# **Springer Theses**Recognizing Outstanding Ph.D. Research

Hiroaki Ishizuka

# Magnetism and Transport Phenomena in Spin-Charge Coupled Systems on Frustrated Lattices



## **Springer Theses**

Recognizing Outstanding Ph.D. Research

#### **Aims and Scope**

The series "Springer Theses" brings together a selection of the very best Ph.D. theses from around the world and across the physical sciences. Nominated and endorsed by two recognized specialists, each published volume has been selected for its scientific excellence and the high impact of its contents for the pertinent field of research. For greater accessibility to non-specialists, the published versions include an extended introduction, as well as a foreword by the student's supervisor explaining the special relevance of the work for the field. As a whole, the series will provide a valuable resource both for newcomers to the research fields described, and for other scientists seeking detailed background information on special questions. Finally, it provides an accredited documentation of the valuable contributions made by today's younger generation of scientists.

#### Theses are accepted into the series by invited nomination only and must fulfill all of the following criteria

- They must be written in good English.
- The topic should fall within the confines of Chemistry, Physics, Earth Sciences, Engineering and related interdisciplinary fields such as Materials, Nanoscience, Chemical Engineering, Complex Systems and Biophysics.
- The work reported in the thesis must represent a significant scientific advance.
- If the thesis includes previously published material, permission to reproduce this must be gained from the respective copyright holder.
- They must have been examined and passed during the 12 months prior to nomination.
- Each thesis should include a foreword by the supervisor outlining the significance of its content.
- The theses should have a clearly defined structure including an introduction accessible to scientists not expert in that particular field.

More information about this series at http://www.springer.com/series/8790

#### Hiroaki Ishizuka

## Magnetism and Transport Phenomena in Spin-Charge Coupled Systems on Frustrated Lattices

Doctoral Thesis accepted by The University of Tokyo, Tokyo, Japan



Author
Dr. Hiroaki Ishizuka
Department of Applied Physics
The University of Tokyo
Tokyo
Japan

Supervisor
Prof. Yukitoshi Motome
Department of Applied Physics
The University of Tokyo
Tokyo
Japan

ISSN 2190-5053 ISSN 2190-5061 (electronic) Springer Theses ISBN 978-4-431-55662-6 ISBN 978-4-431-55663-3 (eBook) DOI 10.1007/978-4-431-55663-3

Library of Congress Control Number: 2015941880

Springer Tokyo Heidelberg New York Dordrecht London

© Springer Japan 2015

This work is subject to copyright. All rights are reserved by the Publisher, whether the whole or part of the material is concerned, specifically the rights of translation, reprinting, reuse of illustrations, recitation, broadcasting, reproduction on microfilms or in any other physical way, and transmission or information storage and retrieval, electronic adaptation, computer software, or by similar or dissimilar methodology now known or hereafter developed.

The use of general descriptive names, registered names, trademarks, service marks, etc. in this publication does not imply, even in the absence of a specific statement, that such names are exempt from the relevant protective laws and regulations and therefore free for general use.

The publisher, the authors and the editors are safe to assume that the advice and information in this book are believed to be true and accurate at the date of publication. Neither the publisher nor the authors or the editors give a warranty, express or implied, with respect to the material contained herein or for any errors or omissions that may have been made.

Printed on acid-free paper

Springer Japan KK is part of Springer Science+Business Media (www.springer.com)

#### Parts of this thesis have been published in the following journal articles:

#### **Original Paper**

- 1. Hiroaki Ishizuka and Yukitoshi Motome, "Exotic magnetic states in an Ising-spin Kondo lattice model on a Kagome lattice", Phys. Rev. B **91**, 085110 (2015).
- 2. Hiroaki Ishizuka, Masafumi Udagawa, and Yukitoshi Motome, "Polynomial expansion Monte Carlo study of frustrated itinerant electron systems: application to a spin-ice type Kondo lattice model on a pyrochlore lattice", Comput. Phys. Commun. **184**, 2684 (2013).
- 3. Hiroaki Ishizuka and Yukitoshi Motome, "Spontaneous spacial inversion symmetry breaking and spin Hall effect in a spin-ice double-exchange model on a pyrochlore lattice", Phys. Rev. B. **88**, 100402(R) (2013).
- 4. Hiroaki Ishizuka and Yukitoshi Motome, "Loop liquid in an Ising-spin Kondo lattice model on a kagome lattice", Phys. Rev. B **88**, 081105(R) (2013).
- 5. Hiroaki Ishizuka and Yukitoshi Motome, "Thermally-induced phases in an Ising Kondo lattice model on a triangular lattice: partial disorder and Kosterlitz-Thouless state", Phys. Rev. B 87, 155156 (2013).
- 6. Hiroaki Ishizuka and Yukitoshi Motome, "Quantum anomalous Hall effect in kagome ice", Phys. Rev. B **87**, 081105(R) (2013).
- 7. Hiroaki Ishizuka and Yukitoshi Motome, "Dirac half-metal in a triangular ferrimagnet", Phys. Rev. Lett. **109**, 237207 (2012)
- 8. Hiroaki Ishizuka, Masafumi Udagawa, and Yukitoshi Motome, "Magnetic Order and Charge Disproportionation in a Spin-ice type Kondo Lattice Model: Large Scale Monte Carlo Study", J. Phys. Soc. Jpn. **81**, 113706 (2012).
- 9. Hiroaki Ishizuka and Yukitoshi Motome, "Partial disorder in an Ising-spin Kondo lattice model on a triangular lattice", Phys. Rev. Lett. **108**, 257205 (2012).

#### **Proceedings**

- 1. Hiroaki Ishizuka and Yukitoshi Motome, "On the Stability of Quantum Hall Kagome-ice Insulator", JPS Conf. Proc. 3, 014010 (2014).
- 2. Hiroaki Ishizuka and Yukitoshi Motome, "Thermally-induced magnetic phases in an Ising spin Kondo lattice model on a kagome lattice at 1/3-filling", J. Korean Phys. Soc. **63**, 579 (2013).
- 3. Hiroaki Ishizuka, Masafumi Udagawa, and Yukitoshi Motome, "Application of polynomial-expansion Monte Carlo method to a spin-ice Kondo lattice model", J. Phys.: Conf. Ser. **400**, 032027 (2012).
- \* Following figures are reproduced with permission from the above papers: Figs. 3.2–3.16, 4.1–4.4, 5.2, 5.3, 5.5–5.8, 6.1, 6.2, 6.4, 6.5, 6.8–6.10, 7.1–7.4, 8.1–8.6, and 9.1–9.8.

### **Supervisor's Foreword**

The interplay between charge and spin degrees of freedom of electrons in solids has attracted much interest in a broad range of fields in condensed matter physics. In magnetic conductors, the spin-dependent scattering of electrons plays an important role in their peculiar magnetic and transport phenomena, such as the giant magnetoresistance and spin-transfer torque. In these systems, the underlying spin texture affects the electrical transport, and at the same time the electron motion has an influence on the magnetism. Thus, the electronic and magnetic states are determined in a self-consistent manner through the spin-charge interplay, which is a key for understanding of the fascinating phenomena. Recently, the exploration of such intriguing physics has been conducted for the systems with geometrically frustrated lattice structures. The geometrical frustration has also been studied for a long time, in particular, in insulating magnets for their peculiar magnetism, such as complicated magnetic orders, spin glasses, and spin liquids. In magnetic conductors on geometrically frustrated lattices, however, further interesting phenomena are anticipated through the spin-charge interplay. In fact, a variety of novel phenomena have been discovered successively; for instance, the unconventional anomalous Hall effect and peculiar diffusive conductivity in pyrochlore compounds and partially disordered magnetism in layered triangular materials. The theoretical understanding of these phenomena is a challenge, as it is necessary to deal with the keen competition between different electronic and magnetic states under the influence of geometrical frustration.

In the present thesis work by Hiroaki Ishizuka, fundamental aspects of the spin-charge coupled phenomena under geometrical frustration have systematically been investigated for three different types of lattice structures, i.e., triangular, kagome, and pyrochlore. He discovered that strong fluctuations enhanced by geometrical frustration result in unprecedented phenomena, not only in peculiar magnetic and transport properties but also in the topological nature of the systems. Given the simplicity of the models studied here, the diversity of the findings is rather surprising but highlights the distinctive effect of geometrical frustration on spin-charge coupled systems. The key theoretical tool in his study is a large-scale

Monte Carlo simulation, which provides numerically exact results fully taking into account the fluctuation effects and makes it possible to discriminate the different states in keen competition. The current study offers the theoretical understanding of the mechanisms of complex phenomena, which will stimulate further experimental studies in the rapidly growing field. It also provides an important basis for a deeper exploration of new physics emergent from the subtle interplay between charge and spin degrees of freedom.

Tokyo, Japan March 2015 Prof. Yukitoshi Motome

### Acknowledgments

It has been more than 4 years since I came to Tokyo for my graduate study. Ever since, I have had a countless number of valuable interactions with many people. It would have been impossible to complete this thesis without their help and collaboration.

First of all, I would like to express my sincere gratitude to my supervisor, Professor Yukitoshi Motome, for his support and continuous encouragement for more than 4 years. I gained a huge range of knowledge from him.

I am also grateful to Professor Masatoshi Imada and Professor Nobuo Furukawa for fruitful discussions throughout the research project. Their insightful comments have helped me very much. I am thankful as well to Professor Cristian D. Batista and Professor Karlo Penc for helpful comments and discussions. In addition, I thank Professor Seiji Miyashita, Professor Naoto Nagaosa, and Professor Yoshinori Tokura for being on my thesis committee.

It has been a great experience to learn from talented assistant professors, post-docs, and students. I am especially thankful to Dr. T. Misawa, Dr. H. Shinaoka, Dr. A. Shitade, Dr. M. Udagawa, and Dr. Y. Yamaji. As well, I thank the members of the Arita group, the Imada group, and the Motome group for their help in many ways.

Finally, I would like to express special gratitude to my family for their support and encouragement over the years.

## **Contents**

1	Intro	oduction		1	
	1.1	Spin-Cl	harge Coupled Systems	1	
	1.2	Magnet	tism in Spin-Charge Coupled Systems	3	
		1.2.1	Ruderman-Kittel-Kasuya-Yosida Interaction	3	
		1.2.2	Double-Exchange Interaction	5	
		1.2.3	Magnetic Ordering by a Metal-Insulator Transition	7	
	1.3	Transpo	ort Phenomena in Spin-Charge Coupled Systems	8	
		1.3.1	Metal-Insulator Transition	8	
		1.3.2	Electron Scattering by Localized Moments	8	
		1.3.3	Anomalous Hall Effect Induced by the Spin		
			Berry Phase	9	
	1.4	Pyroch	lore Oxides	10	
		1.4.1	Lattice and Electronic Structure	11	
		1.4.2	Geometrical Frustration in Pyrochlore Magnets	12	
		1.4.3	Subdominant Interactions in Spin Ice Compounds	12	
		1.4.4	Metallic Pyrochlore Magnets	13	
		1.4.5	$R_2$ Mo <sub>2</sub> O <sub>7</sub>	14	
		1.4.6	$R_2\operatorname{Ir}_2\operatorname{O}_7\ldots\ldots\ldots\ldots\ldots$	18	
	1.5				
		1.5.1	Partially Disordered State	21	
		1.5.2	$Ag_2CrO_2$	22	
	1.6	Motiva	tion of This Study	23	
	1.7	Structu	re of This Thesis	24	
	Refe	References			
2	Mod	els and N	Methods	27	
4	2.1		pin Kondo Lattice Model	27	
	2.1	2.1.1	Kondo Lattice Model on Frustrated Lattices	27	
		2.1.1	Strong Coupling Limit	28	
	2.2		Carlo Simulation	28	
	4.4	IVIOIILE	Caro Simuandi	∠C	

xii Contents

	2.3	Polynomial Expansion Method	29
		2.3.1 Truncation Algorithm	30
		2.3.2 Physical Quantities	32
		2.3.3 Conductivity	33
	2.4	Variational Method	33
	2.5	Perturbation Method in the Strong Coupling Limit	33
	Refe	rences	34
3	Part	ial Disorder on a Triangular Lattice	35
	3.1	Model and Method	35
		3.1.1 Model	35
		3.1.2 Physical Quantities	36
	3.2	Mean Field Theory	38
	3.3	Monte Carlo Simulation	41
	0.0	3.3.1 Phase Diagrams	41
		3.3.2 Partial Disorder	43
		3.3.3 Other Magnetic Orders	46
		3.3.4 Phase Separation	50
	3.4	Electronic State	51
	3.5	Summary	53
		rences.	53
	1010	renees.	33
4		c Half-Metal on a Triangular Lattice	55
4	<b>Dira</b> 4.1	Model and Method	55
4		Model and Method	55 55
4	4.1	Model and Method	55 55 56
4		Model and Method	55 55
4	4.1	Model and Method	55 55 56 57 58
4	4.1	Model and Method       4.1.1 Model         4.1.2 Numerical Calculations       8         Band Structure       10         Low-Energy Effective Hamiltonian       10         4.3.1 $k \cdot p$ Perturbation Theory       10	55 55 56 57 58 58
4	4.1	Model and Method	55 55 56 57 58
4	4.1	Model and Method4.1.1 Model4.1.2 Numerical Calculations4.1.2 Numerical CalculationsBand StructureLow-Energy Effective Hamiltonian4.3.1 $k \cdot p$ Perturbation Theory4.3.2 Condition for the Dirac Half-MetalPhase Diagrams	55 55 56 57 58 58
4	4.1 4.2 4.3	Model and Method	55 55 56 57 58 58 59
4	4.1 4.2 4.3 4.4 4.5	Model and Method4.1.1 Model4.1.2 Numerical Calculations4.1.2 Numerical CalculationsBand StructureLow-Energy Effective Hamiltonian4.3.1 $k \cdot p$ Perturbation Theory4.3.2 Condition for the Dirac Half-MetalPhase Diagrams	55 55 56 57 58 58 59 60
	4.1 4.2 4.3 4.4 4.5 Refe	Model and Method	55 55 56 57 58 58 59 60 62 63
5	4.1 4.2 4.3 4.4 4.5 Refe	Model and Method	55 55 56 57 58 58 59 60 62 63
	4.1 4.2 4.3 4.4 4.5 Refe	Model and Method .  4.1.1 Model .  4.1.2 Numerical Calculations  Band Structure .  Low-Energy Effective Hamiltonian .  4.3.1 k·p Perturbation Theory .  4.3.2 Condition for the Dirac Half-Metal .  Phase Diagrams .  Discussion and Summary .  rences .  rmally-Induced Phases on a Kagome Lattice .  Model and Method .	55 55 56 57 58 58 59 60 62 63
	4.1 4.2 4.3 4.4 4.5 Refe	Model and Method  4.1.1 Model  4.1.2 Numerical Calculations  Band Structure  Low-Energy Effective Hamiltonian  4.3.1 k·p Perturbation Theory  4.3.2 Condition for the Dirac Half-Metal  Phase Diagrams  Discussion and Summary  rences.   rmally-Induced Phases on a Kagome Lattice  Model and Method  5.1.1 Model	55 55 56 57 58 58 59 60 62 63 65 65
	4.1 4.2 4.3 4.4 4.5 Refe	Model and Method  4.1.1 Model  4.1.2 Numerical Calculations  Band Structure  Low-Energy Effective Hamiltonian  4.3.1 k·p Perturbation Theory  4.3.2 Condition for the Dirac Half-Metal  Phase Diagrams  Discussion and Summary  rences.   Temally-Induced Phases on a Kagome Lattice  Model and Method  5.1.1 Model  5.1.2 Monte Carlo Method	55 55 56 57 58 58 59 60 62 63 65 65 65 66
	4.1 4.2 4.3 4.4 4.5 Refe	Model and Method	55 55 56 57 58 58 59 60 62 63 65 65 66 66
	4.1 4.2 4.3 4.4 4.5 Refe Ther 5.1	Model and Method  4.1.1 Model  4.1.2 Numerical Calculations  Band Structure  Low-Energy Effective Hamiltonian  4.3.1 $k \cdot p$ Perturbation Theory  4.3.2 Condition for the Dirac Half-Metal Phase Diagrams  Discussion and Summary  rences.  rmally-Induced Phases on a Kagome Lattice  Model and Method  5.1.1 Model  5.1.2 Monte Carlo Method  5.1.3 Variational Calculation  5.1.4 Observables	55 55 56 57 58 58 59 60 62 63 65 65 66 66 66
	4.1 4.2 4.3 4.4 4.5 Refe	Model and Method  4.1.1 Model  4.1.2 Numerical Calculations  Band Structure  Low-Energy Effective Hamiltonian  4.3.1 k·p Perturbation Theory  4.3.2 Condition for the Dirac Half-Metal  Phase Diagrams  Discussion and Summary  rences.   **mally-Induced Phases on a Kagome Lattice  Model and Method  5.1.1 Model  5.1.2 Monte Carlo Method  5.1.3 Variational Calculation  5.1.4 Observables  Loop-Liquid State	55 55 56 57 58 58 59 60 62 63 65 65 66 66 66 66 68
	4.1 4.2 4.3 4.4 4.5 Refe Ther 5.1	Model and Method  4.1.1 Model  4.1.2 Numerical Calculations  Band Structure  Low-Energy Effective Hamiltonian  4.3.1 $k \cdot p$ Perturbation Theory  4.3.2 Condition for the Dirac Half-Metal Phase Diagrams  Discussion and Summary  rences.  rmally-Induced Phases on a Kagome Lattice  Model and Method  5.1.1 Model  5.1.2 Monte Carlo Method  5.1.3 Variational Calculation  5.1.4 Observables	55 55 56 57 58 58 59 60 62 63 65 65 66 66 66

Contents xiii

	5.3	Partial	Disorder	74		
	5.4	Summa	ary	76		
	Refe	rences		77		
6	Anomalous Hall Insulator in Kagome Ice					
	6.1		and Method	79		
		6.1.1	Kagome Ice Model	79		
		6.1.2	Numerical Diagonalization	81		
		6.1.3	Monte Carlo Simulation	81		
	6.2	Exact 1	Diagonalization Study of Electronic States	82		
		6.2.1	Density of States	82		
		6.2.2	In-Gap Localized States	83		
		6.2.3	Conductivity	83		
	6.3	Monte	Carlo Simulation	85		
		6.3.1	Magnetic Properties	85		
		6.3.2	Electronic and Transport Properties	87		
	6.4	Anisot	ropic Pyrochlore Lattice	89		
	6.5	Discussion and Summary				
	Refe			90		
7	Spin	-Charge	Coupled Phases on a Pyrochlore Lattice	93		
	7.1		and Method	93		
		7.1.1	Spin-Ice Kondo Lattice Model	93		
		7.1.2	Monte Carlo Simulation	94		
		7.1.3	Physical Quantities	95		
	7.2	Phase	Diagram	96		
	7.3	Temperature Dependence of Physical Quantities				
	7.4	Magnetic Field Switching of Charge Disproportionation				
	7.5		sion and Summary	100		
	Refe			101		
8	Spin	-Cluster	State in a Pyrochlore Lattice	103		
	8.1		and Method	103		
		8.1.1	Spin-Ice Double-Exchange Model	103		
		8.1.2	Perturbation Theory	105		
		8.1.3	Monte Carlo Simulation for the Effective Ising			
			Spin Model	105		
		8.1.4	Monte Carlo Simulation for the Double-Exchange			
			Model	105		
		8.1.5	Physical Quantities	105		

xiv Contents

	8.2	Effective Spin Model	107		
		8.2.1 $J_1$ - $J_2$ - $J_3$ Ising Model	107		
		8.2.2 Monte Carlo Simulation	107		
		8.2.3 Emergent Frustration Induced by Further			
		Neighbor Interactions	110		
	8.3	Monte Carlo Study of the Double-Exchange Model	111		
	8.4	Spin Hall Effect	113		
	8.5	Discussion and Summary	113		
	Refe	rences	114		
9	Beno	chmark of the Polynomial Expansion Monte			
		o Method	115		
	9.1	Model and Parameters	115		
		9.1.1 Spin-Ice Kondo Lattice Model	115		
		9.1.2 Details of the Calculation and Physical Quantities	116		
	9.2	Temperature Dependence	117		
	9.3	Convergence in the Number of Polynomials			
	9.4	Convergence in the Truncation Distance			
	9.5	Convergence in the Truncation Distance			
		for Larger Systems	123		
	9.6	Discussion	124		
	9.7	Summary	126		
	Refe	rences	126		
10	Sum	mary	127		
Cui	rriculı	ım Vitae	131		

# Chapter 1 Introduction

**Abstract** Physics of spin-charge coupled systems, systems with itinerant electrons and localized moments that interact with each other, is one of the major topics in the field of strongly correlated electrons. In these systems, the itinerant electrons mediate effective interactions between the localized moments giving rise to rich magnetic behaviors in some of the metallic magnets. Meanwhile, the scattering from localized moments may strongly affects electronic structure of itinerant electrons, inducing unconventional electronic states and transport phenomena. Among various materials of this class, recently, metallic magnets on pyrochlore and triangular lattices have gained interest for there unusual magnetic and transport properties observed in several materials. In these materials, along with the spin-charge coupling, geometrical frustration potentially plays an important roles. In this chapter, we review basic aspects of the spin-charge coupled systems and geometrical frustration.

#### 1.1 Spin-Charge Coupled Systems

A minimal model with the spin-charge coupling is given by the following form,

$$H = -t \sum_{\langle i,j \rangle, \sigma} (c_{i\sigma}^{\dagger} c_{j\sigma} + \text{H.c.}) - J \sum_{j} {}' \mathbf{S}_{j} \cdot \boldsymbol{\sigma}_{j}. \tag{1.1}$$

Here,  $c_{i\sigma}$  ( $c_{i\sigma}^{\dagger}$ ) is the annihilation (creation) operator of an itinerant electron with spin  $\sigma = \uparrow, \downarrow$  at *i*th site, and *t* is the transfer integral. The sum  $\langle i, j \rangle$  is taken over nearest-neighbor (NN) sites. The second term is the onsite (*s*-*d*) interaction between localized spins and itinerant electrons. In the term,  $\mathbf{S}_i$  and

$$\sigma_{j} = \sum_{\alpha,\beta} c_{j\beta}^{\dagger} \tau_{\beta\alpha} c_{j\alpha} \tag{1.2}$$

1

represent the localized spin and itinerant electron spin at jth site, respectively, and J is the coupling constant;  $\sum_{j}'$  is the sum over all sites with localized spins (not neccessary be all the sites in the system).

© Springer Japan 2015 H. Ishizuka, *Magnetism and Transport Phenomena in Spin-Charge Coupled Systems on Frustrated Lattices*, Springer Theses, DOI 10.1007/978-4-431-55663-3\_1

This model has a wide range of applications in the condensed matter physics. One example is noble metal (Au, Ag, Cu, Pt) alloys doped with a small amount of magnetic ions (Fe or Mn) [6]. In these systems, the magnetic moments from the magnetic ions are located randomly in the system, typically 1/100-1/10 of the total sites. These moments on the doped ions interact with itinerant electrons in the metallic alloy, which is thought to be described by the second term of Eq. (1.1). On the other hand, as the typical distance between the localized moments being large, it is expected that the direct exchange interaction between the moments is negligible.

Equation (1.1) is also considered as a simplified model for some of transition-metal and rare-earth oxides; in this case, the magnetic moments are located periodically on every sites. To be specific, here we consider a transition metal compound with open 3d shell filled with four electrons. This is the case for colossal magnetoresitive manganites, where three to four electrons occupy the 3d orbitals depending on the doping. When the transition-metal ion is surrounded by six oxygens forming an octahedron, the degeneracy of 3d shell orbitals is partially lifted by crystal field, splitting into two  $e_g$  orbitals and three  $t_{2g}$  orbitals. In the case of octahedral coordination, the  $t_{2g}$  orbitals have lower energy than the  $e_g$  orbitals; with sufficiently strong crystal field, the  $t_{2g}$  bands are energetically separated from the  $e_g$  bands by an energy gap.

If the Hund's coupling between the electrons is sufficiently strong, three out of four electrons occupy the lower  $t_{2g}$  orbitals with aligning there spins parallel, while the remaining one is placed in one of the  $e_g$  orbitals to benefit from the magnetic interaction. In this case, the electrons in  $t_{2g}$  orbitals can be considered as S=3/2 localized moments as the  $t_{2g}$  levels are far below the Fermi level and have a small intersite overlap between them. On the other hand, the electrons in the  $e_g$  orbitals remain itinerant, which are interacting with the S=3/2 localized moments by the Hund's coupling. In all, the system can be considered as a spin-charge coupled system in which the localized  $t_{2g}$  moment is coupled to  $e_g$  itinerant electrons; the coupling is ferromagnetic (FM) due to the Hund's coupling.

A similar but slightly different situation is realized in rare-earth ions. In rare-earth compounds, the 4f orbitals and orbitals with larger principal quantum number reside close to the Fermi level, contributing to their low temperature behavior. In many of these compounds, the 4f orbitals remain partially filled due to the strong Coulomb repulsion between the 4f electrons, although they tend to have lower one-particle energy than other partially filled shells. In addition, due to the strong repulsion, the number of electrons in 4f orbitals is often virtually fixed at a commensulate value. Hence, a similar situation to the above transition-metal ion is realized, where the 4f electrons can be viewed as localized spins which are interacting with itinerant electrons on orbitals with larger principal quantum number. One difference here is that the effective interaction between the localized moments and the itinerant electrons usually comes from the super-exchange mechanism; they tend to be antiferromagnetic (AFM).

#### 1.2 Magnetism in Spin-Charge Coupled Systems

#### 1.2.1 Ruderman-Kittel-Kasuya-Yosida Interaction

One interesting consequence of the spin-charge coupling in Eq. (1.1) is that, the itinerant electrons mediate effective spin interactions between the localized moments. When J/t is sufficiently weak, the effective interactions are well approximated by the exchange-type interactions that arise from a second-order perturbation theory. This was originally discussed by Ruderman and Kittel [41] in the context of interactions between the nuclear moments. Soon after their work, Kasuya [21] and Yosida [61] independently applied a similar argument to transition-metal systems, where the localized moments of 3d orbitals interact with itinerant electrons. This is called the Ruderman-Kittel-Kasuya-Yosida (RKKY) interaction after their pioneering works.

Let us explain how the RKKY interaction arises from the spin-charge coupling. We consider the first term of Eq. (1.1) as non-perturbative term  $H_0$  and the second term as the perturbation term H';

$$H = H_0 + H', (1.3)$$

where

$$H_0 = \sum_{\mathbf{k} \sigma} \varepsilon_{\mathbf{k}\sigma} c_{\mathbf{k}\sigma}^{\dagger} c_{\mathbf{k}\sigma}, \tag{1.4}$$

$$H' = -J \sum_{j} {}^{\prime} \mathbf{S}_{j} \cdot \boldsymbol{\sigma}_{j} \tag{1.5}$$

$$= -J \sum_{j} \sum_{\mathbf{q}} e^{i\mathbf{q} \cdot \mathbf{R}_{j}} \mathbf{S}_{j} \cdot \boldsymbol{\sigma}_{\mathbf{q}}. \tag{1.6}$$

Here,  $c_{\mathbf{k}\sigma}$  ( $c_{\mathbf{k}\sigma}^{\dagger}$ ) is the Fourier transform of annihilation (creation) operator  $c_{i\sigma}$  ( $c_{i\sigma}^{\dagger}$ ),  $\mathbf{R}_{j}$  is the position of the localized moment  $\mathbf{S}_{j}$ .

$$\sigma_{j} = \sum_{\alpha,\beta} c_{j\beta}^{\dagger} \tau_{\beta\alpha} c_{j\alpha} \tag{1.7}$$

and

$$\sigma_{\mathbf{q}} = \frac{1}{N} \sum_{\mathbf{k}, \alpha, \beta} c_{\mathbf{k} - \mathbf{q}\beta}^{\dagger} \tau_{\beta\alpha} c_{\mathbf{k}\alpha}. \tag{1.8}$$

is the itinerant electron spin and its Fourier transform, respectively; N is the number of the sites and  $\tau_{\beta\alpha}$  is the vector of  $\beta\alpha$  components of the Pauli matrices. In this section, for simplicity, we approximate the electron dispersion by that for the free

electron gas, i.e.,

$$\varepsilon_{\mathbf{k}} = \frac{k^2}{2m^*},\tag{1.9}$$

where  $m^*$  is the effective mass.

The Rayleigh-Schrodinger perturbation theory in terms of J gives the second-order effective Hamiltonian in the form

$$H^{(2)} = \sum_{\mathbf{k}\alpha, \mathbf{k}'\beta} \frac{\langle \mathbf{k}\alpha | H' | \mathbf{k}'\beta \rangle \langle \mathbf{k}'\beta | H' | \mathbf{k}\alpha \rangle}{\varepsilon_{\mathbf{k}} - \varepsilon_{\mathbf{k}'}},$$
(1.10)

where  $|\mathbf{k}\alpha\rangle$  is the one-particle wave function with wave number  $\mathbf{k}$  and spin  $\alpha$ . A straightforward calculation gives

$$H^{(2)} = \frac{m^* J^2}{N^2} \sum_{i>j} \mathbf{S}_j \cdot \mathbf{S}_i \sum_{\mathbf{k}, \mathbf{k}'} \frac{e^{i(\mathbf{k} - \mathbf{k}) \cdot (\mathbf{R}_j - \mathbf{R}_i)}}{\mathbf{k}^2 - \mathbf{k}'^2}.$$
 (1.11)

By replacing the sum by an integral, we obtain

$$H^{(2)} = \frac{2m^* J^2 k_F^4}{(2\pi)^3} \sum_{i>j} K(2k_F R_{ij}) \mathbf{S}_j \cdot \mathbf{S}_i,$$
(1.12)

where

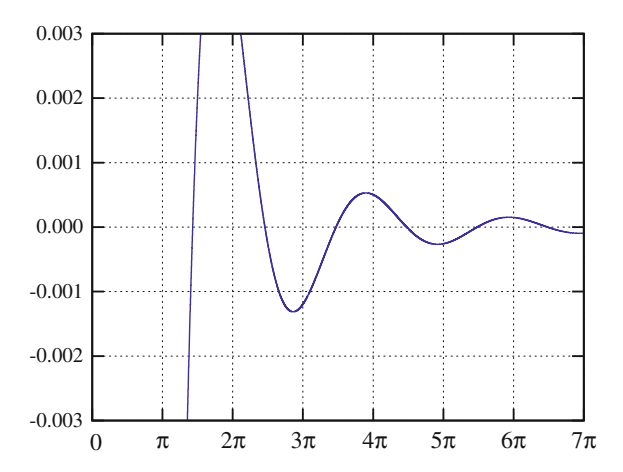
$$K(x) = \frac{x\cos(x) - \sin(x)}{x^4}.$$
 (1.13)

Here,  $R_{ij} = |\mathbf{R}_i - \mathbf{R}_j|$  is the distance between the two spins at ith and jth sites and  $k_{\rm F}$  is the Fermi wave number. Hence, the second-order perturbation theory gives rise to effective exchange-type spin interactions.

There are two distinct features in the RKKY interaction in Eq. (1.12). The first one is the power-law nature of interaction with respect to the distance between two spins. In the case of the direct exchange interaction, the interaction is expected to decay exponentially with respect to distance, and hence, the interactions between further-neighbor sites are often negligible. In contrast, the RKKY interaction for the 3D electron gas given in Eqs. (1.12) and (1.13) shows power-law decay with respect to distance  $R_{ij}$ ,  $|K(R_{ij})| \sim 1/R_{ij}^3$ . Thus, the RKKY interactions between the spins with long distance often become relevant. Another important point is the sign change of the interaction with respect to  $R_{ij}$ . Figure 1.1 shows the plot of K(x), which gives the distance dependence of the RKKY interaction. The interaction shows oscillation of the sign with distance.

The above two features of RKKY interaction give rise to peculiar magnetic behavior. When the localized moments are periodically aligned on the lattice sites, the

**Fig. 1.1** Plot of K(x) in Eq. (1.13) with respect to x



long-range nature and sign change of interactions often induce frustration between the spins, possibly giving rise to some exotic magnetic orderings such as an incommensurate magnetic order. In the case of the noble alloys doped with magnetic ions, the effective interactions between the localized moments vary from FM to AFM, inducing random interactions between them. As a consequence, the system shows characteristic behavior at low temperature known as spin glass [6].

#### 1.2.2 Double-Exchange Interaction

While some of the phenomena that take place in transition metal alloys are well understood by the RKKY interaction, some transition metal compounds are expected to have a strong coupling between the localized moments and itinerant electrons because of the strong intra-atomic Hund's coupling, as described in Sect. 1.1. In these cases, the RKKY description is expected to be no longer valid, as it is a perturbation theory from the weak J limit. Such case was discussed by Zener [62] and by Anderson and Hasegawa [3], in the context of electron mediated interactions in manganese oxides.

To derive the effective interaction in the strong coupling limit, we consider a twosite FM Kondo lattice model with a classical moment at each site and an itinerant electron hopping between the two sites,

$$H = -t \sum_{\sigma} (c_{1\sigma}^{\dagger} c_{2\sigma} + c_{2\sigma}^{\dagger} c_{1\sigma}) - J \sum_{i=1}^{2} \mathbf{S}_{i} \cdot \boldsymbol{\sigma}_{i}.$$
 (1.14)

As the localized moments are treated as classical ones, once the configuration of the moments is given, the Hamiltonian for itinerant electrons can be given by the one-particle Hamiltonian,

$$H_{e} = \begin{pmatrix} -JS_{1}^{z} & S_{1}^{x} - iS_{1}^{y} & -t & 0\\ S_{1}^{x} + iS_{1}^{y} & JS_{1}^{z} & 0 & -t\\ -t & 0 & -JS_{2}^{z} & S_{2}^{x} - iS_{2}^{y}\\ 0 & -t & S_{2}^{x} + iS_{2}^{y} & JS_{2}^{z} \end{pmatrix}.$$
(1.15)

Here, the first and second rows correspond to the up- and down-spin electrons at the site 1, respectively, and the third and fourth rows for the electrons at the site 2. To consider the strong coupling limit of  $J \to \infty$ , we first transform the basis of Eq. (1.15) so that the Hamiltonian becomes diagonal for the second term in Eq. (1.14). This transformation yields

$$\tilde{H}_{e} = \begin{pmatrix} -J & 0 & -\tilde{t} & -\tilde{t}'_{12} \\ 0 & J & -\tilde{t}'_{21}^* & -\tilde{t}^* \\ -\tilde{t}^* & -\tilde{t}'_{12}^* & -J & 0 \\ -\tilde{t}'_{21} & -\tilde{t} & 0 & J \end{pmatrix}, \tag{1.16}$$

where

$$\tilde{t} = t \left( \cos \frac{\theta_1}{2} \cos \frac{\theta_2}{2} + \sin \frac{\theta_1}{2} \sin \frac{\theta_2}{2} e^{i(\varphi_2 - \varphi_1)} \right), \tag{1.17}$$

and

$$\tilde{t}'_{ij} = t \left( \cos \frac{\theta_i}{2} \sin \frac{\theta_j}{2} e^{-i\varphi_j} + \sin \frac{\theta_i}{2} \cos \frac{\theta_j}{2} e^{-i\varphi_i} \right). \tag{1.18}$$

Here,  $(\theta_i, \varphi_i)$  are the polar coordinates of  $S_i$ .

By applying the first-order Brillouin-Wigner perturbation theory in terms of t/J, we obtain the  $2 \times 2$  double-exchange Hamiltonian that for the electrons with spins parallel to the localized moments,

$$H_{\rm DE} = \begin{pmatrix} -J & -\tilde{t} \\ -\tilde{t}^* & -J \end{pmatrix}. \tag{1.19}$$

In the case of two sites, this Hamiltonian can be further simplified by an unitary transformation,

$$\tilde{H}_{DE} = \begin{pmatrix} -J & -t\cos\frac{\theta}{2} \\ -t\cos\frac{\theta}{2} & -J \end{pmatrix},\tag{1.20}$$

where  $\theta$  is the relative angle between the two spins. The one-particle eigenstates are obtained by diagonalizing the Hamiltonian in Eq. (1.20) as

$$\varepsilon_{\pm} = -J \pm |t| \cos \frac{\theta}{2}.\tag{1.21}$$

To see how the itinerant electrons induce magnetic interaction, let us consider the case in which temperature T is much lower than |t|. In this limit, we can assume that the electrons always occupy the ground state. The total energy of the system with one itinerant electron is given by

$$E = \varepsilon_{-} = -J - |t| \cos \frac{\theta}{2}. \tag{1.22}$$

Hence, the internal energy decreases as the localized moments align their spins parallel to each other, i.e., a FM effective interaction is induced by the itinerant electron. This FM interaction is called the double-exchange interaction. In general, the double-exchange interaction favors a magnetic configuration that optimizes the kinetic energy of itinerant electrons. In a lattice model with localized moments at every lattice site, it often favors FM ordering.

#### 1.2.3 Magnetic Ordering by a Metal-Insulator Transition

In spin-charge coupled systems, a metal-insulator transition in the electronic bands of itinerant electrons may takes place associated with a formation of magnetic orderings. This is related to the folding of the Brillouin zone, which was originally proposed in a charge-phonon coupled systems in one dimension.

In a one-dimensional chain, the electronic states at  $k=\pm k_{\rm F}$  is degenerate at the Fermi level. In general, when there is degeneracy at the Fermi level, the system responds sensitively to a perturbation that couples those degenerate states, and lifts the degeneracy. In a chain, such mechanism leads to a formation of superstructure by a lattice distortion of period  $1/2k_{\rm F}$ . This occurs associated with a metal-insulator transition, as the lifting of degeneracy pushes the two states away from the Fermi level. This is known as the Peierls transition [39].

A similar transition my occur by a formation of a magnetic order instead of the lattice distortion. This type of metal-insulator transition accompanied by a magnetic ordering was discussed in the interacting electron systems, that was called the Slater mechanism [43].

A similar phenomenon takes place in the Kondo lattice model when a long-range magnetic order develops; a magnetic order of period  $1/2k_{\rm F}$  couples to the electrons at the Fermi level, driving a metal-insulator transition. The Brillouin zone is folded into 1/n of the original one under the formation of an n-site magnetic superlattice. At the same time, an energy gap opens at the edge of the folded Brillouin zone, leading to an energy gain.

An important feature of the magnetic ordering associated with the metal-insulator transition is that, unlike the case of RKKY interactions, the energy gain by the energy-gap opening can not be expressed as an effective two-spin interaction. Hence, in

general, the Peierls-type mechanism can induce a magnetic ordering, which can not be realized in localized spin systems. We present one of such cases in Chap. 3, where the metal-insulator transition stabilizes a partially disordered state in two dimensions.

#### 1.3 Transport Phenomena in Spin-Charge Coupled Systems

#### 1.3.1 Metal-Insulator Transition

While the coupling between the localized moments and itinerant electrons gives rise to effective interactions, it also affects the electronic and transport properties of the itinerant electrons. In this section, we briefly review the effect of spin-charge coupling on the itinerant electrons with considering the case of classical localized moments.

An example is the metal-insulator transition in the Peierls-type mechanism discussed in Sect. 1.2.3. In this case, as the size of charge gap depends on the development of the magnetic order, the temperature dependence of the resistivity deviates from the Arrhenius equation. This can be used as a signature of correlation-induced metal-insulator transition.

#### 1.3.2 Electron Scattering by Localized Moments

In a metallic phase, fluctuating spins contribute to the electrical resistivity of itinerant electrons as they act as a source of scattering through the spin-charge coupling. To be specific, let us consider the Ising-spin Kondo lattice model, where the collinear Ising moments are coupled to itinerant electrons. In the high-temperature paramagnetic phase, the localized moments are disordered by thermal fluctuations. As the model does not include the interaction between itinerant electrons, the thermodynamic properties are obtained by taking the statistical average over the one-body problem for each of the disordered spin configurations. This is essentially the same as the random potential problem with binary potential. Hence, in the disordered state, the scattering by localized moments contribute to increase in resistivity.

A similar but more drastic phenomenon takes place in the presence of inhomogeneous magnetic domains. One such example is the Mn oxides  $La_{1-x}Sr_xMnO_3$ . In the manganese compounds, the competition between the Neel type AFM ordered insulator and the FM metal is known to take place by carrier doping (the holes are doped into the  $e_g$  orbitals of Mn sites by replacing the La by Sr ions). In the phase competing region, a first order transition and associated phase separation takes place between the two ordered states. The inhomogeneity of different magnetic orders is expected to be the origin of the colossal magnetoresistance observed in the Mn oxides [51].

#### 1.3.3 Anomalous Hall Effect Induced by the Spin Berry Phase

In addition to the scattering from the localized moments, the spin Berry phase induced by the spin-charge coupling also has a significant effect on the transport properties [25, 37, 59]. As we discussed in Sect. 1.2.2, in the strong coupling limit of the Kondo lattice model in Eq. (1.1), the hopping matrix element is given by Eq. (1.17), which can be written in the form

$$\tilde{t} = t \cos \theta_{ii} e^{i\phi_{ij}}, \tag{1.23}$$

where  $\theta_{ij}$  is the relative angle between the localized moments at ith and jth sites and  $\phi_{ij}$  is the spin Berry phase induced by the rotation of the electron spins associated with the hopping from ith to jth site. By an analogy to the Peierls phase induced by the external magnetic field, the spin Berry phase can induce the Hall effect in the presence of a certain spin texture.  $^{1}$ 

The anomalous Hall effect induced by the spin Berry phase mechanism attracted interest as the mechanism for an unconventional magnetic field dependence of the anomalous Hall effect in a pyrochlore oxide Nd<sub>2</sub>Mo<sub>2</sub>O<sub>7</sub> [45, 46] (further details on the pyrochlore oxides will be discussed in Sect. 1.4).<sup>2</sup> As a simplified model that shares essential features of the pyrochlore compounds, a double-exchange model on a kagome lattice was studied in the presence of the all-out type magnetic order [37]. A schematic figure of the kagome lattice is shown in Fig. 1.2a. The all-out order is a q = 0 long-range order in which all the spins on a triangle are pointing outward, as shown in Fig. 1.2b. In this case, by choosing the local gauge so that all the spin Berry phases become  $|\phi_{ij}| = \phi/3$ , the Hamiltonian for the itinerant electrons is given by

$$H_{\mathbf{k}} = t' \begin{pmatrix} 0 & 2\cos(\mathbf{k} \cdot \mathbf{a}_1)e^{-i\phi/3} & 2\cos(\mathbf{k} \cdot \mathbf{a}_3)e^{i\phi/3} \\ 2\cos(\mathbf{k} \cdot \mathbf{a}_1)e^{i\phi/3} & 0 & 2\cos(\mathbf{k} \cdot \mathbf{a}_2)e^{-i\phi/3} \\ 2\cos(\mathbf{k} \cdot \mathbf{a}_3)e^{-i\phi/3} & 2\cos(\mathbf{k} \cdot \mathbf{a}_2)e^{i\phi/3} & 0 \end{pmatrix}, \quad (1.24)$$

where  $t' = t \cos(\theta_{ij}/2)$  and

$$\mathbf{a}_1 = \left(-\frac{1}{2}, -\frac{\sqrt{3}}{2}\right), \quad \mathbf{a}_2 = (1, 0), \quad \mathbf{a}_3 = \left(-\frac{1}{2}, \frac{\sqrt{3}}{2}\right).$$
 (1.25)

By diagonalizing the Hamiltonian in Eq. (1.24), one can show that the energy spectrum of the itinerant electrons has an energy gap at electron density n=1/3 and 2/3 for  $\phi \neq 0$ ,  $\pi$ ; here, n is the electron density  $n=\frac{1}{N}\sum_i \langle c_i^{\dagger}c_i \rangle$ . The Hall conductivity can be evaluated by using the Kubo formula, or equivalently, by calculating the first Chern number [23, 53],

<sup>&</sup>lt;sup>1</sup>Hall effect induced by spin textures in weak coupling limit was also discussed in Ref. [50].

<sup>&</sup>lt;sup>2</sup>For the origin of the anomalous Hall effect of Nd<sub>2</sub>Mo<sub>2</sub>O<sub>7</sub>, there is also another theoretical proposal based on the orbital Berry phase [52].

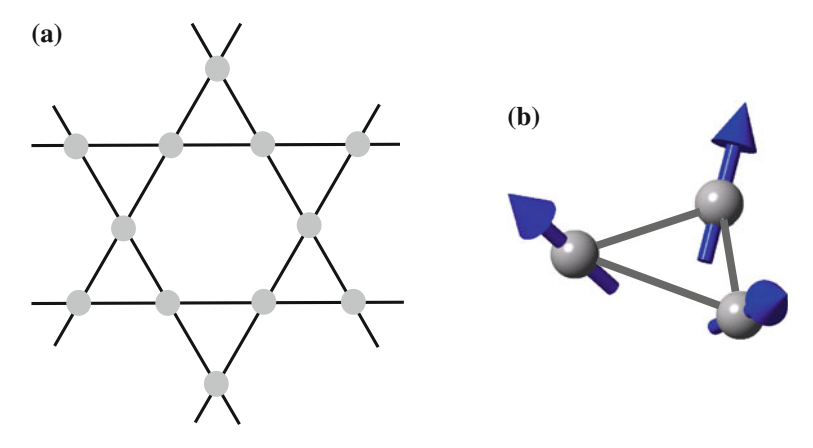


Fig. 1.2 Schematic pictures of a the kagome lattice and b the all-out spin configuration on a triangle unit

$$C_n = \frac{1}{2\pi i} \int_{BZ} d\mathbf{k} \, \hat{\mathbf{z}} \cdot \nabla_{\mathbf{k}} \times \mathbf{A}_n(\mathbf{k}). \tag{1.26}$$

Here,

$$\mathbf{A}_{n}(\mathbf{k}) = \langle n\mathbf{k} | i\nabla_{\mathbf{k}} | n\mathbf{k} \rangle \tag{1.27}$$

is the Berry connection for the nth band and  $\hat{z}$  is the unit vector perpendicular to the kagome plane. The integral is taken over the entire Brillouin zone.

In the cases of  $\phi \neq 0$  and  $\pi$ , the Hall conductance was shown to be [37]

$$\sigma_{\rm H} = -\operatorname{sgn}(\sin\phi) \frac{e^2}{h} \tag{1.28}$$

for both n = 1/3 and 2/3.

#### 1.4 Pyrochlore Oxides

Recently, the experimental study on the magnetism and transport phenomena in spin-charge coupled systems on geometrically frustrated lattices has gained much interest. In these systems, as we discussed in Sect. 1.2, the spins are subject to effective interactions which are mediated by the itinerant electrons via coupling between the itinerant electrons and localized moments. As mentioned in Sect. 1.2, the effective interactions lead to novel magnetic states because of their peculiar nature. In addition, the geometrical frustration of the lattice structure may cause further complicated

situations as the consequence of a macroscopic number of nearly-degenerate states. In this section and the subsequent section, we briefly review a part of recent studies on the frustrated metallic magnets.

#### 1.4.1 Lattice and Electronic Structure

Magnetic pyrochlore oxides  $A_2B_2O_7$  are a class of frustrated magnets which recently gained much interest due to their peculiar properties [14]. In these compounds, the A sites are occupied by rare-earth and some of transition-metal ions and the B sites by transition metal ions and some of tetrels. In the crystal, the ions A and B individually form the pyrochlore lattices which interpenetrate each other.

An important feature of these compounds is the oxygen coordination around the A and B ions. Figure 1.3 shows schematic pictures of A and B ions and their coordinating oxygens. For a B ion site, there are six oxygens coordinating around the ion, forming an octahedral structure (Fig. 1.3b). The distortion of the octahedral cage of oxygens is small, and the O-B-O bond angle ranges from 81° to 100°, which is close to the ideal value 90° [14].

On the other hand, the A site in  $A_2B_2O_7$  has eight coordinating oxygen ions. Figure 1.3a shows a schematic picture of the A site and surrounding oxygen ions; the six oxygen ions form a ring structure, and the remaining two oxygens are placed on the top and bottom of the A site forming a linear O-A-O bonding. A typical distance from the A ion to an oxygen in the ring are 2.4–2.5 Å. On the other hand, the distance between the top oxygen and A ion is typically around 2.2 Å, which is considerably shorter than those to the oxygens in the ring [14]. This strong anisotropy in the coordination gives strong axial crystal field on the electrons at the A site along the linear O-A-O bond. This bond is parallel to the local [111] axis, which is along the line connecting two tetrahedra the ion belongs to.

As stated above, the A sites are usually occupied by rare-earth ions which have the strong spin-orbit coupling; the total angular momentum J = L + S becomes a good quantum number for the 4f electrons in these ions. Here, L and S are the

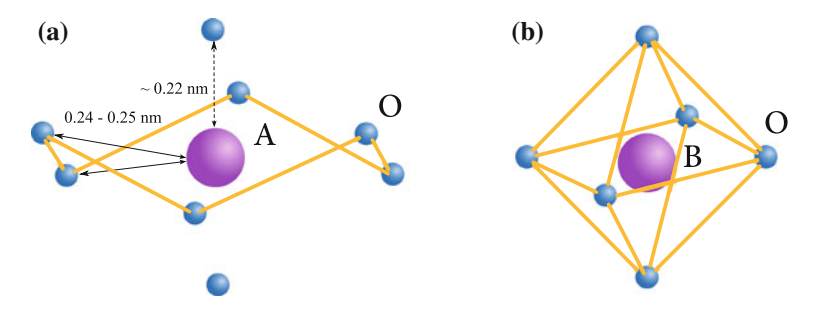


Fig. 1.3 Schematic pictures of  $\bf a$  A and  $\bf b$  B ions and coordinating oxygens in pyrochlore oxides  $A_2B_2O_7$ 

orbital and spin angular momentum, respectively. The spin-orbit coupling and the strong crystal field from the anisotropic coordination of the oxygens lift the 2J + 1 degeneracy of the 4f electrons. As a consequence, the magnetic moments on the A ions are subject to the axial anisotropy. For instance, in the case of  $A_2Ti_2O_7$  and  $A_2Sn_2O_7$  series, the magnetic moments has easy-axis anisotropy in the case of Pr, Nd, Tb, Dy, and Ho, while easy-plane for Er and Yb [14].

#### 1.4.2 Geometrical Frustration in Pyrochlore Magnets

In an insulating compound with one of the A or B ions being non-magnetic, the system can be considered as a localized spin system on a pyrochlore lattice. To be specific, let us consider the Ising moments on a pyrochlore lattice with the strong local [111] easy-axis anisotropy which is realized in several pyrochlore oxides such as Dy<sub>2</sub>Ti<sub>2</sub>O<sub>7</sub> [40] and Ho<sub>2</sub>Ti<sub>2</sub>O<sub>7</sub> [17]. These materials are often called spin ice [7]. In the spin ice compounds, a doublet remains as the single ion ground state due to the crystal field, which can be considered as Ising spins which the moments are directed along the local [111] direction. When the NN interaction is AFM, each tetrahedron favors an all-in or all-out local spin configuration; the schematic picture of the all-out state is shown in Fig. 1.4c. Hence, in the ground state, all the tetrahedra become all-in or all-out forming an AFM long-range order. This is called the all-in/all-out state, in which all the spins on the upward tetrahedra pointing into each tetrahedron and all spins pointing out on the downward tetrahedra.

On the other hand, when the NN interaction is FM, the spin configurations that maximize the net moments of each tetrahedra are favored, and all the tetrahedra become two-in two-out at T=0 (Fig. 1.4a). However, in contrast to the AFM case, the two-in two-out local constraint alone is insufficient for driving the system to order. This is a consequence of the six-fold degeneracy of the two-in two-out configurations; there are macroscopic numbers of global spin configurations for which all the tetrahedra satisfy the two-in two-out constraint [8]. As a result, by only considering the NN interaction, the system remains disordered to absolute zero temperature with only showing the development of two-in two-out local spin correlations.

#### 1.4.3 Subdominant Interactions in Spin Ice Compounds

The ground state degeneracy of the frustrated magnets implies the presence of residual entropy [38], which is the remaining entropy at T=0 associated with the macroscopic degeneracy of the disordered ground state. This apparently contradicts

<sup>&</sup>lt;sup>3</sup>The two-in two-out constraint is called ice rule after its discovery in the study of water ice, where the proton configuration is subject to the equivalent local constraint [5, 38].

<sup>&</sup>lt;sup>4</sup>This situlation is sometimes called as the cooperative paramagnet [56].

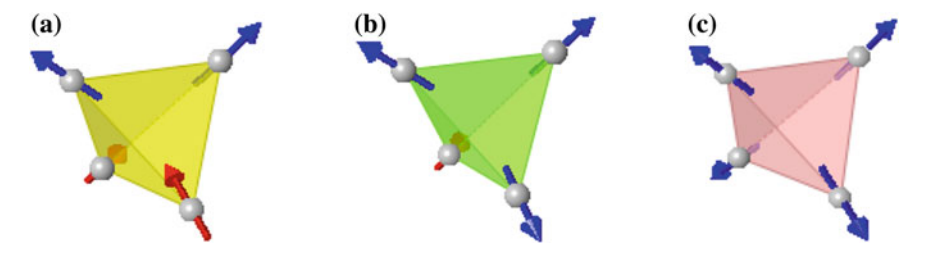


Fig. 1.4 Schematic pictures of a two-in two-out, b one-in three-out, and c all-out tetrahedra of spin ice

with the third raw of thermodynamics stating the entropy  $S \to 0$  for  $T \to 0$ . In the actual compounds, the ground state degeneracy is expected to be lifted by subdominant interactions such as further-neighbor interactions between the magnetic moments. As a consequence, development of a long-range order is expected to take place at low temperatures. Furthermore, such subdominant interactions give rise to nontrivial phenomena which are different from the systems with the NN interactions alone.

One such example is the dipole-dipole interaction in the spin ice compounds [7, 8]. In the spin ice compounds, the A-site rare-earth ions carry large magnetic moments of about  $10\mu_B$ , where  $\mu_B$  is the Bohr magneton. Hence, it is expected that the dipole-dipole interaction becomes relevant; the situation is called the dipolar spin ice [7, 8]. By a Monte Carlo (MC) simulation for a model for the dipolar spin ice, it was discussed that the dipole-dipole interaction lifts the degeneracy of the two-in two-out configurations and gives rise to an AFM order at low temperatures. In addition, it gives rise to phase competition between the spin ice and the all-in/all-out ordered states by changing the NN interaction from AFM to FM [32]. It also gives rise to a first-order transition in the T-H phase diagram with magnetic field along the  $\langle 111 \rangle$  direction, from the kagome-ice magnetization plateau state to the saturated state [4, 9, 18].

#### 1.4.4 Metallic Pyrochlore Magnets

In the pyrochlore oxides, there are several compounds that possess metallic nature. Some examples for such materials are the compounds that Ir and Mo ions occupy the B sites. In the case of metallic compounds, the itinerant electrons coming from the B ions interact with the localized moments on the A sites. In these compounds, through the spin-charge coupling, the effective nearest-neighbor interaction mediated by itinerant electrons together with the geometrical structure possibly gives rise to the frustration between the localized moments. On the other hand, the spin-charge coupling also gives rise to the subdominant interactions such as the further-neighbor

RKKY interactions. In analogy with the dipolar spin ice, such subdominant effects induced by the spin-charge coupling may give rise to novel magnetic behavior.

Another interesting aspect of these compounds is the transport phenomena. In these compounds, if the cooperative paramagnetic state or a novel magnetic state emerges, it may also affect the electronic state of itinerant electrons via the spin-charge coupling. In such a case, it is likely that a signature of the modified electronic state is observed in transport properties. Focusing on these points, in the rest of this section, we review recent experimental and theoretical studies on the metallic pyrochlore compounds.

#### $1.4.5 R_2 Mo_2 O_7$

The first class of the metallic pyrochlore compounds discussed here is the molybdenum pyrochlore oxides  $R_2\text{Mo}_2\text{O}_7$  (R is rare earth). A series of materials in this group is known to show a rich phase diagram with the substitution of the rare-earth ions and by applying the external pressure [2, 15, 16, 19, 22]. Figure 1.5 shows the phase diagram for the substitution sorted by the ionic radius of R. Dy and Tb ions have relatively small ionic radii and are located in the left side in the phase diagram, where a spin-glass insulating phase emerges in the low-temperature region. On the other hand, Nd and Sm ions have larger ionic radii and are located in the right side, where a FM metallic state is dominant in the broad range of temperature up to  $\sim 100 \, \text{K}$ . Gd and Eu compounds are located in the vicinity of the phase boundary between these two phases. In the competing region, the spin-glass metallic phase emerges. As a consequence, the series of compounds shows systematic evolution of the low temperature phase from the spin-glass insulating phase, the spin-glass metallic phase, to the FM metallic phase with increasing the ionic radius of rare-earth ions.

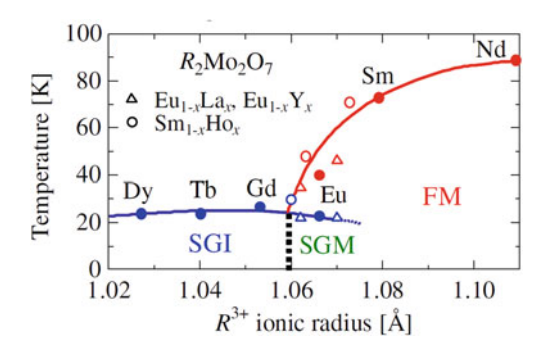


Fig. 1.5 Phase diagram of molybdenum pyrochlore oxides. The horizontal axis is the average ionic radius of the rare-earth ions. FM, SGI, and SGM denote ferromagnetic metal, spin-glass insulator, and spin-glass metal, respectively. (Adapted with permission from Ref. [19], © 2009 APS)

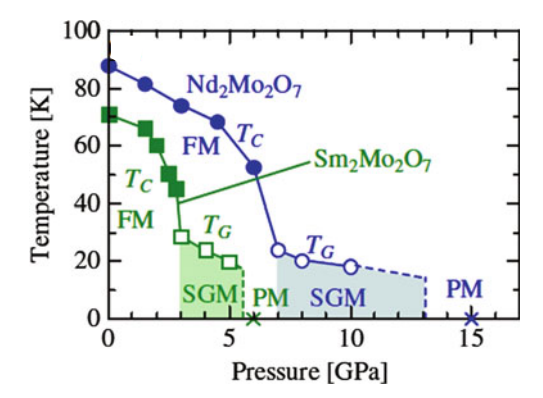


Fig. 1.6 Phase diagram of molybdenum pyrochlore oxides with R = Nd and Sm under the applied hydrostatic pressure. Each line shows the measurement under various external pressure. FM, SGM, and PM denote ferromagnetic metal, spin-glass metal, and paramagnetic metal, respectively. (Adapted with permission from Ref. [19], © 2009 APS)

The low-temperature phases also show a systematic change in application of external pressure [19]. Figure 1.6 shows the phase diagram of  $Nd_2Mo_2O_7$  and  $Sm_2Mo_2O_7$  with application of hydrostatic pressure. Under ambient pressure, the compounds show FM metallic phase below the critical temperature  $T_c$ . With increasing pressure,  $T_c$  decreases and the system turns into a spin-glass metallic state above  $\sim$ 3 and  $\sim$ 7 GPa for Sm and Nd compounds, respectively. Further application of pressure induces another transition, and the system finally enters into a paramagnetic metallic phase under strong pressure. These results indicate that the magnetic behavior of the Mo compounds can be tuned by the substitution of the rare-earth ions or by applying external pressure.

An interesting feature of the Mo compounds is the transport property in the phase competing region. Figure 1.7 shows the temperature dependence of the electrical resistivity. By applying the external pressure to the Nd compound, the temperature dependence of the resistivity gradually weakens and shows nearly temperature independent behavior above 8 GPa. A similar behavior is also seen in the Sm variant, which shows nearly flat behavior above pressure  $\gtrsim 6$  GPa.

The systematic evolution of the low temperature phase was discussed by considering modification of the transfer integrals and the effective super-exchange interaction between Mo ions [19, 44]. In these compounds, the Mo ions are responsible for the phase competition. Each Mo ion has two 4d electrons on average in the  $t_{2g}$  levels which are split by the trigonal crystal field; one of the two electrons is in the lower  $a_{1g}$  level and the other is in the higher  $e_g'$  level. The  $a_{1g}$  electrons are rather localized, and interact with each other through the AFM super-exchange interaction. On the other hand, the  $e_g'$  electrons are itinerant and induce the FM double-exchange interaction between the  $a_{1g}$  spins. The chemical substitution of R and the application of pressure affect the transfer integrals of  $e_g'$  electrons (bandwidth) and the super-exchange interaction between  $a_{1g}$  spins in a complicated manner. The competition between the

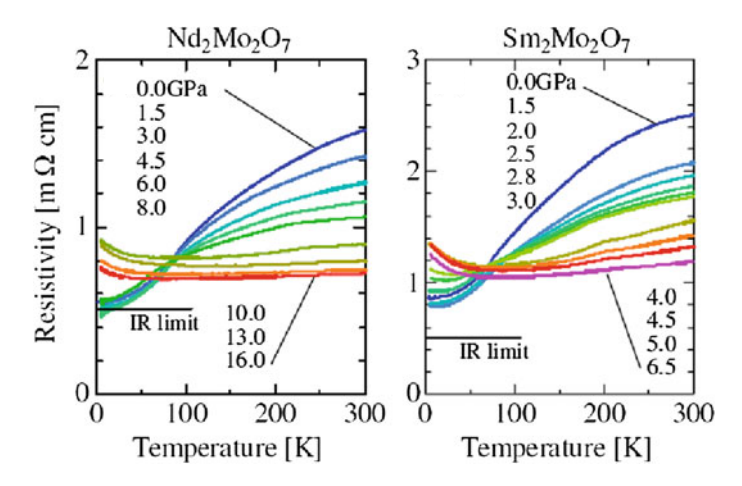


Fig. 1.7 Temperature dependence of the resistivity for Nd and Sm compounds. (Adapted with permission from Ref. [19], © 2009 APS)

two interactions was expected to be the origin of the complicated phase competition in these compounds. It was considered that the chemical substitution mainly affects the bandwidth, while the pressure modifies the superexchange dominantly [19].

Considering the discussions in Sect. 1.1, one may think that the Mo network of  $R_2\mathrm{Mo}_2\mathrm{O}_7$  can be considered as a Kondo lattice model where the  $a_{1g}$  electrons act as the localized spins and only the  $e'_g$  electrons remain itinerant. One, however, need to be careful about whether the discussion in Sect. 1.1 applies to the Mo network. According to the first-principles calculations on the electronic structure of  $R_2\mathrm{Mo}_2\mathrm{O}_7$ , the  $a_{1g}$  band lies typically about 0.5 eV below the Fermi level, and is entangled with the  $e'_g$  bands [44]. This is in contrast to the case of a typical spin-charge coupled system LaMnO<sub>3</sub>, where the localized  $t_{2g}$  bands lie roughly 1.7 eV below the Fermi level and they are well separated from the itinerant  $e_g$  bands [42]. Hence, it might be more like a multi-band Hubbard model then a Kondo lattice model. Nevertheless, the study on the classical-spin Kondo lattice model may be useful in understanding the physics of Mo network, as it has similar mathematical structure to the mean-field type approximations for the Hubbard type models.

Interestingly, a peculiar phase separation between the paramagnetic and the FM ordered states was theoretically reported in a recent study of a double-exchange model on a pyrochlore lattice [34, 35]. The model consists of the double-exchange term and NN AFM super-exchange interaction between the localized spins:

$$H = -\sum_{\langle i,j\rangle,\sigma} t_{ij} (c_{i\sigma}^{\dagger} c_{j\sigma} + \text{H.c.}) + J_{\text{AFM}} \sum_{\langle i,j\rangle} \mathbf{S}_i \cdot \mathbf{S}_j.$$
 (1.29)

Here, the hopping integral  $t_{ij}$  is given by Eq. (1.17) and the sums are for all the NN pairs. By using an unbiased MC simulation described in Sect. 2.2, the phase diagram

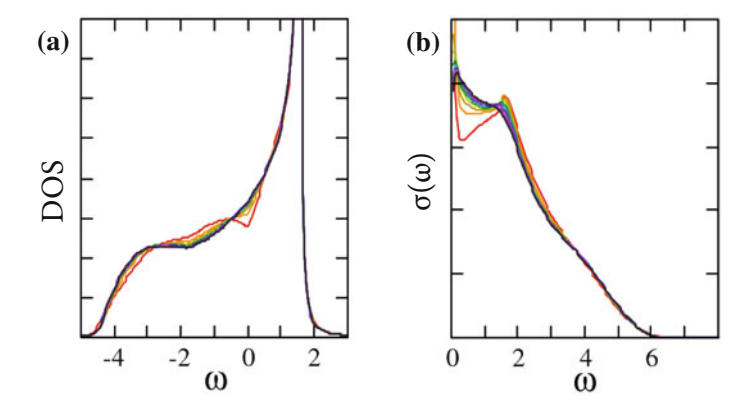


Fig. 1.8 Monte Carlo results of **a** the density of states and **b** the optical conductivity at  $J_{AFM} = 0.1$ . The curves show temperature dependence of each data from T = 0.02 (red) to 0.14 (black). (Adapted with permission from Ref. [35], © 2010 APS)

of the model in Eq. (1.29) was studied throughly. The results indicated that the phase separation between the FM ordered and paramagnetic states appears ubiquitously throughout the phase diagram [34]. This implies that, by tuning the AFM superexchange interaction, the inhomogeneity due to the phase separation is expected to take place on the verge of FM order. Hence, it might be related to the glassy-phase found under application of external pressure (see Fig. 1.6) [19].

In addition, it was also pointed out that the temperature dependence of the electronic and transport properties are suppressed in the phase competing region [35]. Figure 1.8 shows result of MC simulation for  $J_{AFM} = 0.1$ . The results show very weak temperature dependence of the electronic and transport properties from T = 0.04 to 0.14. This behavior is attributed to the suppression of NN interactions by the competition between the double-exchange and super-exchange interactions; the two interactions cancel out and effectively no correlation remains between the NN spins. These results qualitatively account for the diffusive metallic behavior under the external pressure in  $R_2\text{Mo}_2\text{O}_7$  [35].

Meanwhile, the coupling of itinerant electrons on the Mo pyrochlore network with localized magnetic moments at the rare-earth sites lead to another interesting transport phenomena, namely, unconventional anomalous Hall effect [45]. Empirically, the Hall resistivity  $\rho_{\rm H}$  in a metallic compound is known to obey

$$\rho_{\rm H} = R_0 B + 4\pi R_{\rm s} M,\tag{1.30}$$

where B is the external field, M is the magnetization, and  $R_0$  and  $R_s$  are the ordinary and anomalous Hall coefficients, respectively. Thus, the Hall resistivity is expected to increase with both increasing external field and magnetization.

In contrast to this well known behavior, a recent experiment on Nd<sub>2</sub>Mo<sub>2</sub>O<sub>7</sub> observed decrease of Hall resistivity with increasing external magnetic field. It was

argued both experimentally [45, 46] and theoretically [37] that the Berry phase mechanism described in Sect. 1.3.3 is responsible for this behavior. In the Nd compound, the noncoplaner magnetic texture of the Nd localized moments plays a key role. The Nd moments have a spin anisotropy due to the crystal field, and are aligned in the local [111] directions; Nd spins constitute a spin-ice system and develop two-in two-out ice-rule type spin configuration at low temperatures. The noncoplanar spin configuration leads to a finite spin Berry phase. Then the spin-Berry phase may induce the anomalous Hall effect as discussed in Sect. 1.3.3. Thus, in this scenario, the coupling of itinerant electrons to the ice-rule type frustrated localized spins plays a crucial role in the anomalous transport phenomena.

#### $1.4.6 R_2 Ir_2 O_7$

The Ir pyrochlore compounds also show interesting behavior. These compounds also show a systematic change in the metal-insulator transition with respect to the ionic radius of R site [1, 29, 30, 58]. The compounds with small ionic radii exhibit a metal-insulator transition at temperature around 120–140 K. On the other hand, the transition temperature become much lower for compounds with large ionic radii; R = Nd compound show transition at 33 K and no transition is observed for R = Pr.

Among the various compounds in this group, the Pr compound is known for various interesting transport phenomena. Figure 1.9 shows the resistivity and the magnetic susceptibility of a single crystal sample [36]. The resistivity decreases with decreasing temperature above  $100 \, \text{K}$ , indicating the system is metallic. However, the decrease becomes slow below  $\simeq 100 \, \text{K}$ , and the resistivity slightly increases at lower temperatures with showing minimum at  $\simeq 40 \, \text{K}$ . The magnetic susceptibility shows no sign of a phase transition down to  $\simeq 70 \, \text{mK}$ , except for a spin freezing behavior below  $0.12 \, \text{K}$ . Temperature dependence of the susceptibility exhibits peculiar behavior, as shown in Fig. 1.10. At high temperatures, it is well fitted by the Curie-Weiss behavior,

Fig. 1.9 Resistivity and inverse magnetic susceptibility of a single crystal of Pr<sub>2</sub>Ir<sub>2</sub>O<sub>7</sub>. (Adapted with permission from Ref. [36], © 2006 APS)

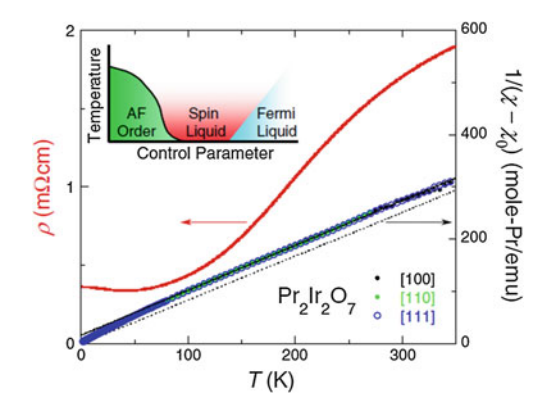


Fig. 1.10 Magnetic susceptibility for a single crystal of  $Pr_2Ir_2O_7$ . (Adapted with permission from Ref. [36], © 2006 APS)

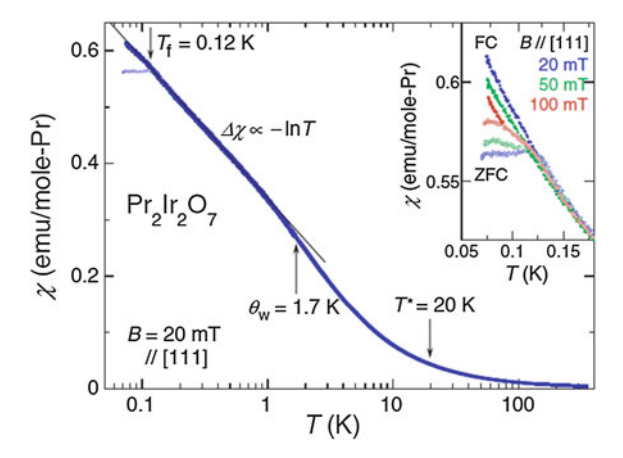
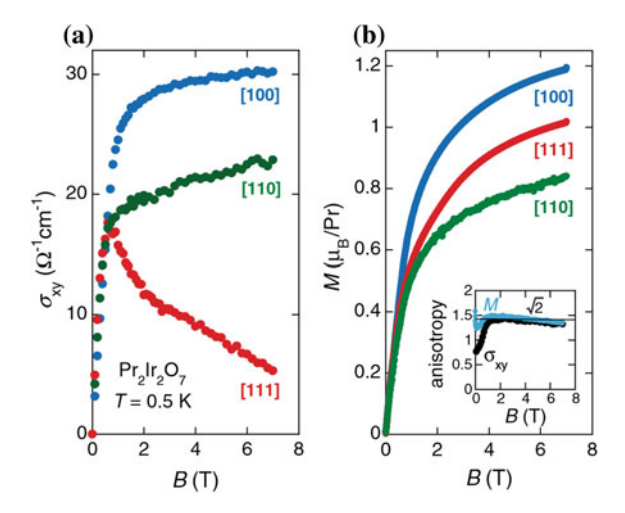


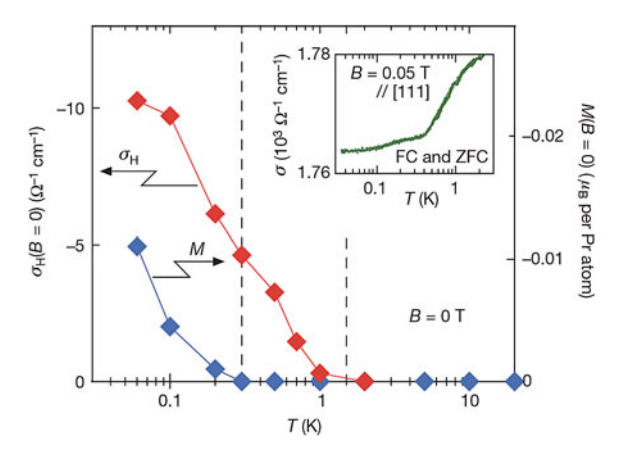
Fig. 1.11 Anisotropic response of Hall conductivity and magnetization with respect to external magnetic field. (Adapted with permission from Ref. [26], © 2007 APS)



and the estimated Curie-Weiss temperature is  $\Theta_W = -20 \,\mathrm{K}$ . In addition, below  $T \simeq 1.7 \,\mathrm{K}$ , the magnetic susceptibility shows a logarithmic temperature dependence. The inset shows strong dependence of the susceptibility on external field upon cooling below  $T = 0.12 \,\mathrm{K}$ , which is a sign of spin freezing [36].

In addition,  $Pr_2Ir_2O_7$  shows peculiar features in the Hall conductivity [26]. Figure 1.11 show the results of the anomalous Hall conductivity (a) and magnetization (b) in applied magnetic field along three different directions, [100], [110], and [111]. While the results for [100] and [110] directions show monotonic increase with respect to the magnetic field, the conductivity along the [111] direction shows non-monotonic behavior similar to that of  $Nd_2Mo_2O_7$ . Clearly, this is in contradiction with the "conventional" anomalous Hall effect, in which the conductivity is proportional to the magnetic moment.

Fig. 1.12 Temperature dependence of magnetization and Hall conductivity. (Adapted with permission from Ref. [27], © 2010 Nature Publishing Group)



Another interesting behavior was recently reported in this compound, in the low temperature conductivity measurement under no external magnetic field [27]. Figure 1.12 shows temperature dependence of spontaneous magnetic moment and Hall conductivity. At the lowest temperature,  $Pr_2Ir_2O_7$  shows a phase transition to a phase with finite magnetic moment and Hall conductivity. The magnetic moment vanishes with increasing the temperature. However, the Hall conductivity appears to remain finite even in the absence of magnetic moment. In Ref. [28], this result was interpreted as a consequence of a novel magnetic state. However, we also note that a recent study on the electronic structure of the Ir electrons argued that a very weak magnetic moments may give rise to strong response in the Hall conductivity, which might be the source of the anomalous Hall effect in  $Pr_2Ir_2O_7$  [33].

As discussed in Sect. 1.4.1, the localized moment of the Pr ion in  $Pr_2Ir_2O_7$  is subject to the strong crystal field, which induces strong Ising-type anisotropy. Hence, an Ising-spin Kondo lattice model is expected to be a good starting point for studying  $Pr_2Ir_2O_7$ . Such a model was studied by simply considering an effective Ising spin model with the RKKY interaction for the fcc electron gas [20]. They studied the phase diagram and temperature dependence of susceptibility using the classical MC simulation, and successfully reproduced the behavior of magnetic susceptibility, negative  $\Theta_W$  in the presence of strong FM NN interaction. More recently, the transport property of an Ising-spin Kondo lattice model was studied, focusing on the resistivity minimum of the  $Pr_2Ir_2O_7$  [10, 55]. There results showed that the development of the ice-rule local correlation gives rise to a minimum in the resistivity.

#### 1.5 Triangular Layered Oxides

Another class of metallic magnets on a frustrated lattice that is known to show interesting magnetic properties are the triangular lattice magnets. One such example is the partially-disordered phase, which is a magnetic order with coexisting

magnetically-ordered sites and paramagnetic/non-magnetic sites. In this section, we review basic aspects of the triangular lattice magnets focusing on the partial disorder in Ising spin systems.

#### 1.5.1 Partially Disordered State

The partially-disordered (PD) state is a magnetic order which magnetically ordered sites and paramagnetic sites are periodically aligned. Figure 1.13 shows schematic pictures of the PD states in an Ising spin model; the up and down arrows show ordered Ising spins and the open circles represent paramagnetic sites. The spins on the paramagnetic sites are thermally fluctuating between the up and down states, hence, they do not contribute to the magnetization.

Historically, the PD state was first studied in an Ising model on the triangular lattice [31]. In the first attempt, an Ising spin model with NN  $(J_1)$  and secondneighbor  $(J_2)$  interactions was considered, with  $J_1$  and  $J_2$  being AFM and FM, respectively. The ground state of this model is a three-sublattice ferrimagnetic (FR) order, which is composed of the honeycomb network of up spins and isolated down spins at the remaining sites. The phase diagram of this model was studied by a mean-field theory, and it was shown that the three-sublattice PD state (Fig. 1.13a) is realized in the finite temperature region in between the low temperature FR ordered state and the high-temperature paramagnetic phase. However, subsequent numerical studies on the  $J_1-J_2$  Ising model on the triangular lattice have reported that the PD state is unstable against thermal fluctuations. In a series of the subsequent studies, the phase diagram of this model was studied extensively using the classical MC simulation for both weak  $J_2$  [11–13, 49, 57] and for  $J_2$  being comparable to  $J_1$ [24]. All of the studies consistently reported the presence of two subsequent phase transitions, similar to those of the mean-field theory. However, based on the finite size scaling analysis [12, 13], MC snap shots [11, 57], and MC time evolution [12, 49, 57], it was claimed that the intermediate phase found in these studies are

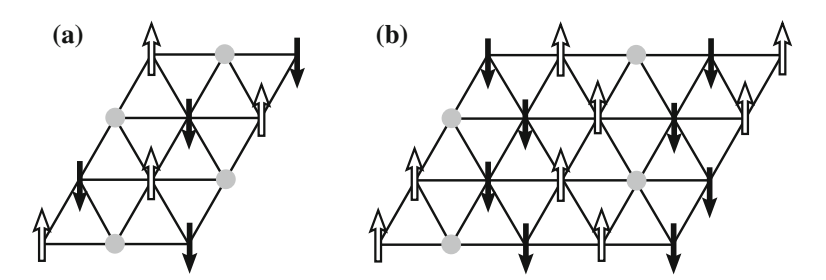


**Fig. 1.13** Schematic picture of the **a** 3-sublattice and **b** 5-sublattice PD state. The *up* and *down arrows* indicate magnetically ordered sites and the *open circles* represent paramagnetic sites. The paramagnetic sites are thermally fluctuating between the up and down states

a Kosterlitz-Thouless type quasi-long-range order, and not a long-range PD state [24].<sup>5</sup> These results consistently show that the PD state is unstable in the  $J_1$ – $J_2$  Ising model on the triangular lattice, and is taken over by a Kosterlitz-Thouless type state.

Later, similar studies for an Ising model on a triangular lattice with third-neighbor interaction [48] and for an Ising model on a kagome lattice with NN  $J_1$  and second-neighbor  $J_2$  interaction were done by using the classical MC method [47]. However, no PD long-range order was found in these models; it was only realized as a quasi-long-range order at the best. These results along with the above MC results on the  $J_1$ - $J_2$  triangular Ising model appear to show that the PD state is unstable in two-dimensional Ising models. So far, the only PD state confirmed is in a three-dimensional model with stacked triangular lattices, in which the interlayer spin-spin coupling being stronger than the intralayer couplings [54].

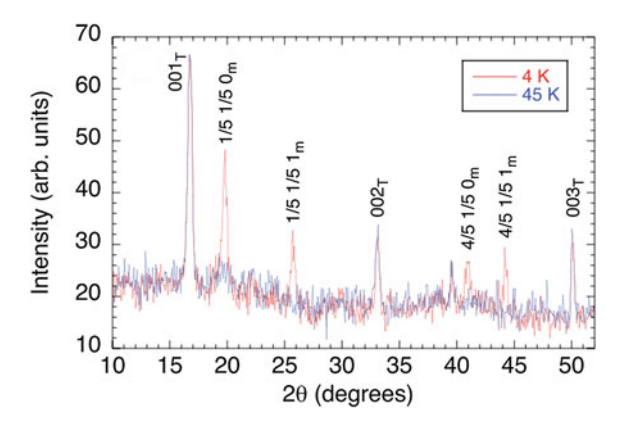
#### $1.5.2 Ag_2CrO_2$

While the theoretical studies on two-dimensional Ising models appear to show that the PD state is not stabilized in two dimensions, a recent experiment on a quasitwo-dimensional oxide Ag<sub>2</sub>CrO<sub>2</sub> has reported an interesting result. Ag<sub>2</sub>CrO<sub>2</sub> is a stacked-triangular lattice compound with a crystal structure similar to delafossite. This compound consists of alternating stacks of the CrO<sub>2</sub> planes and Ag<sub>2</sub> plane, with lattice parameter  $a=2.9298\,\text{Å}$  and  $c=8.6637\,\text{Å}$  at  $T=200\,\text{K}$  [28]. In this compound, the  $Cr^{3+}$  ions have open 3d shells with three electrons per ion. Due to the octahedral coordination of oxygen ions, the 3d orbitals of the  $Cr^{3+}$  ions split into three  $t_{2g}$  and two  $e_g$  orbitals; the three electrons fill up the  $t_{2g}$  orbitals with aligning their spins, which leaves no orbital degrees of freedom. From the hightemperature susceptibility measurement, the effective magnetic moment for Cr3+ ions is experimentally estimated to be 3.55  $\mu_B$  [60], which is close to the spin-only value, 3.87  $\mu_B$ . Hence, it is expected that each  $Cr^{3+}$  layer forms a triangular spin system with S = 3/2. Meanwhile, this magnet is known to be a metal; it is expected that the itinerant electrons are at Ag sites. Thus, this material is a spin-charge coupled system which localized moments on Co site interacts with itinerant electrons on Ag sites.

 $Ag_2CrO_2$  shows a phase transition at  $T_N = 24$  K; the heat capacity measurement shows a sharp peak at  $T_N = 24$  K, indicating a phase transition to an AFM order [60]. A detailed study on the magnetic and crystal structure of the compound was recently conducted by a neutron diffraction technique [28]. Figure 1.14 shows neutron powder diffraction pattern for the  $Ag_2CrO_2$  at T = 4 and 45 K, which are below and above the  $T_N$ , respectively. In addition to the Bragg peaks observed in at 45 K, the

<sup>&</sup>lt;sup>5</sup>We also note that, in these studies, there was some disagreement on the overall structure of the phase diagram. However, all these studies consistently claimed that the high-*T* phase transition is of a Kosterlitz-Thouless type. For further details, see Ref. [24].

Fig. 1.14 Neutron powder diffraction pattern of  $Ag_2CrO_2$  at T = 4 K (below  $T_N$ ) and 45 K (above  $T_N$ ). (Adapted with permission from Ref. [28], © 2012 APS)



result for 4 K shows additional Bragg peaks at  $(\frac{1}{5}\frac{1}{5}l)$  and  $(\frac{4}{5}\frac{1}{5}l)$ . This indicates that a five-sublattice magnetic structure emerges below  $T_N$ . The magnetic Bragg peaks were fitted reasonably well by assuming the five-sublattice PD state in Fig. 1.13b [28]. The unit cell along the c axis remains as the same with the structural one, indicating the FM stacking of the PD triangular layers. In addition, from the structural analysis, it was reported that the compound exhibits a slight distortion of the triangular lattice at  $T_N$ , where the b axis is slightly contracted. The transition is the magnetic ordering accompanied by the lattice distortion, consistent with the anisotropic structure of the five-sublattice order.

#### 1.6 Motivation of This Study

In this chapter, we reviewed some of the basic aspects of the spin-charge coupled systems, where localized moments and itinerant electrons interact with each other. Though the magnetism and transport phenomena in the spin-charge coupled systems have been extensively studied for more than half a century, they still serve as one of the major topics in the field of condensed matter physics. Moreover, recent developments in experimental techniques have opened numbers of new directions in the studies of these systems; from novel magnetic behavior and transport phenomena to industrial applications such as spintronics.

One of such direction is the study of compounds with geometrically frustrated lattice structures. One of the major motivations in the study of these compounds is to explore novel magnetic states and transport phenomena induced by the cooperation of the spin-charge coupling and geometrical structure of the lattices. Indeed, as we discussed in Sects. 1.4 and 1.5, these compounds exhibit various interesting transport and magnetic phenomena.

The main objective of thesis is to theoretically explore the novel phases that are induced by the spin-charge coupling in a geometrically frustrated magnets. While

24 1 Introduction

novel phenomena are anticipated and experimentally observed in the triangular and pyrochlore metallic magnets, much less theoretical studies were done at the beginning of this project. This is contrastive to the case of manganese oxides, where the fundamental properties of its effective model—the double-exchange model—have been extensively studied. To gain an understanding on the fundamental properties of the simplest models, we studied the magnetic phase diagram and electronic properties in this thesis.

In frustrated systems, due to the competition between the interactions, they often induce various nontrivial magnetic states at the low temperature. To clarify these phenomena, through out the study, we intensively used an unbiased Monte Carlo simulation which gives the "numerically exact" solutions to the thermodynamic properties of the model. The method is free from the negative-sign problem that often precludes application of the quantum Monte Carlo method. Hence, we can study the low temperature properties of the fermion models even in the presence of geometrical frustration.

#### 1.7 Structure of This Thesis

The structure of this thesis is as follows. In Chap. 2, we introduce the models and methods; the Ising-spin Kondo lattice models are introduced in Sect. 2.1, and Monte Carlo and variational method we used are described in the subsequent sections. Section 2.5 is devoted to the perturbation theory we used in Chap. 8.

In Chaps. 3–8, we present our theoretical results on the Kondo lattice models on various frustrated lattices. The results on the triangular lattice models are presented in Chaps. 3 and 4. The magnetic behavior of this model is studied in Chap. 3, where we show that this model exhibits the first example of PD state in two dimensions. On the other hand, in Chap. 4, we study the electronic states of itinerant electrons in another magnetic state that appears in the phase diagram of this model, the three-sublattice ferrimagnetic order. We found that the ferrimagnetic order is a half-metal with Dirac electrons.

Chapters 5 and 6 are devoted to the magnetic and transport properties of Kondo lattice models on a kagome lattice. In Chap. 5, we present emergence of a peculiar ferrimagnetic state called the loop liquid state, and its transport properties. On the other hand, we study a spin-ice type Ising-spin Kondo lattice model on a kagome lattice in Chap. 6. We show that, when a local correlation called kagome ice develops, an energy gap opens in the electronic density of states of the itinerant electrons. We call this state the kagome-ice insulator; the electronic states and transport properties are studied in detail. We show that the kagome-ice insulator exhibits finite Hall conductivity.

In the last three chapters, Chaps. 7, 8, and 10, we study spin-ice type Ising-spin Kondo lattice models on a pyrochlore lattice. In Chap. 7, we show the magnetic and electronic properties in the intermediate coupling region, where the coupling between the electrons and spins is weaker than the bandwidth of free electrons. On the other

hand, in Chap. 8, we present emergence of an interesting intermediate phase in the strong coupling limit of the Kondo lattice model. The benchmark of the Monte Carlo method used in these two sections is given in Chap. 9. Finally, Chap. 10 is devoted to the summary.

### References

- 1. N. Aito, M. Soda, Y. Kobayashi, M. Sato, J. Phys. Soc. Jpn. 72, 1226 (2003)
- 2. N. Ali, M.P. Hill, S. Labroo, J.E. Greedan, J. Solid State Chem. 83, 178 (1989)
- 3. P.W. Anderson, H. Hasegawa, Phys. Rev. 100, 675 (1955)
- 4. H. Aoki, T. Sakakibara, K. Matsuhira, Z. Hiroi, J. Phys. Soc. Jpn. 73, 2851 (2004)
- 5. J.D. Bernal, R.H. Fowler, J. Chem. Phys. 1, 515 (1933)
- 6. K. Binder, A.P. Young, Rev. Mod. Phys. **58**, 801 (1986)
- 7. S.T. Bramwell, M.J.P. Gingras, Science 294, 1495 (2001)
- 8. S.T. Bramwell, M.J.P. Gingras, P.C.W. Hildsworth, in *Frustrated Spin Systems*, ed. by H.T. Diep (World Scientific, Singapore, 2005). (Chap. 7)
- 9. C.R. Castelnovo, R. Moessner, S.L. Sondhi, Nature 451, 42 (2008)
- 10. G.W. Chern, S. Maiti, R.M. Fernandes, P. Wölfle, Phys. Rev. Lett. 110, 146602 (2013)
- 11. S. Fujiki, K. Shutoh, Y. Abe, S. Katsura, J. Phys. Soc. Jpn. **52**, 1531 (1983)
- 12. S. Fujiki, K. Shutoh, S. Katsura, J. Phys. Soc. Jpn. 53, 1371 (1984)
- 13. S. Fujiki, K. Shutoh, S. Inawashiro, Y. Abe, S. Katsura, J. Phys. Soc. Jpn. 55, 3326 (1986)
- 14. J.S. Gardner, M.J.P. Gingras, J.E. Greedan, Rev. Mod. Phys. 82, 53 (2010)
- 15. J.E. Greedan, M. Sato, N. Ali, W.R. Datars, J. Solid State Chem. 68, 300 (1987)
- N. Hanasaki, K. Watanabe, T. Ohtsuka, I. Kezsmarki, S. Iguchi, S. Miyasaka, Y. Tokura, Phys. Rev. Lett. 99, 086401 (2007)
- M.J. Harris, S.T. Bramwell, D.F. McMorrow, T. Zeiske, K.W. Godfrey, Phys. Rev. Lett. 79, 2554 (1997)
- 18. R. Higashinaka, H. Fukazawa, K. Deguchi, Y. Maeno, J. Phys. Soc. Jpn. 73, 2845 (2004)
- S. Iguchi, N. Hanasaki, N. Takeshita, C. Terakura, Y. Taguchi, H. Takagi, Y. Tokura, Phys. Rev. Lett. 102, 136407 (2009)
- 20. A. Ikeda, H. Kawamura, J. Phys. Soc. Jpn. 77, 073707 (2008)
- 21. T. Kasuya, Prog. Theor. Phys. 16, 45 (1956)
- 22. T. Katsufuji, H.Y. Hwang, S.-W. Cheong, Phys. Rev. Lett. 84, 1998 (2000)
- 23. M. Kohmoto, Ann. Phys. **160**, 343 (1985)
- 24. D.P. Landau, Phys. Rev. B 27, 5604 (1983)
- 25. D. Loss, P.M. Goldbart, Phys. Rev. B 45, 13544 (1992)
- Y. Machida, S. Nakatsuji, Y. Maeno, T. Tayama, T. Sakakibara, S. Onoda, Phys. Rev. Lett. 98, 057203 (2007)
- 27. Y. Machida, S. Nakatsuji, S. Onoda, T. Tayama, T. Sakakibara, Nature 463, 210 (2010)
- M. Matsuda, C. de la Cruz, H. Yoshida, M. Isobe, R.S. Fishman, Phys. Rev. B 85, 144407 (2012)
- K. Matsuhira, M. Wakeshima, R. Nakanishi, T. Yamada, A. Nakamura, W. Kawano, S. Takagi, Y. Hinatsu, J. Phys. Soc. Jpn. 76, 043706 (2007)
- 30. K. Matsuhira, M. Wakeshima, Y. Hinatsu, S. Takagi, J. Phys. Soc. Jpn. 80, 094701 (2011)
- 31. M. Mekata, J. Phys. Soc. Jpn. 42, 76 (1977)
- 32. R. Melko, M.J.P. Gingras, J. Phys. Condens. Matter 16, R1227 (2004)
- 33. E.-G. Moon, C. Xu, Y.-B. Kim, L. Balents, Phys. Rev. Lett. **111**, 206401 (2013)
- 34. Y. Motome, N. Furukawa, Phys. Rev. B 82, 060407(R) (2010)
- 35. Y. Motome, N. Furukawa, Phys. Rev. Lett. **104**, 106407 (2010)
- S. Nakatsuji, Y. Machida, Y. Maeno, T. Tayama, T. Sakakibara, J. van Duijn, L. Balicas, J.N. Millican, R.T. Macaluso, J.Y. Chan, Phys. Rev. Lett. 96, 087204 (2006)

26 1 Introduction

- 37. K. Ohgushi, S. Murakami, N. Nagaosa, Phys. Rev. B 62, 6065(R) (2000)
- 38. L. Pauling, J. Am. Chem. Soc. 57, 2680 (1935)
- 39. R. Peierls, Quantum Theory of Solids (Clarendon Press, Oxford, 1955)
- A.P. Ramirez, A. Hayashi, R.J. Cava, R. Siddharthan, B.S. Shastry, Nature (London) 399, 333 (1999)
- 41. M.A. Ruderman, C. Kittel, Phys. Rev. **96**, 99 (1954)
- 42. S. Satpathy, Z.S. Popović, F.R. Vukajlović, Phys. Rev. Lett. 76, 960 (1996)
- 43. J.C. Slater, Phys. Rev. **82**, 538 (1951)
- 44. I.V. Solovyev, Phys. Rev. B 67, 174406 (2003)
- 45. Y. Taguchi, Y. Oohara, H. Yoshizawa, N. Nagaosa, Y. Tokura, Science 291, 2573 (2001)
- Y. Taguchi, T. Sasaki, S. Awaji, Y. Iwasa, T. Tayama, T. Sakakibara, S. Iguchi, T. Ito, Y. Tokura, Phys. Rev. Lett. 90, 257202 (2003)
- 47. T. Takagi, M. Mekata, J. Phys. Soc. Jpn. **62**, 3943 (1993)
- 48. T. Takagi, M. Mekata, J. Phys. Soc. Jpn. **64**, 4609 (1995)
- 49. H. Takayama, K. Matsumoto, H. Kawahara, K. Wada, J. Phys. Soc. Jpn. 52, 2888 (1983)
- 50. G. Tatara, H. Kawamura, J. Phys. Soc. Jpn. **71**, 2613 (2002)
- 51. Y. Tokura (ed.), Colossal Magnetoresistive Oxides (CRC Press, Amsterdam, 2000)
- 52. T. Tomizawa, H. Kontani, Phys. Rev. B 80, 100401(R) (2009)
- 53. D.J. Thouless, M. Kohmoto, M.P. Nightingale, M. den Nijs, Phys. Rev. Lett. 49, 405 (1982)
- 54. N. Todoroki, S. Miyashita, J. Phys. Soc. Jpn. 73, 412 (2004)
- 55. M. Udagawa, H. Ishizuka, Y. Motome, Phys. Rev. Lett. **108**, 066406 (2012)
- 56. J. Villain, R. Bidaux, J.-P. Carton, R. Conte, J. Phys. (Paris) 41, 1263 (1980)
- 57. K. Wada, T. Tsukada, T. Ishikawa, J. Phys. Soc. Jpn. **51**, 1331 (1982)
- 58. D. Yanagishima, Y. Maeno, J. Phys. Soc. Jpn. **70**, 2880 (2001)
- J. Ye, Y.B. Kim, A.J. Millis, B.I. Shraiman, P. Majumdar, Z. Tešanovic, Phys. Rev. Lett. 83, 3737 (1999)
- 60. H. Yoshida, E. Takayama-Muromachi, M. Isobe, J. Phys. Soc. Jpn. 80, 123703 (2011)
- 61. K. Yosida, Phys. Rev. 106, 893 (1957)
- 62. C. Zener, Phys. Rev. 82, 403 (1951)

# Chapter 2 Models and Methods

**Abstract** This chapter is devoted to introduce the models and methods we employed in this thesis. We consider Ising-spin Kondo lattice models on frustrated lattices, such as triangular, kagome, and pyrochlore lattices. A strong coupling limit of the Kondo lattice model, double-exchange model, is also introduced. The magnetic and transport properties of these models are numerically studied by using Monte Carlo simulations and variational calculation. Details of these methods are also explained in this chapter. In addition to the numerical calculations on Kondo lattice models, a perturbation approach for deducing the effective spin-spin interactions in the double-exchange models are also explained.

### 2.1 Ising-Spin Kondo Lattice Model

#### 2.1.1 Kondo Lattice Model on Frustrated Lattices

To explore the novel magnetic and transport phenomena that emerge from the competition and/or cooperation of spin-charge coupling and geometrical frustration, we here consider a simple model with these aspects, the Ising-spin Kondo lattice model on geometrically frustrated lattices. The Hamiltonian is given by

$$H = -t \sum_{\langle i,j \rangle, \sigma} (c_{i\sigma}^{\dagger} c_{j\sigma} + \text{H.c.}) - J \sum_{i} \mathbf{S}_{i} \cdot \hat{\sigma}_{i} - \sum_{i} \mathbf{S}_{i} \cdot \mathbf{h}.$$
 (2.1)

The first term represents hopping of itinerant electrons, where  $c_{i\sigma}$  ( $c_{i\sigma}^{\dagger}$ ) is the annihilation (creation) operator of an itinerant electron with spin  $\sigma = \uparrow$ ,  $\downarrow$  at ith site, and t is the transfer integral. The sum  $\langle i, j \rangle$  is taken over NN sites. The second term is the onsite interaction between localized spins and itinerant electrons, where J is the coupling constant (the sign of J does not matter in the present model),

$$\hat{\boldsymbol{\sigma}}_{i} = \sum_{\alpha,\beta} c_{i,\alpha}^{\dagger} \boldsymbol{\sigma}_{\alpha\beta} c_{i\beta} \tag{2.2}$$

© Springer Japan 2015 H. Ishizuka, *Magnetism and Transport Phenomena in Spin-Charge Coupled Systems on Frustrated Lattices*, Springer Theses, DOI 10.1007/978-4-431-55663-3\_2 28 2 Models and Methods

represents the localized Ising spin at *i*th site ( $|\mathbf{S}_i| = 1$ ); and  $\sigma_{\alpha\beta}$  is the vector of Pauli matrices. As we will see in the following sections, along with the models with collinear Ising spins, we also consider the models with different anisotropy axes depending on the sublattices. Hence, the localized spins are denoted by vectors  $\mathbf{S}_i = (S_i^x, S_i^y, S_i^z)$ , where  $S_i^{\gamma}$  ( $\gamma = x, y, z$ ) is the  $\gamma$  component of the *i*th spin. In some sections, we also consider the effect of external magnetic field  $\mathbf{h}$ . The third term in Eq. (2.1) describes the external magnetic field acting on the localized moments. For simplicity, we ignore the effect of magnetic field on the itinerant electrons. This corresponds to the limit in which the localized spins have infinitely large magnetic moments; such a limit is reasonably justified in some realistic situation, such as the rare-earth and transition-metal compounds discussed in the introduction, as they are expected to have large magnetic moments.

### 2.1.2 Strong Coupling Limit

In Chaps. 6 and 8, we consider the strong-*J* limit of Eq. (2.1). In this limit, the spin of each itinerant electron is perfectly polarized along the direction of the localized moment at each site. As a consequence, the spin indices for itinerant electrons are projected out. Instead, the spin-charge coupling modifies the hoppings of itinerant electrons [1, 5]; this limit is known as the double-exchange limit (see Sect. 1.2.2). The Hamiltonian in this limit is given by

$$H = -\sum_{\langle i,j\rangle} (t_{ij}\tilde{c}_i^{\dagger}\tilde{c}_j + \text{H.c.}) - \sum_i \mathbf{h} \cdot \mathbf{S}_i, \tag{2.3}$$

where

$$t_{ij} = t \left( \cos \frac{\theta_i}{2} \cos \frac{\theta_j}{2} + \sin \frac{\theta_i}{2} \sin \frac{\theta_j}{2} e^{-i(\varphi_i - \varphi_j)} \right)$$
 (2.4)

is the hopping matrix element between *i*th and *j*th site modulated by the relative angle between the  $S_i$  and  $S_j$ ;  $(\theta_i, \varphi_i)$  are the polar coordinates for the localized moment at *i*th site;

$$\mathbf{S}_i = (S_i^x, S_i^y, S_i^z) = S(\sin \theta_i \cos \varphi_i, \sin \theta_i \sin \varphi_i, \cos \theta_i). \tag{2.5}$$

#### 2.2 Monte Carlo Simulation

To numerically analyze the models in Eqs. (2.1) and (2.3), we performed an unbiased Monte Carlo (MC) simulation which has been widely used to study similar models [2–4]. The method is generally applicable to the fermion models coupled to classical fields whose Hamiltonian is given in a quadratic form in terms of the fermion

operators. To be specific, however, we particularly consider the case of itinerant electrons coupled to localized spins.

In general, the partition function for such a model is obtained by taking two traces; one is over the classical fields and the other over the fermion degree of freedom. For the present model in Eq. (2.1), the partition function is written as

$$Z = \operatorname{Tr}_{\{\mathbf{S}_i\}} \operatorname{Tr}_{\{c_{i\sigma}, c_{i\sigma}^{\dagger}\}} \exp\left[-\beta \left(H(\{\mathbf{S}_i\}) - \mu \hat{N}_c\right)\right], \tag{2.6}$$

where  $\operatorname{Tr}_{\{\mathbf{S}_i\}}$  and  $\operatorname{Tr}_{\{c_{i\sigma},c_{i\sigma}^{\dagger}\}}$  are the traces over the Ising spins and the electron operators, respectively, and  $H(\{\mathbf{S}_i\})$  is a one-particle Hamiltonian matrix in Eq.(2.1) defined for a given Ising spin configuration  $\{\mathbf{S}_i\} = (\mathbf{S}_1,\mathbf{S}_2,\ldots,\mathbf{S}_N)$  where N is the number of the sites;  $\beta = 1/T$  is inverse temperature,  $\mu$  is the chemical potential, and  $\hat{N}_c = \sum_{i\sigma} c_{i\sigma}^{\dagger} c_{i\sigma}$ . The former trace can be calculated by classical MC sampling of the spin configurations  $\{\mathbf{S}_i\}$  with the Boltzmann weight

$$P(\{\mathbf{S}_i\}) = \frac{1}{Z} \exp\left[-S_{\text{eff}}(\{\mathbf{S}_i\})\right], \qquad (2.7)$$

where the effective action is given by the latter trace in the form

$$S_{\text{eff}}(\{\mathbf{S}_i\}) = -\log\left(\text{Tr}_{\{c_{i\sigma},c_{i\sigma}^{\dagger}\}}\exp\left[-\beta\left(H(\{\mathbf{S}_i\}) - \mu\hat{N}_c\right)\right]\right). \tag{2.8}$$

A straightforward method to calculate the effective action is the numerical diagonalization of  $H(\{S_i\})$  [4]. By using the one-particle eigenvalues for  $H(\{S_i\})$ ,  $\{\varepsilon_{\nu}(\{S_i\})\}$ , the effective action is calculated by

$$S_{\text{eff}}(\{\mathbf{S}_i\}) = \sum_{\nu=1}^{N_{\text{dim}}} F[\varepsilon_{\nu}(\{\mathbf{S}_i\})], \tag{2.9}$$

where  $F[x] = -\log[1 + \exp{\{-\beta(x - \mu)\}}]$  and  $N_{\text{dim}}$  is the dimension of the Hamiltonian ( $N_{\text{dim}} = 2N$  in the present case).

# 2.3 Polynomial Expansion Method

In the polynomial-expansion Monte Carlo (PEMC) method, the sum over the eigenstates is replaced by the integration over the density of states (DOS), and the integral is evaluated by using the polynomial expansion technique [3];

$$S_{\text{eff}}(\{\mathbf{S}_i\}) = \int d\varepsilon \, D_{\{\mathbf{S}_i\}}(\varepsilon) F(\varepsilon) = \sum_m \mu_m f_m, \qquad (2.10)$$

where  $D_{\{S_i\}}$  is DOS for itinerant electrons for a spin configuration  $\{S_i\}$ .

30 2 Models and Methods

In Eq. (2.10), DOS and F are expanded by Chebyshev polynomials as

$$\mu_m = \int_{-1}^1 dx T_m(x) \tilde{D}_{\{\mathbf{S}_i\}}(x) = \text{Tr } T_m[H(\{\mathbf{S}_i\})], \tag{2.11}$$

$$f_m = \frac{-1}{\alpha_m} \int_{-1}^{1} \frac{dx}{\pi \sqrt{1 - x^2}} T_m(x) F(x), \qquad (2.12)$$

where  $\alpha_m = 1$  for m = 0 and otherwise 1/2. Here, DOS is renormalized so that the entire spectrum fits into the range of x = [-1, 1];

$$\tilde{D}_{\{S_i\}}(x) = aD_{\{S_i\}}(ax + b). \tag{2.13}$$

where  $a=(\varepsilon_{\rm top}-\varepsilon_{\rm btm})/2$  and  $b=(\varepsilon_{\rm top}+\varepsilon_{\rm btm})/2$ . In the case of a pyrochlore lattice with finite J/t, we take  $\varepsilon_{\rm top}=2t+J+1$  and  $\varepsilon_{\rm btm}=-6t-J-1$  (we afford a margin of 1 for both  $\varepsilon_{\rm top}$  and  $\varepsilon_{\rm btm}$ ). On the other hand, in the case of  $J/t\to\infty$  limit, we take  $\varepsilon_{\rm top}=2t+1$  and  $\varepsilon_{\rm btm}=-6t-1$ . In Eqs. (2.11) and (2.12), the Chebyshev polynomials  $T_m$  are calculated by using the recursion relation in the form

$$T_m(x) = 2xT_{m-1}(x) - T_{m-2}(x),$$
 (2.14)

with

$$T_0(x) = 1, \ T_1(x) = x.$$
 (2.15)

In the MC update, we choose a single spin (or several spins) randomly and flip it (or them) by probability p, which is given by the standard Metropolis algorithm, i.e.,

$$p = \frac{\exp[-\beta S_{\text{eff}}(\{\mathbf{S}_i\}^f)]}{\exp[-\beta S_{\text{eff}}(\{\mathbf{S}_i\}^i)]}.$$
 (2.16)

Here,  $\{S_i\}^i$  is the initial spin configuration and  $\{S_i\}^f$  is the fliped configuration.

When evaluating  $S_{\rm eff}(\{{\bf S}_i\}^i)$  and  $S_{\rm eff}(\{{\bf S}_i\}^f)$  in PEMC, the Chebyshev moments  $\mu_m$  are evaluated by calculating the Chebyshev polynomials of the Hamiltonian matrix recursively. For the sparse Hamiltonian matrix, the calculation amount of  $\mu_m$  is  $O(N^2 \log N)$ , as the necessary order of polynomials scales as  $\log N$ . In one MC step, we go through the above process N times recursively. Hence, the total cost for one MC step in PEMC is  $O(N^3 \log N)$  [3], which is reduced from  $O(N^4)$  in the Monte Carlo method using the numerical diagonalization.

# 2.3.1 Truncation Algorithm

An efficient way to further reduce the calculation amount is to employ a truncation algorithm [2]. In the truncation procedure, a real-space basis  $\mathbf{e}_i(k) = \delta_{i,k}$  is chosen

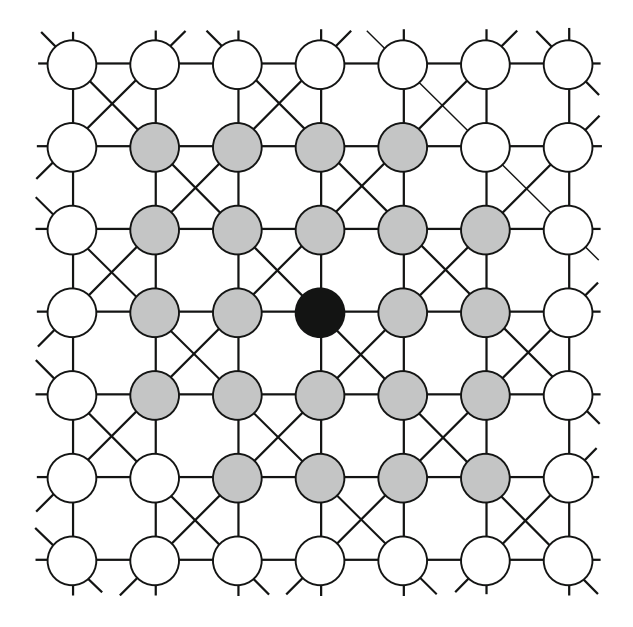
for the trace in Eq. (2.11), where k is a site index. A new vector  $\mathbf{v}_{j}^{(m)}$  is generated by multiplying the unit vector by the mth Chebyshev polynomial of the Hamiltonian, as

$$\mathbf{v}_{j}^{(m)} = T_{m}[H(\{\mathbf{S}_{i}\})]\mathbf{e}_{j} \equiv \sum_{k} v_{j,k}^{(m)} \mathbf{e}_{k}.$$
(2.17)

If the hopping term in the Hamiltonian is limited to nearest-neighbor sites as in Eq. (2.1), the coefficient  $v_{j,k}^{(m)}$  takes a nonzero value only if  $||j-k|| \le m$  is satisfied, where ||j-k|| is the Manhattan distance between two sites j and k. Furthermore, the coefficient usually becomes small quickly as the Mahnattan distance increases. Hence, the vector elements of  $\mathbf{v}_j^{(m)}$  with such small amplitudes can be neglected in the calculation of the moment  $\mu_m$ . In particular, the truncation was done by introducing a threshold for the amplitude of vector elements,  $\epsilon$ , and ignoring the small elements which satisfy  $|v_{j,k}^{(m)}| < \epsilon$  in the calculation of Eq. (2.17) [2]. A similar truncation was also introduced in the trace operation to calculate the effective action  $S_{\mathrm{eff}}(\{\mathbf{S}_i\})$ . This algorithm further reduces the total cost of one MC update to O(N) [2].

In this study, we considered a similar but slightly different truncation algorithm. We carry out the truncation by a real-space distance, not by a magnitude of the vector element in the original scheme; namely, we set a truncation distance d and ignore all contributions out of the range of the Manhattan distance d from a flipped spin. An example of sites within Manhattan distance  $d \le 2$  is shown in Fig. 2.1 for checkerboard lattice. In the present method, the list of sites to be considered in the calculation is known in advance and unchanged throughout the MC simulation. On the other hand, in the previous method, the list needs to be updated by looking at the

Fig. 2.1 Schematic picture of the real-space truncation. The figure shows a projection of the pyrochlore lattice onto a  $\langle 001 \rangle$  plane, and *circles* represent the lattice sites. The *black circle* in the center represents the site with flipped spin. *Gray circles* indicate the sites within the range of the truncation distance d. The picture shows an example of d = 2



32 2 Models and Methods

elements of  $\mathbf{v}_j^{(m)}$  in each MC step. Therefore, the present algorithm is much simpler than the previous one.

In previous studies, this method was shown to be efficient in reducing the computational costs [2]. The benchmark on the efficiency of this method for the model in Eq. (2.1) is presented in Sect. 9. We, however, found that the truncation method is less efficient for the system sizes that we calculated. Hence, we did not use the truncation method, and instead, used the original PEMC method in Chaps. 7 and 8.

### 2.3.2 Physical Quantities

In this algorithm, the calculation of physical quantities related to the localized spin degrees of freedom (e.g., magnetization and its susceptibility) can be done in the same manner as the classical Monte Carlo method. Formally, it is done by replacing the internal energy with  $S_{\text{eff}}(\{S_i\})$ ,

$$\langle O_s \rangle = \frac{1}{Z} \operatorname{Tr}_{\{\mathbf{S}_i\}} O_s \exp\left[-S_{\text{eff}}(\{\mathbf{S}_i\})\right]. \tag{2.18}$$

Here,  $O_s = O_s(\{S_i\})$  is a function for a physical quantity related to spins. The susceptibility for  $O_s$ ,  $\chi_{O_s}$ , is calculated from the fluctuation of  $O_s$ ,

$$\chi_{O_s} = \frac{1}{T} (\langle O_s^2 \rangle - \langle O_s \rangle^2). \tag{2.19}$$

When calculating a physical quantity related to electronic degree of freedom, such as internal energy, the calculation should be done by appropriately taking into account of the Fermi distribution function

$$\langle \hat{O}_e \rangle = \frac{1}{Z} \operatorname{Tr}_{\{\mathbf{S}_i\}} O_e(\{\mathbf{S}_i\}) \exp\left[-S_{\text{eff}}(\{\mathbf{S}_i\})\right], \qquad (2.20)$$

with

$$O_e(\{\mathbf{S}_i\}) = \text{Tr}_{\{c_{i\sigma}, c_{i\sigma}^{\dagger}\}} \hat{O}_e(\{\mathbf{S}_i\}) \exp(-\beta H).$$
 (2.21)

Here,  $O_e(\{S_i\})$  is a physical quantity for itinerant electrons which is given in the quadratic form in terms of  $c_{i\sigma}$ , and  $\text{Tr}_{\{c_{i\sigma},c_{i\sigma}^{\dagger}\}}$  is the trace over the electronic degree of freedom.

As numbers of different parameters are used in each chapter, the details of the actual quantities calculated were described in each chapter separately. We also note that we used different notations as defined in each chapter.

### 2.3.3 Conductivity

To investigate the transport properties, we calculated the conductivity by the standard Kubo formula in a similar manner as in Eq. (2.21). For instance, the optical conductivity along the direction  $\nu$  induced by an electronic field along the direction  $\eta$  was calculated by

$$\sigma_{\eta\nu}(\omega, T) = -i \text{Tr}_{\{\mathbf{S}_i\}} \left[ \sum_{m,n} \frac{f(\varepsilon_n) - f(\varepsilon_m)}{\varepsilon_m - \varepsilon_n} \frac{\langle m | \hat{j}_{\eta} | n \rangle \langle n | \hat{j}_{\nu} | m \rangle}{\omega - \varepsilon_m + \varepsilon_n + i\tau^{-1}} \right], \quad (2.22)$$

where,  $f(\varepsilon)$  is the Fermi distribution function,  $\varepsilon_m$  is the eigenenergy for mth state of itinerant electrons, and  $\tau$  is the scattering rate. Here,

$$\hat{j}_{\eta} = -it \sum_{\langle j,k \rangle,\sigma} (\mathbf{n}_{\eta} \cdot \boldsymbol{\delta}_{j,k}) (c_{k\sigma}^{\dagger} c_{j\sigma} - c_{j\sigma}^{\dagger} c_{k\sigma})$$
 (2.23)

is a current operator in the  $\eta$  direction ( $\eta$  is assigned for each case below), which is constructed in a standard way from a polarization operator in order to satisfy the continuity equation. Here,  $\mathbf{n}_{\eta}$  is the unit vector in the  $\eta$  direction and  $\boldsymbol{\delta}_{j,k}$  is the geometrical vector from jth to kth site. The sum is taken for all the nearest-neighbor pairs. The details on the parameters we used in the calculations are given in each chapter.

#### 2.4 Variational Method

In addition to the MC method introduced in Sects. 2.2 and 2.3, the ground state phase diagrams were studied using a variational method comparing the ground state energy of different magnetically ordered states obtained in the MC simulation.

In the variational calculation, we first calculated the electron density and internal energy for each magnetic orders with varying the chemical potential  $\mu$ . The ground state at different  $\mu$  are obtained by comparing the ground state energy for different magnetic states. The phase diagram with respect to  $\mu$  is then mapped onto the phase diagram with varying n; the phase separation between different magnetic states is determined from the jump of n at the phase boundary. As an example, the variational calculation for the triangular lattice model is presented in Sect. 3.3.4.

# 2.5 Perturbation Method in the Strong Coupling Limit

In the pyrochlore lattice cases in Chaps. 7 and 8, we also derived an effective spin model to analyze the phase diagram. In the weak coupling limit, the perturbation theory in terms of J/t which leads to the RKKY interaction, is expected to be a

34 2 Models and Methods

useful approach; the details of this approach is explained in Sect. 1.2.1 and is used in Chap. 7. On the other hand, in the strong coupling limit, we introduced a perturbation theory in terms of the relative angle of the localized moments. In the strong coupling limit, the hopping integrals for itinerant electrons are modulated by the relative angle of localized moments (Eq. (2.4)). For simplicity, we approximate the hopping Eq. (2.4) by its absolute value

$$\tilde{t}_{ij} = |t_{ij}| = t\sqrt{1 + \cos\theta_i \cos\theta_j + \frac{1}{2}\sin\theta_i \sin\theta_j \cos(\varphi_i - \varphi_j)}$$

$$= t\cos(\theta_{ij}/2),$$
(2.24)

where,  $\theta_{ij}$  is the angle between the *i*th and *j*th spins. In the current models, as the

spins are of Ising type, Eq. (2.25) can be transformed into

$$\tilde{t}_{ij} = t_0 + t_1 \tilde{S}_i \tilde{S}_j \tag{2.26}$$

with

$$t_0 = \frac{1}{2} \left( \cos \frac{\theta_{ij}^0}{2} + \sin \frac{\theta_{ij}^0}{2} \right) \tag{2.27}$$

$$t_1 = \frac{1}{2} \left( \cos \frac{\theta_{ij}^0}{2} - \sin \frac{\theta_{ij}^0}{2} \right),$$
 (2.28)

where  $\theta_{ij}^0$  is the relative angle between the easy axes of neighboring sites and  $\tilde{S}_i = \pm 1$  is the Ising spin on ith site projected onto its anisotropy axis. When  $\theta_{ij}^0 = \pi/2$ , then  $t_1 = 0$ ; hence, the orientation of localized Ising moments does not affect itinerant electrons. When  $\theta_{ij}^0 \sim \pi/2$ ,  $t_1$  remains much smaller than  $t_0$ . As the angle between the two nearest-neighbor spins is  $\sim 109^\circ$  for the spin-ice model considered in Chap. 8, and close to  $\pi/2$ , we performed perturbation theory in terms of  $t_1/t_0$ . Essentially, this perturbation expansion corresponds to the perturbation for  $\Delta \theta_{ij}^0 = \pi/2 - \theta_{ij}^0$ .

#### References

- 1. P.W. Anderson, H. Hasegawa, Phys. Rev. 100, 675 (1955)
- 2. N. Furukawa, Y. Motome, J. Phys. Soc. Jpn. 73, 1482 (2004)
- 3. Y. Motome, N. Furukawa, J. Phys. Soc. Jpn. 68, 3853 (1999)
- S. Yunoki, J. Hu, A.L. Malvezzi, A. Moreo, N. Furukawa, E. Dagotto, Phys. Rev. Lett. 80, 845 (1998)
- 5. C. Zener, Phys. Rev. 82, 403 (1951)

<sup>&</sup>lt;sup>1</sup>In principle, the perturbation expansion can also be done by considering the complex hopping. However, for simplicity, we used the approximation in Eq. (2.25).

# Chapter 3

# Partial Disorder on a Triangular Lattice

**Abstract** In this chapter, we study magnetic and electronic properties of an Ising-spin Kondo lattice model on a triangular lattice. We present that the model shows rich phase diagram with various magnetic phases: two-sublattice stripe, three-sublattice ferrimganetic, and partially disordered states. In addition to these long-range orders, we also found a Kosterlitz-Thouless like quasi-long-range order. In these four states, partial disorder and Kosterlitz-Thouless like states are thermally-induced phases that only apears in intermediate temperature region above other long-range orders. Interestingly, the partially disordered phase is insulating and show charge disproportionation. We also present analysis of a mean-field calculation of the band structure and discuss that the partial disorder in the present model is potentially stabilized by the charge gap formation.

#### 3.1 Model and Method

In this section, we introduce the model and method. The model we consider in this section is described in Sect. 3.1.1. In Sect. 3.1.2, we define the physical quantities that we calculated by the Monte Carlo simulation.

#### 3.1.1 Model

In this chapter, we consider a single-band Kondo lattice model on a triangular lattice with localized Ising moments. The Hamiltonian is given by

$$H = -t \sum_{\langle i,j \rangle, \sigma} (c_{i\sigma}^{\dagger} c_{j\sigma} + \text{H.c.}) + J \sum_{i} \sigma_{i}^{z} S_{i}.$$
 (3.1)

The first term represents hopping of itinerant electrons, where  $c_{i\sigma}$  ( $c_{i\sigma}^{\dagger}$ ) is the annihilation (creation) operator of an itinerant electron with spin  $\sigma = \uparrow$ ,  $\downarrow$  at ith site, and t is the transfer integral. The sum  $\langle i, j \rangle$  is taken over nearest-neighbor (NN) sites on the triangular lattice. The second term is the onsite interaction between localized spins

<sup>©</sup> Springer Japan 2015

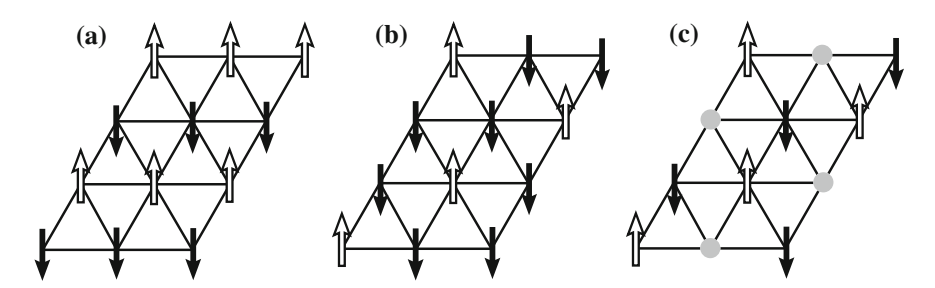


**Fig. 3.1** Schematic pictures of **a** stripe order, **b** ferrimagnetic (FR) order, and **c** partial disorder (PD) on a triangular lattice. The *arrows* show magnetically ordered sites and the circles are thermally fluctuating paramagnetic sites

and itinerant electrons, where  $\sigma_i^z=c_{i\uparrow}^\dagger c_{i\uparrow}-c_{i\downarrow}^\dagger c_{i\downarrow}$  represents the z-component of itinerant electron spin, and  $S_i=\pm 1$  denotes the localized Ising spin at ith site; J is the coupling constant. We take t=1 as the unit of energy, the lattice constant a=1, and the Boltzmann constant  $k_{\rm B}=1$ .

### 3.1.2 Physical Quantities

In this section, the magnetic phase diagram of the model in Eq. (3.1) is studied mainly by a Monte Carlo (MC) simulation introduced in Sect. 2.2. As we will see, the model in Eq. (3.1) shows rich phase diagram with variety of magnetic orders as shown in Fig. 3.1: stripe, three-sublattice ferrimagnetic (FR), and partially disordered (PD) states. In the MC simulation, in principle, these magnetic states can be distinguished by calculating the spin structure factor for the Ising moments,

$$S(\mathbf{q}) = \frac{1}{N} \sum_{i,j} \langle S_i S_j \rangle \exp(i\mathbf{q} \cdot \mathbf{r}_{ij}), \qquad (3.2)$$

where the braket denotes the thermal average in the grand canonical ensemble, and  $\mathbf{r}_{ij}$  is the vector from ith to jth site. The PD state is signaled by peaks of  $S(\mathbf{q})$  at  $\mathbf{q} = \pm (2\pi/3, -2\pi/3)$ , while the FR order develops a peak at  $\mathbf{q} = 0$  in addition to  $\mathbf{q} = \pm (2\pi/3, -2\pi/3)$ . No Bragg peaks develop in the Kosterlitz-Thouless (KT) state as it is a quasi-long-range order. However, it is difficult to distinguish KT phase from a long-range order (LRO) in finite-size calculations, as the correlation length in the KT state is divergent and easily exceeds the system size at low temperature.

To distinguish the FR, PD, and KT instabilities, it is helpful to use the pseudospin defined on three-site unit cell:

$$\tilde{\mathbf{S}}_{m} = \begin{pmatrix} \frac{2}{\sqrt{6}} - \frac{1}{\sqrt{6}} - \frac{1}{\sqrt{6}} \\ 0 & \frac{1}{\sqrt{2}} - \frac{1}{\sqrt{2}} \\ \frac{1}{\sqrt{3}} & \frac{1}{\sqrt{3}} & \frac{1}{\sqrt{3}} \end{pmatrix} \begin{pmatrix} S_{i} \\ S_{j} \\ S_{k} \end{pmatrix}, \tag{3.3}$$

3.1 Model and Method 37

and its summation

$$\tilde{\mathbf{M}} = \frac{3}{N} \sum_{m} \tilde{\mathbf{S}}_{m} \tag{3.4}$$

where m is the index for the three-site unit cells, and (i, j, k) denote the three sites in the mth unit cell belonging to the sublattices (A, B, C), respectively [5, 10]. Then, the three-sublattice PD state (Fig. 3.1c) is characterized by a finite  $\tilde{\mathbf{M}} = (\tilde{M}_x, \tilde{M}_y, \tilde{M}_z)$  parallel to  $(\sqrt{3/2}, 1/\sqrt{2}, 0)$ ,  $(0, \sqrt{2}, 0)$ , or their threefold symmetric directions around the z axis. On the other hand, the three-sublattice FR state (Fig. 3.1b) is characterized by a finite  $\tilde{\mathbf{M}}$  along  $(\sqrt{2/3}, \sqrt{2}, 1/\sqrt{3}), (2\sqrt{2/3}, 0, -1/\sqrt{3}),$  or their threefold symmetric directions around the z axis. Hence, the two states are distinguished by the azimuth of  $\tilde{\mathbf{M}}$  in the xy plane as well as  $M_z$ . In the MC calculations, we measure

$$M_{xy} = \langle (\tilde{M}_x^2 + \tilde{M}_y^2)^{1/2} \rangle,$$
 (3.5)

$$M_z = \langle |\tilde{M}_z| \rangle, \tag{3.6}$$

and the corresponding susceptibilities,

$$\chi_{xy} = \frac{N}{T} (\langle \tilde{M}_x^2 + \tilde{M}_y^2 \rangle - M_{xy}^2),$$
(3.7)

$$\chi_z = \frac{N}{T} (\langle \tilde{M}_z^2 \rangle - M_z^2). \tag{3.8}$$

We also introduce the azimuth parameter of  $\tilde{\mathbf{M}}$  defined by

$$\psi = \mathcal{M}^3 \cos 6\phi_M,\tag{3.9}$$

where  $\phi_M$  is the azimuth of  $\tilde{\mathbf{M}}$  in the xy plane and  $\mathcal{M} = \frac{3}{8}M_{xy}^2$ . The parameter  $\psi$  has a negative value and  $\psi \to -\frac{27}{64}$  for the perfect PD ordering, while it becomes positive and  $\psi \to 1$  for the perfect FR ordering;  $\psi = 0$  for both paramagnetic and KT phases in the thermodynamic limit  $N \to \infty$ .

In PD phase, we also expect to observe finite entropy close to 1/3 of the paramagnetic phase due to the presence of thermally-fluctuating moments. To evaluate the entropy that comes from localized moments, we calculate the spin entropy. The spin entropy per site is defined by

$$\mathcal{S}(T) = -\frac{1}{N} \sum_{\{S_i\}} P(\{S_i\}) \log P(\{S_i\}), \tag{3.10}$$

where  $P(\{S_i\})$  is given by Eq. (2.7), which is the probability for a spin configuration  $\{S_i\}$  to be realized. In the MC calculation, we calculate the temperature derivative of  $\mathcal{S}$ ,

$$\frac{\partial \mathscr{S}(T)}{\partial T} = \frac{1}{NT^2} \left\{ \langle S_{\text{eff}} H \rangle - \langle S_{\text{eff}} \rangle \langle H \rangle \right\},\tag{3.11}$$

and estimate the spin entropy by integrating  $\partial \mathcal{S}(T)/\partial T$ ,

$$\mathscr{S}(T) = \int_0^T \frac{\partial \mathscr{S}(T)}{\partial T} dT = \log 2 - \int_T^\infty \frac{\partial \mathscr{S}(T)}{\partial T} dT. \tag{3.12}$$

In Eq. (3.11),  $S_{\text{eff}}$  is the effective action in Eq. (2.8). In the following calculations, we set the cutoff to 1 for the upper limit of the last integral in Eq. (3.12).

On the other hand, in order to identify the two-sublattice stripe order (Fig. 3.1a), we calculate the order parameter

$$M_{\text{str}} = \left[ \sum_{\mathbf{q}_{\text{str}}^*} \left\{ \frac{S(\mathbf{q}_{\text{str}}^*)}{N} \right\}^2 \right]^{1/2}, \tag{3.13}$$

and its susceptibility  $\chi_{str}$ . Here, the sum is taken for the characteristic wave vectors of the stripe orders running in three different directions,  $\mathbf{q}_{str}^* = (\pi, 0)$  and  $(\pm \frac{1}{2}\pi, \frac{\sqrt{3}}{2}\pi)$ .

In this study, the thermodynamic behavior of itinerant electrons are also studied focusing on charge disproportionation. We compute the charge modulation defined by

$$n_{\rm CO} = \left\{ \frac{N(\mathbf{q}_{\rm CO}^*)}{N} \right\}^{1/2} \tag{3.14}$$

at  $\mathbf{q}_{\text{CO}}^* = (-2\pi/3, 2\pi/\sqrt{3})$ , which corresponds to the wave numbers for the three-sublattice orders. Here,  $N(\mathbf{q})$  is the charge structure factor for itinerant electrons,

$$N(\mathbf{q}) = \frac{1}{N} \sum_{i,j} \langle n_i n_j \rangle \exp(i\mathbf{q} \cdot \mathbf{r}_{ij}), \qquad (3.15)$$

and  $n_i = \frac{1}{2} \sum_{\sigma} c_{i\sigma}^{\dagger} c_{i\sigma}$ .

## 3.2 Mean Field Theory

We first discuss one particle band structure in the PD state by a mean-field approach. We consider a three-sublattice LRO state in Fig. 3.1c. The mean-field Hamiltonian given by

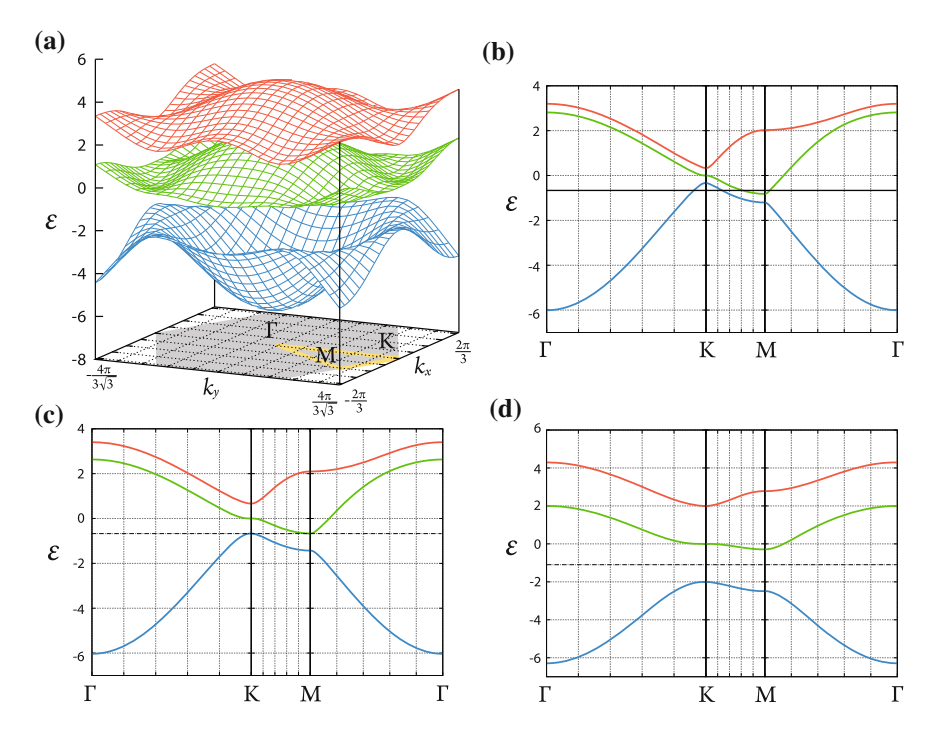


Fig. 3.2 a Mean-field band structure calculated by Eq. (3.16) for the local magnetic field of PD type,  $(\Delta_A, \Delta_B, \Delta_C) = (2, 0, -2)$ . The *gray hexagon* on the basal plane shows the first Brillouin zone for the magnetic supercell. **b–d** Mean-field band structure along the symmetric lines in the local magnetic field of PD type,  $(\Delta_A, \Delta_B, \Delta_C) = (\Delta, 0, -\Delta)$ : **b**  $\Delta = 1/3$ , **c**  $\Delta = 2/3$ , and **d**  $\Delta = 2$ . The *dashed horizontal lines* indicate the Fermi level for n = 1/3

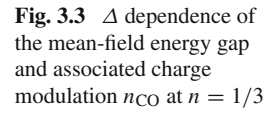
$$\mathcal{H}^{MF} = \sum_{\mathbf{k}} \begin{pmatrix} \Delta_{A} \sigma^{z} & \tau_{\mathbf{k}} & \tau_{\mathbf{k}}^{*} \\ \tau_{\mathbf{k}}^{*} & \Delta_{B} \sigma^{z} & \tau_{\mathbf{k}} \\ \tau_{\mathbf{k}} & \tau_{\mathbf{k}}^{*} & \Delta_{C} \sigma^{z} \end{pmatrix}. \tag{3.16}$$

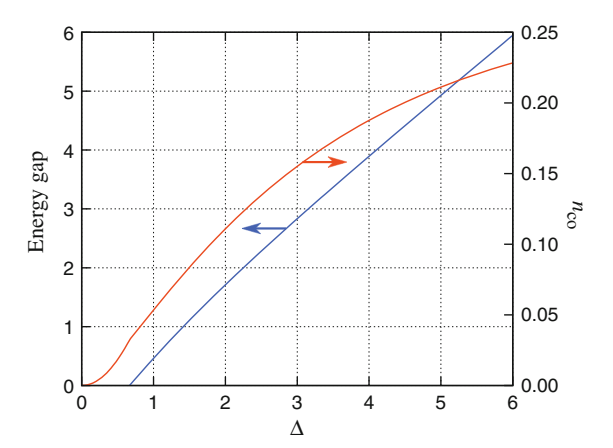
Here, three rows correspond to the different sublattices A, B, and C in the three-site unit cell;  $\Delta_{\alpha}$  is a mean field given by  $J(S_{\alpha})$  ( $\alpha = A, B, C$ ). The sum is taken in the first Brillouin zone for the magnetic unit cell for three-sublattice order.  $\tau_k$  is the hopping term for itinerant electrons given by

$$\tau_{\mathbf{k}} = -t[e^{ik_x} + e^{i\left(-\frac{k_x}{2} + \frac{\sqrt{3}}{2}k_y\right)} + e^{i\left(-\frac{k_x}{2} - \frac{\sqrt{3}}{2}k_y\right)}]$$
(3.17)

and  $\sigma^z$  corresponds to the z component of itinerant electron spin.

If we consider three sublattice FR order, then  $\Delta_{\alpha}$  is given by  $(\Delta_A, \Delta_B, \Delta_C) = (\Delta, \Delta, -\Delta)$ . This case is studied in Sect. 4.2; we show that the electronic structure in the FR order is semimetallic with forming Dirac nodes. In this section, we discuss the band structure for the PD case, where the mean-field is given by  $(\Delta_A, \Delta_B, \Delta_C) = (\Delta, 0, -\Delta)$ . The band structure for  $\Delta = 2$  is shown in Fig. 3.2a. There are three bands





reflecting the three sublattice structure of PD state which all of the bands are doubly degenerate. The first Brillouin zone is shown by the gray shade in the bottom surface. The result shows the presence of an energy gap at the Fermi level corresponding to n = 1/3, that opens between the lowest energy band and the middle band (see also Fig. 3.2d).

Figure 3.2b–d shows the results of band structure while varying  $\Delta$ . The results are plotted along the symmetric line in the Brillouin zone shown in the bottom surface in Fig. 3.2a. When  $\Delta=1/3$ , electron and hole pockets are present at the Fermi level. For  $\Delta=2$ , on the other hand, the system is insulating for n=1/3 (Fig. 3.2d). The pockets in  $\Delta=1/3$  result disappear at  $\Delta=2/3$ ; the band structure for  $\Delta=2/3$  is shown in Fig. 3.2c. Namely, the PD state show metal-insulator transition at  $\Delta_c=2/3$ .

Figure 3.3 shows  $\Delta$  dependence of the energy gap. The charge gap develops for  $\Delta > 2/3$  and monotonically increases, approaching asymptotically a  $\Delta$ -linear form for  $\Delta \gg t$ . The charge modulation is also induced by the inequivalence of sublattices. We plot  $n_{\rm CO}$  (Eq. (3.14)) at n=1/3 in Fig. 3.3. In the PD state, the local charge density at paramagnetic sites become dilute compared to those at the magnetically ordered sites. In the limit of  $\Delta \gg t$ ,  $n_{\rm CO}$  approaches  $n_{\rm CO} = 1/\sqrt{12} \sim 0.289$ .

The results above suggest potential stabilization of PD state by charge gap formation, which does not occure in models with only localized moments. In the previous studies on the Ising spin models [4, 10, 11] and an equivalent classical particle model [8] on a triangular lattice, PD was shown to be unstable against thermal fluctuations and taken over by a KT state. In the case of our model, however, as the KT state lacks a long-range periodic magnetic structure, it is expected that the KT state does not open an energy gap in the electronic state of itinerant electrons. Therefore, there is a chance of stabilizing the PD state by the Slater-type mechanism, that is, by forming an energy gap at the Fermi level with folding the Brillouin zone by forming a magnetic superlattice.

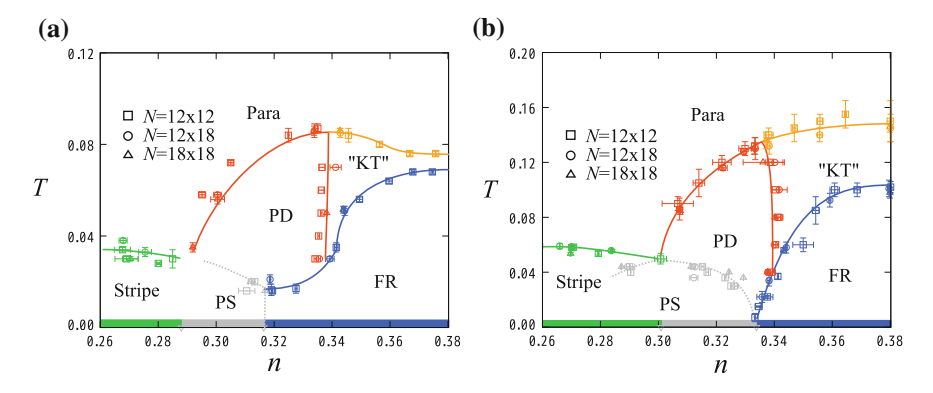
Another point to be noted is that the formation of an energy gap takes place at finite  $\Delta$ . This implies that, if the PD state is stabilized by the charge gap formation, it is expected to appear from a finite J and not remain stable down to  $J \rightarrow 0$ . This is contrasting from magnetic ordering driven by Ruderman-Kittel-Kasuya-Yosida (RKKY) interaction [7, 9, 12]. If the PD state is stabilized by RKKY interaction, it should appear for an infinitesimal J, as RKKY interaction is given by the second-order perturbation in terms of J/t.

#### 3.3 Monte Carlo Simulation

In this section, we study the thermodynamic property of model in Eq. (3.1) by a Monte Carlo simulation. We first show finite-temperature phase diagrams in Sect. 3.3.1, which include four magnetic phases: stripe, PD, FR, and KT-like states. The details of numerical data for the PD state are elaborated in Sect. 3.3.2 and the results for stripe, KT-like, and FR states are discussed in Sect. 3.3.3. The method to determine the phase separation is explained in Sect. 3.3.4.

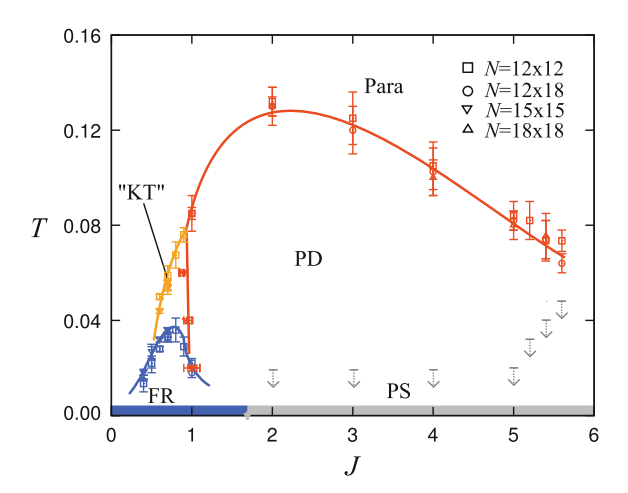
### 3.3.1 Phase Diagrams

Figure 3.4a shows the phase diagram around the electron filling n = 1/3 at J = 1 obtained by MC calculations. The phase diagram is covered with four different phases, stripe, FR, PD, and KT-like, in addition to an electronic phase separation (PS).



**Fig. 3.4** Phase diagrams of the model in Eq. (3.1) while varying n at  $\mathbf{a}$  J=1 and  $\mathbf{b}$  J=2. The *symbols* show phase boundaries for the four phases: stripe, partially disordered (PD), KT-like ("KT"), and ferrimagnetic (FR) phases. PS represents a phase separation. The lines are guides for the eyes. The strips at T=0 show the ground states obtained by comparing the energy of stripe and FR states

Fig. 3.5 Phase diagram of the model in Eq. (3.1) at n = 1/3 while varying J. The notations are common to those in Fig. 3.4. The boundary between PD and PS is difficult to determine by MC calculations, and supposed to be located at lower temperature than indicated by the *gray arrows* 



For relatively low filling of  $n \lesssim 0.29$ , the stripe order with period two (Fig. 3.1a) develops in the low temperature region. On the other hand, for higher filling of  $n \gtrsim 0.32$ , the system exhibits the three-sublattice FR order at low temperature (Fig. 3.1b). We also calculated ground state phase diagram by a variational calculation comparing the ground state energy of the stripe and FR states. Strip at the bottom of the figure shows the result of variational calculation. The details of the results for these orders will be discussed in Sect. 3.3.3.

In addition to these two states, the numerical results show two intermediate-temperature states depending on the electron filling n. For  $0.29 \lesssim n \lesssim 0.34$ , we identify the intermediate phase as the three-sublattice PD state (Fig. 3.1c). Meanwhile, for  $n \gtrsim 0.34$ , we find KT-like behavior similar to the one discussed in the Ising models [4, 5, 8, 10, 11]. In these intermediate-temperature phases, the numerical data indicate a LRO for PD but a quasi-LRO in the KT-like region. The details of PD phase will be discussed in Sect. 3.3.2.

The results for J=2 also show qualitatively similar phase diagram, as shown in Fig. 3.4b. We also find the PD phase in the intermediate-temperature region where stripe and FR orders compete. However, in contrast to the case with J=1, where PD is found widely above the FR state as well as PS, the PD phase dominantly appears above the PS region between the stripe and FR states.

We also investigated the phase diagram of the model in Eq. (3.1) while varying J. Figure 3.5 shows the numerically obtained phase diagram at n=1/3. In the MC simulation, PD state appears for  $J\gtrsim 0.8$ . The transition temperature to PD state increases with increasing J for small J region, and it turns to a gradual decrease with maximum at  $J\sim 2$ . The result shows that the PD state is stable in a wide range of Kondo coupling,  $0.8\lesssim J\lesssim 5.6$ .

An important observation in this phase diagram is that the PD state does not survive to  $J \to 0$ , and it is taken over by the KT-like and FR phases in the small J region. The absence of PD state in the  $J \to 0$  limit implies that the RKKY

interaction in the second-order perturbation theory is insufficient in stabilizing the PD state. Interestingly, the emergence of PD for  $J > J_c \neq 0$  is consistent with the Slater-type mechanism discussed in Sect. 3.2; the MC result of  $J_c \sim 0.8$  is in good accordance with the mean-field argument of the critical value  $\Delta_c = 2/3$ . The result implies that a non-perturbative effect of itinerant electrons plays a crucial role in stabilizing the PD state.

In the PD region in Fig. 3.5, our MC data do not show clear sign of further transition while decreasing temperature before the MC calculations become unstable. In the low temperature region, however, it becomes difficult to determine the chemical potential  $\mu$  for n=1/3. The lowest temperatures of MC calculations are shown in the phase diagram by the gray downward arrows. On the other hand, the analysis of the ground state indicates that the ground state for  $J \lesssim 1.68$  is the FR state, while the region for  $J \gtrsim 1.68$  is PS between the stripe and FR states. In addition, we observe the PS instability by carefully investigating the change of n as a function of  $\mu$  at J=5.4 (see also Sect. 3.3.4). From these facts, at T=0, we conclude that the PD for  $J \gtrsim 1.68$  is taken over by PS between the stripe and FR states. For an estimates of the PS boundary, we merely plotted the lowest temperatures we reached in our constant-n calculations as the upper limit of temperature for the PS instability.

#### 3.3.2 Partial Disorder

Here, we present the details of MC data for identifying the PD state. Figure 3.6 shows T dependences of MC results for different J at n=1/3. To fix n, we tuned  $\mu$  at each temperature; the errors for n at each temperature are controlled within

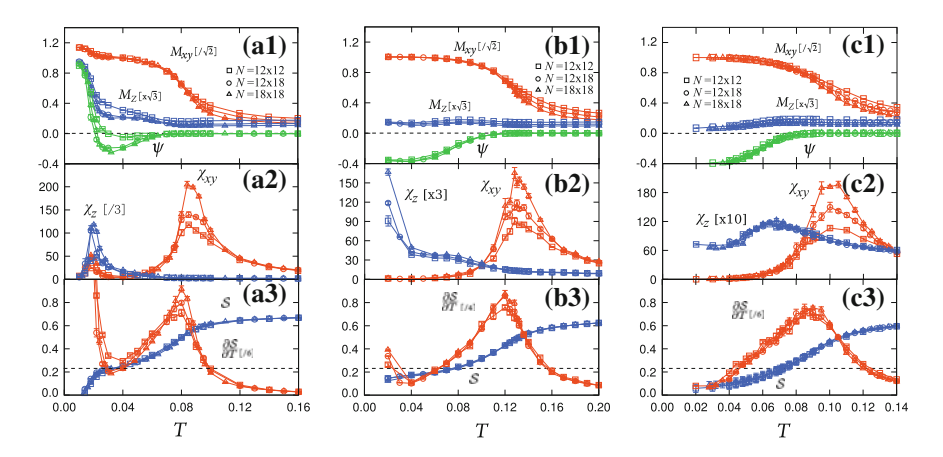


**Fig. 3.6** MC results for (a1)-(c1)  $M_{xy}$ ,  $M_z$ , and  $\psi$ , (a2)-(c2)  $\chi_{xy}$  and  $\chi_z$ , and (a3)-(c3)  $\mathscr S$  and its temperature derivative  $\partial \mathscr S/\partial T$  at n=1/3; (a1)-(a3) J=1, (b1)-(b3) J=2, and (c1)-(c3) J=4. The calculations were done for the system sizes  $N=12\times12$ ,  $12\times18$ , and  $18\times18$ .  $\mathscr S$  is calculated from numerical integration of  $\partial \mathscr S/\partial T$  by assuming  $\mathscr S(T=1)=\log 2$ 

0.001. Figure 3.6a1 is the result for the pseudomoments  $M_{xy}$  and  $M_z$  at J=1[see the definitions in Eqs. (3.5) and (3.6), respectively].  $M_{xy}$  shows two anomalies while decreasing temperature at  $T_c^{(PD)} = 0.086(4)$  and  $T_c^{(FR)} = 0.019(2)$ . The critical temperatures are determined by the peaks of the susceptibilities,  $\chi_{xv}$  and  $\chi_z$ , as mentioned below. At  $T_c^{(\text{PD})}$ ,  $M_{xy}$  rapidly increases and approaches  $\sqrt{2}$  at lower temperatures. In addition, it shows a kink at  $T_c^{(FR)}$  and further increase to 8/3 at lower temperatures. Meanwhile,  $M_z$  shows no anomaly at  $T_c^{(PD)}$ , while it shows a rapid increase to  $1/\sqrt{3}$  at  $T_c^{(FR)}$ . Correspondingly,  $\chi_{xy}$  and  $\chi_z$  in Fig. 3.6a2 also shows divergent peaks increasing with the system size; peaks of  $\chi_{xy}$  appear at both  $T_c^{(PD)}$ and  $T_c^{(FR)}$ , while  $\chi_z$  shows a peak only at  $T_c^{(FR)}$ . These results signal the presence of two successive phase transitions at  $T_c^{(PD)} = 0.086(4)$  and  $T_c^{(FR)} = 0.019(2)$ . The error bars are estimated by the range of temperature where the standard deviation of the MC data exceeds the difference of expectation value from the peak value. The transition temperatures and error bars shown in Figs. 3.4 and 3.5 are given by this criterion. Meanwhile, most of the calculations in Fig. 3.4 were done by fixing  $\mu$ instead of n. Hence, we also give the error bars in terms of n, as n changes with Tin a fixed  $\mu$  calculation.

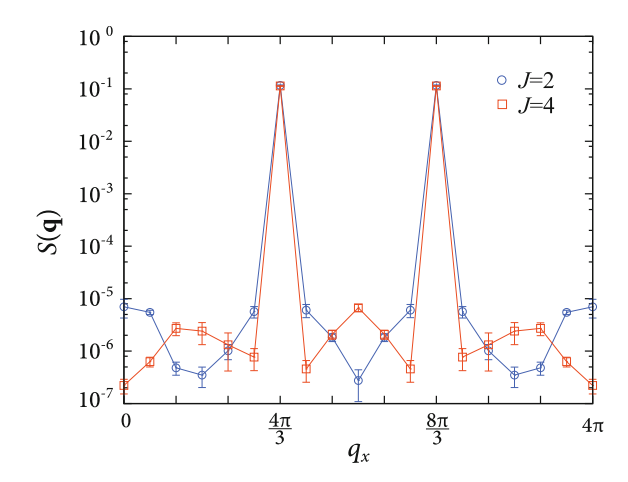
To determine the nature of low temperature phases at n=1/3, we also computed the azimuth parameter  $\psi$  [Eq. (3.9)] shown in Fig. 3.6a1. While increasing the system sizes,  $\psi$  apparently deviates from zero to a negative value below  $T_c^{(\text{PD})}$ , indicating that the intermediate phase for  $T_c^{(\text{FR})} < T < T_c^{(\text{PD})}$  has a PD type order. On the other hand,  $\psi$  shows a sign change at  $T_c^{(\text{FR})}$ , and rapidly increases to  $\psi=1$  at lower temperatures. This is a signature of the FR transition, which will be discussed in detail in Sect. 3.3.3.

The emergence of PD is also seen in the results for the spin entropy  $\mathscr S$  and its temperature derivative [Eqs. (3.12) and (3.11), respectively], as shown in Fig. 3.6a3. In the intermediate-temperature region for  $T_c^{(FR)} < T < T_c^{(PD)}$ ,  $\mathscr S$  appears to approach  $\frac{1}{3}\log 2$  as decreasing temperature, which is the value expected for the ideal PD state where one out of three spins in the magnetic unit cell remains paramagnetic. The remaining entropy is released rapidly at  $T_c^{(FR)}$  and  $\mathscr S \to 0$  at lower temperatures due to the ordering of paramagnetic spins in the FR state.

Similar phase transitions to the PD state are observed in the wide range of J, as shown in Fig. 3.6b1-b3, c1-c3 at J=2 and J=4, respectively. In these results, however, we could not confirm the presence of another phase transition at a lower temperature in the range of temperature we calculated, in contrast to the FR transition found in the case of J=1. As the PD state retains a finite  $\mathscr{S}$ , it is unlikely that this phase survives to  $T\to 0$ . Hence, it is presumably taken over by other ordered phases or PS at a lower temperature. As shown in Fig. 3.5, the variational ground state phase diagram shows PS for the values of J in Fig. 3.6b, c. We, therefore, expect that the PD state is taken over by PS below T=0.02 for  $J\gtrsim 2$ . The situation is indicated by the gray arrows in the phase diagram in Fig. 3.5, as discussed in Sect. 3.3.1.

Another point to be noted is the systematic change in  $\mathscr{S}$  in the PD state by changing J. While the result at J=1 appears to show plateau like behavior at  $\mathscr{S}\sim\frac{1}{3}\log 2$ ,

**Fig. 3.7** MC results for  $S(\mathbf{q})$  along the  $\mathbf{q} = (q_x, 0)$  line at T = 0.02. The calculations were done for the system size  $N = 18 \times 18$ 

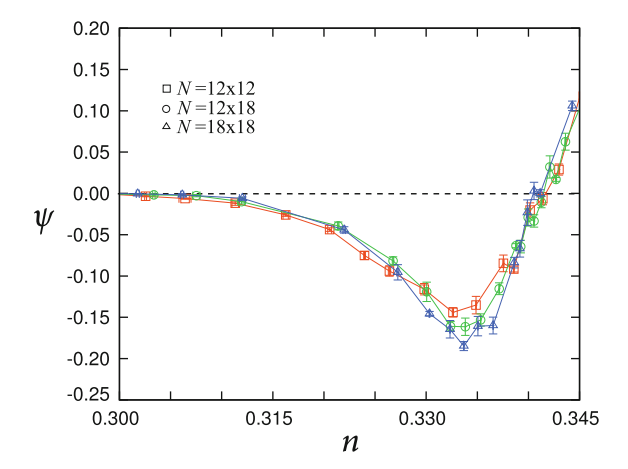


the plateau value of  $\mathscr S$  in the PD state decreases while increasing J, as shown in Fig. 3.6a3, b3, c3. The decrease in  $\mathscr S$  is presumably attributed to the development of spatial correlations between paramagnetic sites in the PD state; the ideal value  $\mathscr S=\frac{1}{3}\log 2$  is for completely uncorrelated paramagnetic spins, and correlations between them reduces the entropy. Such development of correlations is observed in the spin structure factor  $S(\mathbf q)$  defined in Eq. (3.2). Figure 3.7 shows a profile of  $S(\mathbf q)$  calculated by MC simulation at T=0.02. The peaks at  $\mathbf q=(4\pi/3,0)$  and  $(8\pi/3,0)$  indicates that the system is in a three-sublattice ordered phase, while the absence of a sharp peak at  $\mathbf q=(0,0)$  indicates that there is no net magnetic moment; the result is consistent with PD state. When comparing the results at J=2 and J=4, the peak corresponding to the three-sublattice order gets sharper for J=4, while the height of the peak of  $S(\mathbf q)$  is almost the same. This indicates that the PD order at J=2 shows more spin fluctuations than that at J=4, consistent with the trend of the plateau value of  $\mathscr S$ .

Thus far, we showed the results at n=1/3. Next, we show how the PD evolves while changing n. Figure 3.8 shows the MC result of  $\psi$  as a function of n at T=0.08 and J=2.  $\psi$  becomes negative around n=1/3 and takes the lowest value at  $n\simeq 1/3$ . The data indicate that  $\psi$  is almost system size independent or slightly decreases as the system size increases in the finite range of n around n=1/3. Hence, the PD state is stabilized not only at n=1/3 but for a finite range of  $0.31 \lesssim n \lesssim 0.34$  in the thermodynamic limit. The range well agrees with that for the PD phase estimated from the peak of susceptibilities shown in Fig. 3.4b.

With regard to the order of the PD transition, the PD transition in our MC results appears to be continuous, as shown in Fig. 3.6. However, it needs careful consideration, as we will discuss here. It is known that the Ising model on a triangular lattice with antiferromagnetic NN interactions is effectively described by a six-state model, in which the low-energy states with three up-up-down and three up-down-down configurations in the three-site unit cell are described by six-state variables. The PD state in our model also retains six low-energy states with different up-down-paramagnetic

Fig. 3.8 MC results for  $\psi$  while varying n at T=0.08 and J=2. The calculations were done for the system sizes  $N=12\times12, 12\times18$ , and  $18\times18$ 

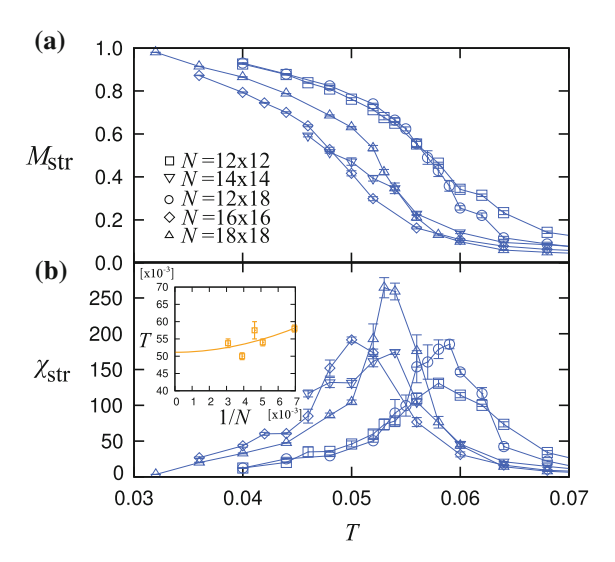


configurations, and hence, the transition to PD is expected to be classified in the framework of six-state models. However, from the argument of duality properties, it is prohibited that the six-state models exhibit a single second-order transition for changing temperature [3]. For instance, a two-dimensional six-state clock model shows two KT transitions at finite temperature [2, 6]. On the other hand, a six-state Potts model shows a weak first order transition to LRO, in which the correlation length reaches the order of 1000 sites at the critical point [1]. In our PD case, the apparently second-order transition at  $T_c^{(PD)}$  is not expected to be a single one, but is always followed by another transition to FR or PS at a lower temperature. This appears not to violate the general argument for the six-state models, although it is not clear to what extent the argument applies, as the electronic PS never takes place in the localized spin models. Hence, the PD transition can be of second order, as indicated in our numerical results. Of course, we cannot exclude the possibility of a weak first order transition, similar to that of the Potts model. In this case, due to a long correlation length at the critical temperature, the system sizes used in our calculations are likely to be insufficient to distinguish the first order transition from second order one.

## 3.3.3 Other Magnetic Orders

Figure 3.9 presents the results for the relatively low filling where the stripe order is stabilized at a low temperature. Figure 3.9a shows the order parameter for the stripe order,  $M_{\rm str}$  (Eq. (3.13)), and Fig. 3.9b shows the corresponding susceptibility  $\chi_{\rm str}$  at J=2 and n=0.27. A phase transition to the stripe phase is characterised by a rapid increase of  $M_{\rm str}$  and corresponding peak of  $\chi_{\rm str}$ . The transition temperature  $T_c^{\rm (str)}$  plotted in the phase diagram in Fig. 3.4a is determined by the peak position

Fig. 3.9 MC results for a  $M_{\rm str}$  and b its susceptibility  $\chi_{\rm str}$  at J=2 and n=0.27. The inset in (b) shows  $T_c^{\rm (str)}$  for different sizes and the solid line is the extrapolation which gives  $T_c^{\rm (str)}=0.051(13)$ . The calculations were done for the system sizes  $N=12\times12,\,14\times14,\,12\times18,\,16\times16,\,$  and  $18\times18$ 



of  $\chi_{\rm str}$ . The error bars are estimated in a similar manner to the case of  $T_c^{\rm (PD)}$  and  $T_c^{\rm (FR)}$ . We also show the system-size extrapolation of  $T_c^{\rm (str)}$  in the inset of Fig. 3.9b. Although the data are rather scattered, we fit them by  $f(N) = a + b/N^c$  with fitting parameters a, b, and c. The extrapolation clearly shows that the phase transition takes place at a finite temperature, as expected for the two-dimensional Ising orders.

With increasing n, the ground state is taken over by the FR state. Figure 3.10 shows the results for at n=0.38 and J=2. The data indicate two successive transitions signaled by the peaks in  $\chi_{xy}$  and  $\chi_z$  at different temperatures. The peak of  $\chi_z$  corresponding to the increase of  $M_z$  signals the phase transition to the FR phase at  $T_c^{(FR)}=0.098(4)$ . At the same time,  $\psi$  becomes finite below  $T_c^{(FR)}$ , and approaches 1, as expected for the FR ordering. Similar behavior was observed at  $T_c^{(FR)}=0.019(2)$  in Fig. 3.6a1, a2. On the other hand, at a higher  $T_{KT}=0.146(4)$ , only  $M_{xy}$  changes rapidly, and correspondingly,  $\chi_{xy}$  shows a peak.  $M_{xy}$ , however, shows a noticeable system-size dependence even below  $T_{KT}$ , in contrast with the results below  $T_c^{(PD)}$ . Similar behavior was observed in the KT transition in Ising spin systems [5, 10].

In these successive transitions,  $\psi$  does not show an anomaly at  $T_{\rm KT}$ , while it shows a sharp rise around  $T_c^{\rm (FR)}$ , as shown in Fig. 3.10a. The value of  $\psi$  extrapolated to large N converges to zero in the intermediate-temperature range. Figure 3.11 shows the extrapolation of  $\psi$  for  $N \to \infty$ . The results indicate that,  $\psi$  remains to be zero at  $N \to \infty$  for  $T \gtrsim 0.104$ , which is far below  $T_{\rm KT} = 0.146(4)$ . On the other hand, the extrapolated value becomes positive finite for  $T \lesssim 0.104$ , reflecting the FR order; the transition temperature is estimated as  $\tilde{T}_c^{\rm (FR)} = 0.102(2)$ , which is in accordance with  $T_c^{\rm (FR)} = 0.098(4)$ .

Fig. 3.10 MC results for a  $M_{xy}$ ,  $M_z$ , and  $\psi$ , b  $\chi_{xy}$  and  $\chi_z$ , and c  $\mathscr{S}$  and its temperature derivative  $\partial \mathscr{S}/\partial T$  at n=0.38 and J=2. The calculations were done for the system sizes  $N=12\times12$ ,  $12\times18$ , and  $18\times18$ 

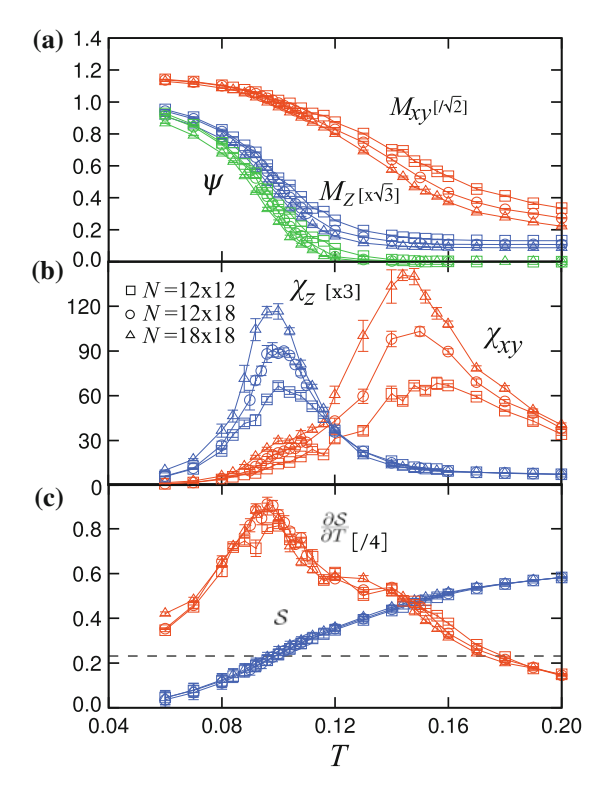
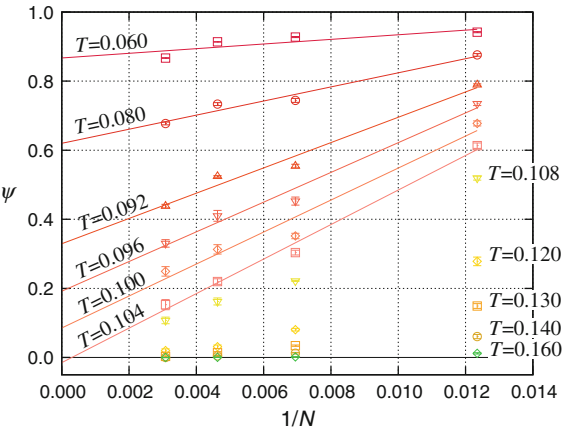
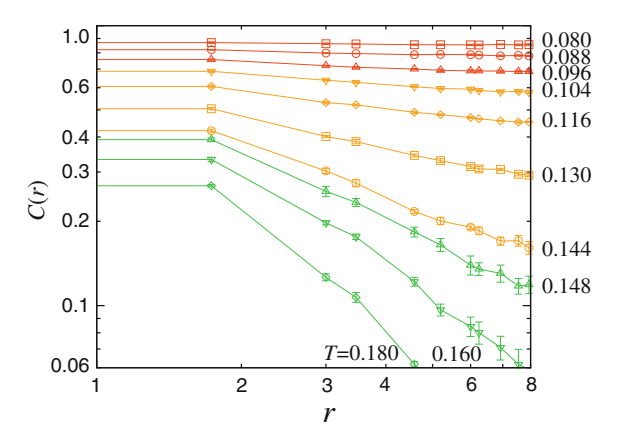


**Fig. 3.11** Extrapolation of  $\psi$  to  $N \to \infty$  at different temperatures. The *solid lines* for  $T \le 0.104$  is the linear fitting of data



The results above indicate that there is no sixfold symmetry breaking in  $M_{xy}$  at  $T_{\rm KT}$ , as seen in the KT phase in the Ising spin models [10]. Hence, we consider that the higher-temperature transition at  $T_{\rm KT}$  is of KT type. Namely, the system exhibits two successive transitions from the paramagnetic phase to the KT-like phase at  $T_{\rm KT}$ ,

Fig. 3.12 MC results for the real-space spin correlation function C(r) at J=2 and n=0.38. The results are shown only for the sites with C(r) > 0. The calculations were done for the system size  $N=18 \times 18$ 



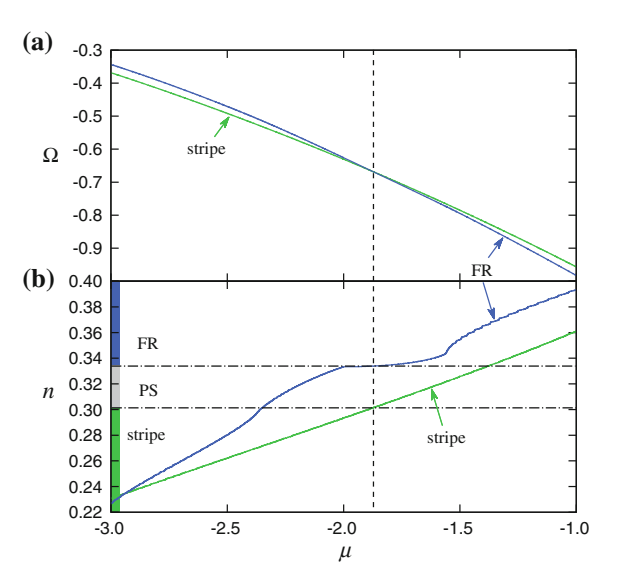
and the KT-like phase to the low-temperature FR phase at  $T_c^{(FR)}$ . Here, we call the intermediate-temperature phase the KT-like phase, as it is difficult to confirm either the KT universality class by critical behavior or the quasi-LRO behavior within the system sizes we reached, as seen below.

The signature of two successive transitions is also observed in the real-space spin correlation function C(r). Here C(r) is the averaged correlations between the Ising spins in distance r, defined by

$$C(r) = \sum_{i,j} \frac{1}{N_{\rm p}(r)} \langle S_i S_j \rangle \delta(|\mathbf{r}_{ij}| - r), \tag{3.18}$$

where  $N_{\rm p}(r)=\sum_{i,j}\delta(|{\bf r}_{ij}|-r)$  is the number of spin pairs with distance r, and  $\delta(x)$  is the delta function. The MC data while varying temperature are shown in Fig. 3.12. Although the results are not conclusive due to the limitation on accessible system sizes, they appear to be consistent with the two transitions discussed above. For  $T\lesssim T_c^{\rm (FR)}=0.098(4)$ , the spin correlation appears to approach constant for large distance, well corresponding to the FR LRO developed in this low temperature region. On the other hand, for  $T\gtrsim T_{\rm KT}=0.146(4)$ , it becomes concave downward with a steep decrease with respect to the distance, which reflects an exponential decay in the high temperature paramagnetic state. In the intermediate region for  $T_c^{\rm (FR)}\lesssim T\lesssim T_{\rm KT}$ , the spin correlation also decays with increasing distance. The decay, however, is much slower and appears to obey an asymptotic power law, which is characteristic to the quasi-LRO in the KT state. In principle, the critical exponents can be estimated from the asymptotic power-law behavior, but it is difficult to be conclusive in the current system sizes.

Fig. 3.13 a The grand potential  $\Omega$  and b electron filling n with respect to the chemical potential  $\mu$ , numerically calculated by exactly diagonalizing the one-body Hamiltonian for itinerant electrons. The results are obtained at J=2 with  $N_s=24\times24$  site superlattice of  $N=12\times12$  site unit cells. The strip at the left side of (b) shows the ground state at the corresponding filling

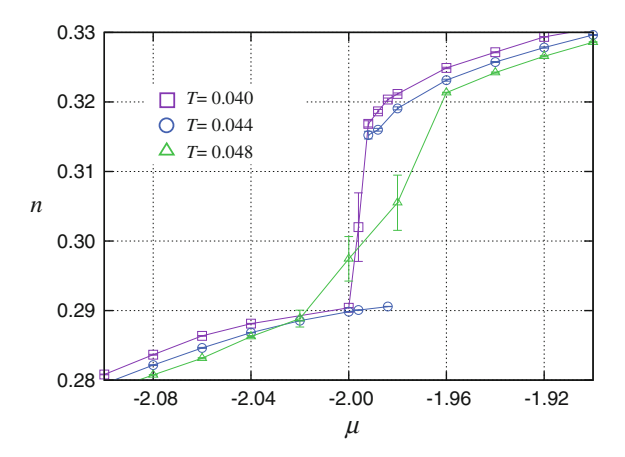


### 3.3.4 Phase Separation

In this section, we present how the PS region was identified in the phase diagram in Figs. 3.4 and 3.5. The ground state phase diagram is obtained by a variational calculation comparing the grand potential per site,  $\Omega = \langle H \rangle / N - 2\mu n$ , where  $\mu$  is the chemical potential and n is the electron filling. Here, we compare  $\Omega$  calculated for the magnetically ordered states found in the MC simulation. The procedure is summarized in Fig. 3.13 at J = 2. Figure 3.13a, b shows the results of  $\Omega$  and n, respectively. For  $\mu \lesssim -1.87$  ( $\mu \gtrsim -1.87$ ),  $\Omega$  for the stripe order is lower (higher) than that for the FR order, indicating that the stripe (FR) state is the ground state in this region. At the critical value of  $\mu \simeq -1.87$ , the electron filling for the two states take different values,  $n \simeq 0.301$  in the stripe state and  $n \simeq 0.334$  in the FR state, as shown in Fig. 3.13b. This indicates that *n* changes discontinuously from  $n \simeq 0.301$ to  $n \simeq 0.334$  at the transition between the stripe and FR states. In other words, the system is unstable in the region of  $0.301 \lesssim n \lesssim 0.334$  against PS between the two states; the range of n is identified as the electronic PS. The PS regions in Fig. 3.4 are determined in this manner. Meanwhile, the PS region at n = 1/3 in Fig. 3.5 is identified by the similar calculations by changing J.

Next, we describe how the PS region is determined at finite temperature in the MC calculation. In the MC simulation using the grand canonical ensemble, PS is characterized by a sudden jump of n while sweeping  $\mu$ . Figure 3.14 shows a typical MC result for n as a function of  $\mu$ . The result at T=0.048 shows a smooth change of

**Fig. 3.14** MC results for n as a function of  $\mu$  at different temperature. The results are for J = 2 and  $N = 12 \times 12$ 



n in the entire region of  $\mu$  in the figure. On the other hand, the results at T=0.040 and 0.044 show a sudden change from  $n\sim0.290$  to 0.315 at  $\mu\sim-1.996$ . We roughly estimate the PS region by the values of n at the both ends of the jump. The results are plotted in the phase diagrams in Fig. 3.4. The range of PS slightly depends on the system size, and hence, we plot the threshold values of n for each system size in the phase diagram.

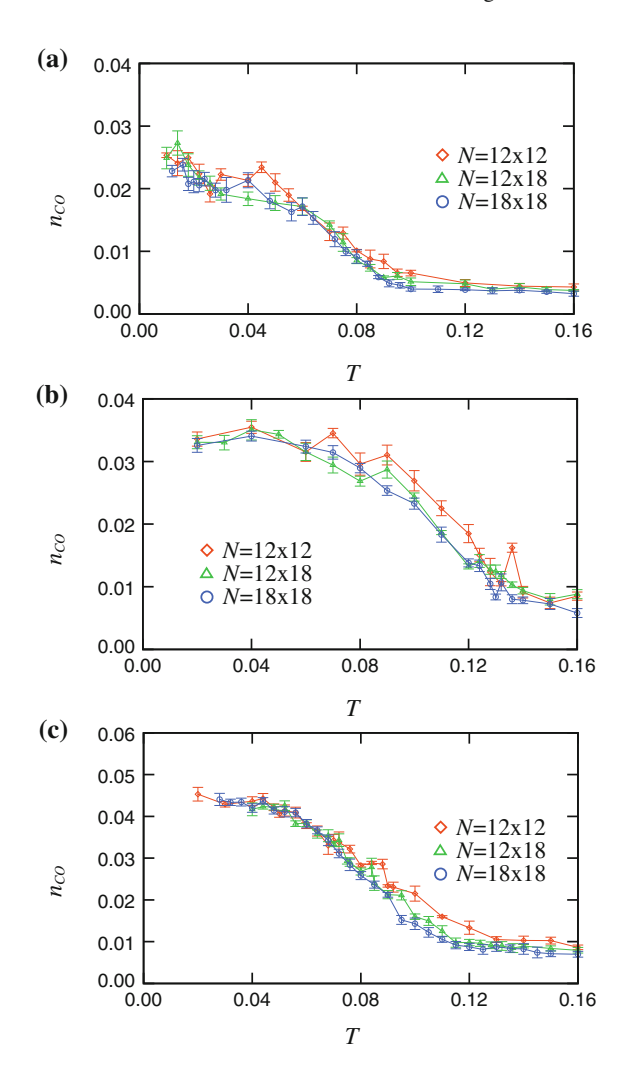
#### 3.4 Electronic State

In the previous sections, we discussed the thermodynamic behavior of the localized spin degree of freedom, with emphasis on the emergence of PD state. In this section, we focus on the behavior in the charge degree of freedom of itinerant electrons in the PD phase.

Figure 3.15 shows temperature dependence of the charge modulation  $n_{\rm CO}$  at n=1/3 for different J. Figure 3.15a is the result at J=1 for different system sizes. The result shows an increase of  $n_{\rm CO}$  below  $T\simeq T_c^{\rm (PD)}=0.086(4)$ , indicating that the PD state is accompanied by charge modulation with period three. Similar onsets of charge modulation at  $T_c^{\rm (PD)}$  are observed for larger J, as shown in Fig. 3.15b, c; the amplitude of the modulation in the PD phase increases monotonically as J increases. The magnitude of the charge modulation is in the same order compared to the mean-field result in Fig. 3.3, while the growth is considerably suppressed by a factor of two to four, presumably because of thermal fluctuations neglected in the mean-field theory.

We next look into the electronic density of states (DOS) at different temperature. Figure 3.16 shows the results for DOS while varying temperature at J=2 and n=1/3. The Fermi level is set at  $\varepsilon=0$ . Here, DOS was calculated by counting the

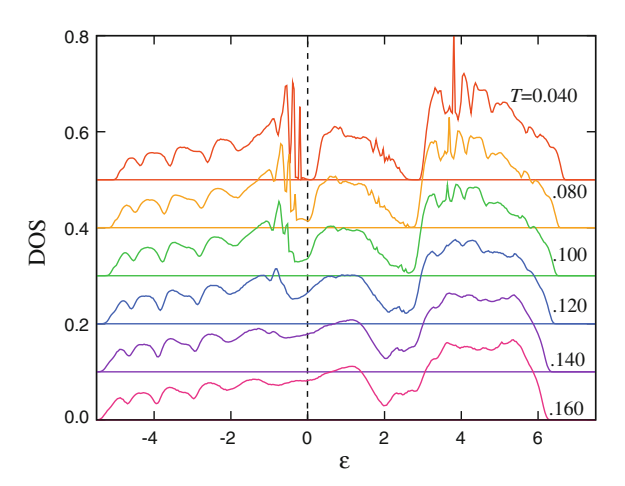
Fig. 3.15 MC results for  $n_{\text{CO}}$  at  $\mathbf{q} = (2\pi/3, -2\pi/3)$  at n = 1/3 and  $\mathbf{a}$  J = 1,  $\mathbf{b}$  J = 2, and  $\mathbf{c}$  J = 4. The calculations were done for the system sizes  $N = 12 \times 12$ ,  $12 \times 18$ , and  $18 \times 18$ 



number of energy eigenvalues as the histogram with the energy interval of 0.0375. In the paramagnetic region for  $T \gtrsim T_c^{(\text{PD})} = 0.130(4)$ , DOS is featureless near the Fermi level. On the other hand, below  $T_c^{(\text{PD})}$ , an energy gap develops at the Fermi level for n=1/3. The result shows that the PD state is an insulator, which supports the scenario that PD is stabilized by the charge gap formation described in Sect. 3.2. Similarly to the charge modulation, the energy gap in the MC results is largely suppressed compared to that obtained by the mean-field analysis in Fig. 3.3. This appears to show the importance of appropriately taking into account of thermal fluctuations.

3.5 Summary 53

**Fig. 3.16** MC results for DOS of itinerant electrons at n = 1/3 and J = 2 for  $N = 18 \times 18$ . The Fermi level is set at  $\varepsilon = 0$ . The statistical errors are comparable to the width of the lines



### 3.5 Summary

To summarize, by a combined analysis of the mean-field type calculation and Monte Carlo simulation, we investigated the origin of the partial disorder in the Ising-spin Kondo lattice model on a two-dimensional triangular lattice. In the mean-field type calculation, we have clarified that a local magnetic field of the partial disorder type induces a metal-insulator transition at 1/3 filling at a critical value of the field. The result suggests that the three-sublattice partial disorder can give rise to an energy gap, and therefore, it has a chance to be stabilized through the Slater-type mechanism. On the other hand, in the Monte Carlo simulation, we have provided numerical results on the emergence of partial disorder at finite temperatures where the stripe phase and the ferrimagnetic order compete with each other. The Monte Carlo results show that the partially disordered state appears above a nonzero value of the spin-charge coupling, and that it is insulating and accompanied by charge disproportionation. The nonzero critical value of the spin-charge coupling and the opening of the charge gap are both qualitatively consistent with the mean-field analysis. The results indicate that the partial disorder is stabilized by the charge gap formation which is often found in itinerant magnets.

#### References

- 1. E. Buffenoir, S. Wallon, J. Phys. A: Math. Gen. 26, 3045 (1993)
- 2. M.S.S. Challa, D.P. Landau, Phys. Rev. B 33, 437 (1986)
- 3. J.L. Cardy, J. Phys. A 13, 1507 (1980)
- 4. S. Fujiki, K. Shutoh, Y. Abe, S. Katsura, J. Phys. Soc. Jpn. 52, 1531 (1983)
- 5. S. Fujiki, K. Shutoh, S. Katsura, J. Phys. Soc. Jpn. **53**, 1371 (1984)
- 6. J.V. José, L.P. Kadanoff, S. Kirkpatrick, D.R. Nelson, Phys. Rev. B 16, 1217 (1977)

- 7. T. Kasuya, Prog. Theor. Phys. 16, 45 (1956)
- 8. D.P. Landau, Phys. Rev. B 27, 5604 (1983)
- 9. M.A. Ruderman, C. Kittel, Phys. Rev. 96, 99 (1954)
- 10. H. Takayama, K. Matsumoto, H. Kawahara, K. Wada, J. Phys. Soc. Jpn. 52, 2888 (1983)
- 11. K. Wada, T. Tsukada, T. Ishikawa, J. Phys. Soc. Jpn. 51, 1331 (1982)
- 12. K. Yosida, Phys. Rev. 106, 893 (1957)

## Chapter 4

# Dirac Half-Metal on a Triangular Lattice

**Abstract** In this section, we study the electronic states in the three-sublattice ferrimagnetic order which appeared in the  $n \gtrsim 1/3$  region of the phase diagram in Chap. 3. We show that the itinerant electrons exhibit the Dirac cone dispersion with half-metallic behavior in the presence of three-sublattice ferrimagnetic order. By variational calculation and Monte Carlo simulation, we demonstrate that the ferrimagnetic order with the Dirac node dominates in the wide range of Kondo coupling and electron density. An experimental realization will be beneficial for spintronics as a candidate for spin-current generator.

#### 4.1 Model and Method

#### 4.1.1 Model

In this section, we consider an Ising-spin Kondo lattice model on a triangular lattice similar to the Hamiltonian studied in Chap. 3:

$$H = -t \sum_{\langle i,j \rangle, \sigma} (c_{i\sigma}^{\dagger} c_{j\sigma} + \text{H.c.}) - J \sum_{i} S_{i}^{z} \sigma_{i}^{z} + J' \sum_{\langle i,j \rangle} \sigma_{i} \cdot \mathbf{S}_{j}.$$
 (4.1)

Here,  $c_{i\sigma}(c_{i\sigma}^{\dagger})$  is the annihilation (creation) operator of an itinerant electron with spin  $\sigma = \uparrow, \downarrow$  at ith site,  $\sigma_i^z = c_{i\uparrow}^{\dagger}c_{i\uparrow} - c_{i\downarrow}^{\dagger}c_{i\downarrow}$  and  $S_i^z$  represent the z component of itinerant and localized spin, respectively. t is the transfer integral, and J and J' are the Kondo coupling. The third term in Eq. (4.1) is the Kondo coupling between nearest-neighbor sites. Hereafter we take t = 1 and  $J, J' \geq 0$ .

#### 4.1.2 Numerical Calculations

For investigating the stability of the ferrimagnetic (FR) order in the ground state, we used a variational calculation in which the ground state energy is compared for different magnetically ordered states. The details of the method is given in Sect. 2.4.

For finite temperature (T) calculation, we used a Monte Carlo (MC) method explained in Sect. 2.2. In this section, we perform calculations with system size up to  $N=18\times18$  sites. For these sizes, we confirmed that the MC method using exact diagonalization is faster than the polynomial expansion method. Hence, we use the exact diagonalization instead of polynomial expansion. The calculations were done for system sizes  $N=12\times12$ ,  $12\times18$ , and  $18\times18$  with typically 9800 Monte Carlo steps after 5000 steps of relaxation.

The magnetic pattern of the ordered phases are primarily investigated by calculating the magnetic structure factor  $S(\mathbf{q})$ . However, as discussed in Chap. 3, the Kondo lattice model on triangular lattice shows rich phase diagram with thermally induced phases, such as partial disorder (PD) and Kosterlitz-Thouless (KT) like states. These states are difficult to be distinguished solely by  $S(\mathbf{q})$ . To distinguish these phases, we use the pseudo-moments and azimuth parameters (see Chap. 3 for further details).

The pseudo-moment is defined by

$$\tilde{\mathbf{S}}_{m} = \begin{pmatrix} \frac{2}{\sqrt{6}} - \frac{1}{\sqrt{6}} - \frac{1}{\sqrt{6}} \\ 0 & \frac{1}{\sqrt{2}} - \frac{1}{\sqrt{2}} \\ \frac{1}{\sqrt{3}} & \frac{1}{\sqrt{3}} & \frac{1}{\sqrt{3}} \end{pmatrix} \begin{pmatrix} S_{i} \\ S_{j} \\ S_{k} \end{pmatrix}, \tag{4.2}$$

where m is the index for the three-site unit cells, and (i, j, k) denote the three sites in the mth unit cell belonging to the sublattices (A, B, C), respectively. We measure the net moment  $\mathbf{M} = (3/N) \sum_{m} \tilde{\mathbf{S}}_{m}$  and its susceptibility. Using the net moment for each MC steps, we define the azimuth parameter  $\psi$  by

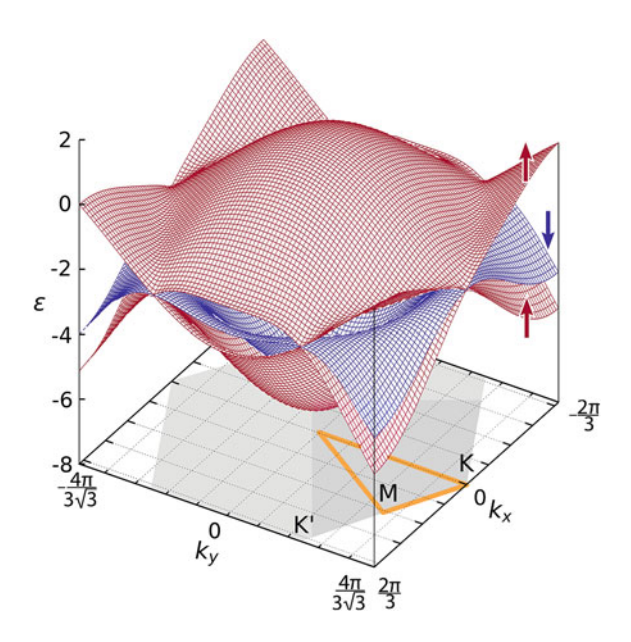
$$\psi = (\tilde{M}_{xy})^3 \cos 6\phi_M,\tag{4.3}$$

$$= \frac{3^3}{8^3} \left( M_x^2 - M_y^2 \right) \left\{ \left( M_x^2 + M_y^2 \right)^2 - \left( 4M_x M_y \right)^2 \right\},\tag{4.4}$$

where  $\phi_M$  is the azimuth angle of **M** in the xy plane and  $\tilde{M}_{xy} = 3M_{xy}^2/8$  ( $M_{xy}^2 = M_x^2 + M_y^2$ ). In Chap. 3, these parameters are used to distinguish PD, KT-like, and three-sublattice FR states. In this section, we focus on the FR state, which is signaled by  $M_{xy} \to 2\sqrt{2/3}$ ,  $|M_z| \to 1/\sqrt{3}$ , and  $\psi \to 1$  at  $T \to 0$ , respectively [2, 5]. Further details on the parameters introduced here is given in Sect. 3.1.

4.2 Band Structure 57

Fig. 4.1 Band structure of the model in Eq. (4.1) under the three-sublattice ferrimagnetic order at J = 2. The figure shows three lower-energy bands at J' = 0 and the arrows indicate the spins for each band. The *gray* shade on the basal plane shows the first Brillouin zone



#### 4.2 Band Structure

In this section, we discuss the itinerant electron bands of the model in Eq. (4.1) in the three-sublattice FR state. By treating the localized moments as classical spins with  $|\mathbf{S}_i| = 1$ , the band structure is calculated by the exact diagonalization of the Hamiltonian. Due to the three sublattice structure of the magnetic order, we get six bands in total, three for up-spin and three for down-spin. The lower three bands of the six bands are shown in Fig. 4.1; the two red bands are up spin bands, and the blue band is of down spin.

The band structure has a notable feature at the energy  $\varepsilon=-J$ . The two up-spin bands touch with each other at the K and K' points in the Brillouin zone forming a Dirac node; the down-spin band has the band top at the same points with an ordinary parabolic dispersion in the vicinity of K and K' points. The enlarged figure of Dirac node is shown in Fig. 4.2a, and the energy dispersion along the symmetric lines in Fig. 4.2b. When the electron filling is at n=1/3, the two lower bands are fully occupied while the remaining bands (including the upper three) are unoccupied; the Fermi level is located at the nodes where the three bands meet. As the down-spin band has an energy gap, the half-metallic Dirac electrons are obtained by electron doping to the unoccupied up-spin band. On the other hand, hole doping hides the Dirac nature as the down-spin band also forms the Fermi surface.

The Dirac node can be energetically isolated from the down spin band by introducing a weak AFM Kondo coupling between the neighboring sites, J'. Figures 4.2c, d show lower three bands of the FR order at J=2 and J'=0.05. Figure 4.2c is the first quadrant of the Brillouin zone, and Fig. 4.2d is the band structure along the symmetric lines. The Fermi level for 1/3 filling is located at the Dirac nodes.

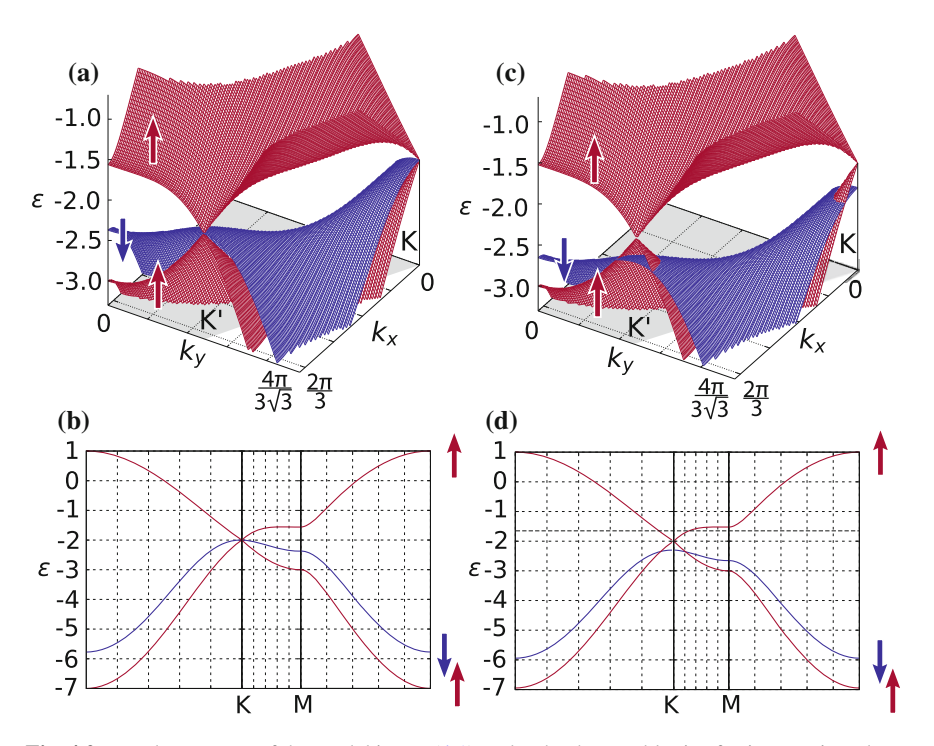


**Fig. 4.2** Band structures of the model in Eq. (4.1) under the three-sublattice ferrimagnetic order at J=2. **a** The enlarged view near the Fermi level  $\varepsilon=-J$  at n=1/3 in the first quadrant, **b** the cut along the symmetric lines, **c** and **d** show the results at J'=0.05. The arrows indicate the spins for each band. The dashed line in **d** indicates the Fermi level in the MC simulation shown in Fig. 4.4

As it is shown, the parabolic down spin band is shifted downward and the Fermi level around 1/3 filling solely comes from the Dirac nodes. We note that the off-site Kondo coupling considered here is significantly small, which are in the order of J/100. In general, an off-site Kondo coupling may exist in the Kondo lattice systems, although the magnitude is expected to be much smaller than the onsite one and the sign depends on the orbital nature of itinerant and localized electrons. As the magnitude of J' considered here is much smaller than that of J, we believe that such value could be realized in magnetic oxides. Hence, the simple FR order on the triangular lattice realizes the Dirac half-metallic state near 1/3 filling.

## 4.3 Low-Energy Effective Hamiltonian

# 4.3.1 k · p Perturbation Theory

In this section, we discuss the low-energy effective Hamiltonian for the itinerant electrons using the  $\mathbf{k} \cdot \mathbf{p}$  perturbation scheme [4]. We show that the low-energy

Hamiltonian for the Dirac nodes in the previous section is exactly the same one as that for the graphene, and hence, it is expected to show similar transport properties.

Under the FR order, the electronic Hamiltonian is given by

$$\mathcal{H} = \sum_{\mathbf{k}} \begin{pmatrix} -J\sigma_A^z & \tau_{\mathbf{k}} & \tau_{\mathbf{k}}^* \\ \tau_{\mathbf{k}}^* & -J\sigma_B^z & \tau_{\mathbf{k}} \\ \tau_{\mathbf{k}} & \tau_{\mathbf{k}}^* & (J+6J')\sigma_C^z \end{pmatrix}. \tag{4.5}$$

Here, the upper two rows correspond to the sites with the up localized moment (A, B sublattices) and the bottom row is for the down one (C sublattice) in the three-site unit cell. In Eq. (4.5),  $\sigma^z$  is the z component of the Pauli matrix for itinerant electrons,  $\mathbf{k}$  is the wave vector, and  $\tau_{\mathbf{k}}$  is the Fourier transform of the hopping term given by

$$\tau_{\mathbf{k}} = -t \left[ e^{ik_x} + e^{i\left(-\frac{k_x}{2} + \frac{\sqrt{3}}{2}k_y\right)} + e^{i\left(-\frac{k_x}{2} - \frac{\sqrt{3}}{2}k_y\right)} \right]. \tag{4.6}$$

Focusing around the K and K' points in the Brillouin zone, we obtain an approximate form of Eq. (4.5) by the  $\mathbf{k} \cdot \mathbf{p}$  perturbation scheme [4]. Expanding  $\tau_{\mathbf{k}}$  to the first order in terms of the relative wave vector  $\kappa$  measured from the K and K' points, the Hamiltonian is rewritten in the form

$$\mathscr{H}_{\mathbf{k}\pm} \simeq \begin{pmatrix} -J\sigma_A^z & \mathrm{i}\frac{3}{2}t\left(\kappa_x \pm \mathrm{i}\kappa_y\right) & -\mathrm{i}\frac{3}{2}t\left(\kappa_x \mp \mathrm{i}\kappa_y\right) \\ -\mathrm{i}\frac{3}{2}t\left(\kappa_x \mp \mathrm{i}\kappa_y\right) & -J\sigma_B^z & \mathrm{i}\frac{3}{2}t\left(\kappa_x \pm \mathrm{i}\kappa_y\right) \\ \mathrm{i}\frac{3}{2}t\left(\kappa_x \pm \mathrm{i}\kappa_y\right) & -\mathrm{i}\frac{3}{2}t\left(\kappa_x \mp \mathrm{i}\kappa_y\right) & \left(J+6J'\right)\sigma_C^z \end{pmatrix}. \tag{4.7}$$

Here, the sign  $\pm$  corresponds to the K and K' points. Then, up to the first order expansion in terms of  $t\kappa_x/J$  and  $t\kappa_y/J$ , Eq. (4.7) is factorized into two parts; one is a localized state at the down-spin sites in the C sublattice, and the other is a  $2 \times 2$  Hamiltonian with the wave functions confined in the up-spin honeycomb subnetwork of the A and B sublattices,

$$\mathcal{H}_{\mathbf{k}\pm}^{\text{Dirac}} = \begin{pmatrix} -J\sigma_A^z & \mathrm{i}\frac{3}{2}t(\kappa_x \pm \mathrm{i}\kappa_y) \\ -\mathrm{i}\frac{3}{2}t(\kappa_x \mp \mathrm{i}\kappa_y) & -J\sigma_B^z \end{pmatrix}. \tag{4.8}$$

This is equivalent to the effective low-energy Hamiltonian of graphene.

# 4.3.2 Condition for the Dirac Half-Metal

From the form of effective low-energy Hamiltonian, it is clear that the Dirac cones are formed immediately by switching on J. When J is small, however, the second lower band for up spin crosses the Fermi level at n=1/3 in the different region in the Brillouin zone from the Dirac points. Hence, there is a band overlap at the energy of the Dirac nodes, and the low-energy physics is not characterized solely by

the massless Dirac fermions. In this section, we consider the condition that the Dirac nodes are energetically isolated at the Fermi level.

In the small J region, the second up-spin band has two local minima: one at the K and K' point, forming the Dirac nodes, and the other at the  $\mathbf{k} = (2\pi/3, 0)$  and its three fold symmetric points. The eigenvalues for these points are given by

$$\varepsilon_K = -(J + 3J') \tag{4.9}$$

for the Dirac node and

$$\varepsilon_{(\frac{2\pi}{3},0)} = \frac{t}{2} - \sqrt{\left(J + 3J' - \frac{t}{2}\right)^2 + 2t^2}$$
 (4.10)

for the  $\mathbf{k}=(2\pi/3,0)$  points. Hence, with sufficiently small J, the energy is lower for the latter, resulting in the band overlap which masks the Dirac nodes. In order to make the Dirac node isolated at the Fermi level,  $\varepsilon_K<\varepsilon_{(\frac{2\pi}{3},0)}$  should be satisfied; this condition is further simplified to

$$J + 3J' > t. \tag{4.11}$$

This condition is important because the necessary J and J' are much smaller than the noninteracting bandwidth 9t. We believe the strength of J and J' given here can be satisfied in materials.

# 4.4 Phase Diagrams

In the discussions above, we assumed the presence of three-sublattice FR order in the model in Eq. (4.1). In this section, we investigate the stability of the FR order in the Kondo-lattice type model.

First, we start by investigating the ground state phase diagram near n=1/3 by a variational calculation. In Chap. 3, we studied the phase diagram of the model in Eq. (4.1) with J'=0 and found that the two-sublattice stripe phase and three-sublattice FR phase competes in the vicinity of 1/3 filling. We compare the ground state energy of these two phases and the ferromagnetic order. The results at J=2 are shown in Fig. 4.3 for J'=0 and 0.05. At J'=0, the ground state in the plotted range is dominated by the FR phase as well as the stripe phase. The different phases are separated by phase separation. As shown in Fig. 4.3b, the introduction of small J' largely stabilizes the FR phase near n=1/3 as well as the stripe phase. This is because the itinerant electron spins are polarized parallel to the localized spins in the ground state, leading to an energy gain (loss) by the AFM J' for the two states (the ferromagnetic state). We note that, in a real compound, the AFM superexchange (SE) coupling between neighboring localized spins, given by  $J_{AF} \sum_{\langle i,j \rangle} \mathbf{S}_i \cdot \mathbf{S}_j$  may

4.4 Phase Diagrams 61

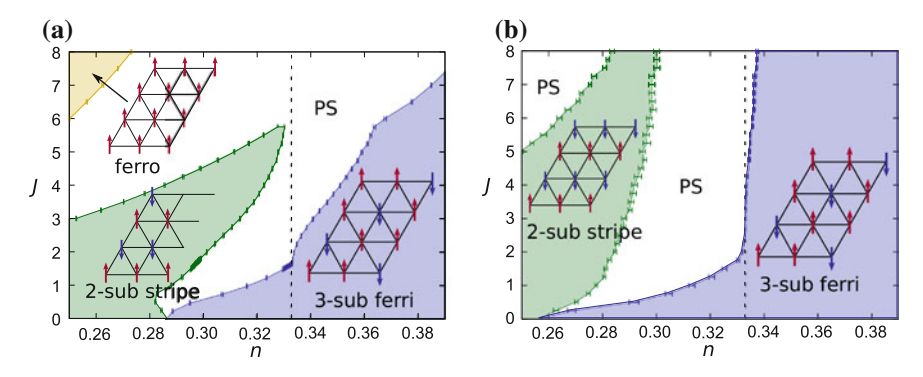
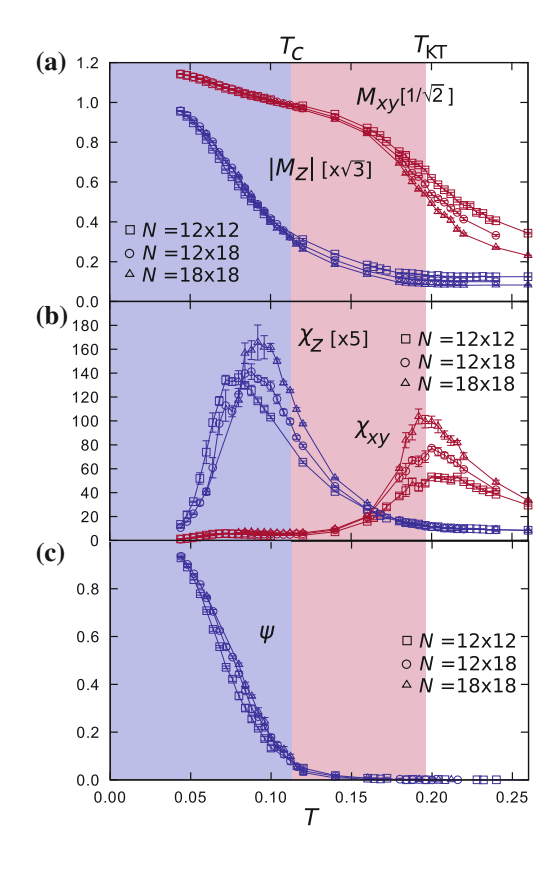


**Fig. 4.3** Ground state phase diagrams obtained by the variational calculation at  $\mathbf{a} \ J' = 0$  and  $\mathbf{b} \ J' = 0.05$ . The schematic picture of magnetic structure in each phase is shown. The white region indicates the electronic phase separation (PS) and the dotted vertical lines indicate n = 1/3

**Fig. 4.4** MC results for **a** the pseudo moments  $M_{xy}$  and  $|M_z|$ , **b** corresponding susceptibilities  $\chi_{xy}$  and  $\chi_z$ , **c** azimuth parameter  $\psi$ . The data are calculated at n = 0.34



also exist. However, in the current case, it neither modifies the band structure nor harms the stability of the FR state. This could be understood from the fact that the AFM SE interaction affects stripe and FR order in exactly the same way. As the phase competition around n=1/3 is between stripe and FR order, the AFM SE interaction do not affects the phase boundary.

We next investigate the finite temperature region using the MC calculation. As the results for J'=0 are already presented in Chap. 3, we here present the results only for finite J' and show that weak J' does not make qualitative change in the finite T behavior. Figure 4.4 shows the MC results at J=2 and J'=0.05 in the slightly electron doped region to n=1/3 (see also Fig. 4.2d). The results indicate two successive phase transitions at  $T_{\rm KT}=0.192(15)$  and at  $T_c=0.108(9)$ . The transition temperatures are estimated by extrapolating the peak of susceptibilities  $\chi_{xy}$  and  $\chi_z$  as  $N\to\infty$ . The transition at  $T_{\rm KT}$  is considered as a KT type with the growth of quasi-long-range order (see Sect. 3.3.3). On the other hand, the phase transition at  $T_c$  is a three-sublattice FR ordering. The MC result and the above analysis for the ground state consistently indicate that the three-sublattice FR order is stabilized in the vicinity of n=1/3 in the wide range of parameters for J and J', spontaneously giving rise to the Dirac half-metal.

# 4.5 Discussion and Summary

In this chapter, we discussed emergence of a Dirac half-metal in an Ising-spin Kondo lattice model on a triangular lattice. By the analysis on the electronic state, we showed that a three-sublattice ferrimagnetic order in a triangular lattice gives rise to half-metallic Dirac nodes at the Fermi level for 1/3 filling. In addition, we performed variational calculation and Monte Carlo simulation and showed that the ferrimagnetic order is stabilized in the vicinity of electron filling 1/3. The results consistently shows that the Dirac half-metal to be realized in the Ising-spin Kondo lattice model.

These results may also be interesting from experimental point of view. Theoretically, a trivial approach to the spin-polarized Dirac node is to consider ferromagnetic Kondo lattice model that couples localized moments to itinerant electrons with Dirac nodes in their single particle bands, such as single-band tight binding model on a honeycomb or kagome lattice.

In the honeycomb and kagome models, when J is sufficiently strong compared to the bandwidth, a ferromagnetic ground state is realized by the double-exchange mechanism [1, 7] we discussed in Sect. 1.2.2. This ferromagnetic state is expected to be stable for wide range of electron fillings. In this ferromagnetic state, the itinerant electron bands split into two according to the spins; each band has exactly the same form as that for the noninteracting case J=0. This is due to the strong ferromagnetic Kondo coupling. Hence, we expect to find half-metallic Dirac electrons in double-exchange systems on a honeycomb or kagome lattice. However, these situations are expected to be very difficult to realize in materials as a strong exchange interaction or the honeycomb and kagome structures is rare in magnetic compounds.

In the triangular lattice compounds, the ferrimagnetic state we considered in this chapter is a well known magnetic state in triangular Ising antiferromagnet, and such state was also observed in several insulating magnets [3, 6]. Hence, our results in the minimal model will stimulate the hunt for Dirac half-metal in transition-metal and rare-earth compounds. The present results is expected to be qualitatively robust even when extending the model to more realistic situations. For instance, the FR state remains stable when including the transverse components of localized spins, at least, in the presence of the Ising anisotropy. Multi-band effect may be avoided under a particular crystal field; for instance, the d-electron  $a_{1g}$  orbital isolated by a strong trigonal field is a good candidate for the realization. Our results here also suggest the possibility of realizing the exotic electronic state in transition-metal and rare-earth compounds, which generally retain much higher controllable degrees of freedom than the well known Dirac electron systems such as graphene.

#### References

- 1. P.W. Anderson, H. Hasegawa, Phys. Rev. 100, 675 (1955)
- 2. S. Fujiki, K. Shutoh, S. Inawashiro, Y. Abe, S. Katsura, J. Phys. Soc. Jpn. 55, 3326 (1986)
- J. Iida, M. Tanaka, Y. Nakagawa, S. Funahash, N. Kimizuka, S. Takekawa, J. Phys. Soc. Jpn. 62, 1723 (1993)
- 4. G.W. Semenoff, Phys. Rev. 53, 2449 (1984)
- 5. H. Takayama, K. Matsumoto, H. Kawahara, K. Wada, J. Phys. Soc. Jpn. 52, 2888 (1983)
- 6. M. Tanaka, H. Iwasaki, K. Siratori, I. Shindo, J. Phys. Soc. Jpn. 58, 1433 (1989)
- 7. C. Zener, Phys. Rev. **82**, 403 (1951)

# **Chapter 5 Thermally-Induced Phases on a Kagome**

**Abstract** In this chapter, we consider an Ising-spin Kondo lattice model on a kagome lattice. The model shares some of the fundamental characters with the triangular model considered in Chaps. 3 and 4; both the triangular and kagome lattices consist of triangular units, and the two models show geometrical frustration when the nearest-neighbor interaction is antiferromagnetic. We show that this kagome lattice model exhibits a rich phase diagram with various thermally-induced phases: loop-liquid state,  $\sqrt{3} \times \sqrt{3}$  partially-disordered state, and partial ferromagnetic state. Among these phases, loop-liquid state is a novel ferrimagnetic state, which possesses a fractional magnetic moment but the system remains disordered due to thermal fluctuations. We also discuss the similarity and differences of the partially-disordered state in kagome and triangular lattice models.

#### 5.1 Model and Method

#### 5.1.1 Model

Lattice

We consider a single-band Kondo lattice model on a kagome lattice with localized Ising spin moments. The Hamiltonian is given by

$$H = -t \sum_{\langle i,j \rangle, \sigma} (c_{i\sigma}^{\dagger} c_{j\sigma} + \text{H.c.}) + J \sum_{i} \sigma_{i}^{z} S_{i}.$$
 (5.1)

Here, the first term is hopping of itinerant electrons, where  $c_{i\sigma}$  ( $c_{i\sigma}^{\dagger}$ ) is the annihilation (creation) operator of itinerant electron with spin  $\sigma = \uparrow$ ,  $\downarrow$  at the ith site, and t is the transfer integral. The sum  $\langle i,j \rangle$  is taken over nearest-neighbor (NN) sites on the kagome lattice. The second term is the on-site Kondo coupling between localized Ising spins and itinerant electrons.  $\sigma_i^z = c_{i\uparrow}^{\dagger} c_{i\uparrow} - c_{i\downarrow}^{\dagger} c_{i\downarrow}$  is the z component of the itinerant electron spin,  $S_i = \pm 1$  denotes the localized Ising spin at the ith site, and J is the coupling constant. Hereafter, we take t=1 as the unit of energy, the lattice constant a=1, and the Boltzmann constant  $k_{\rm B}=1$ . As the unit of conductance, we take  $e^2/h$ .

© Springer Japan 2015 H. Ishizuka, Magnetism and Transport Phenomena in Spin-Charge Coupled Systems on Frustrated Lattices, Springer Theses,

#### 5.1.2 Monte Carlo Method

Thermodynamic properties of the model in Eq. (5.1) are studied by the same Monte Carlo (MC) method used in previous chapters; we use numerical diagonalization to calculate the effective action as they are faster for system sizes up to order of hundred sites. The details of the algorithm is elaborated in Sect. 2.2. Using this method, we conducted the calculations up to the system size  $N=3\times N_{\rm s}$  with  $N_{\rm s}=9^2$  where  $N_{\rm s}$  is the number of three-site unit cells. To deal with the freezing of MC sampling, some of the low temperature data were calculated starting from a mixed initial spin configuration of low temperature ordered and high-temperature disordered states [9]. The thermal averages were calculated with typically 4300–80000 MC steps after 1800–18000 MC steps for thermalization. In the MC simulation, we also calculate optical conductivity of itinerant electrons using the standard Kubo formula with scattering rate  $\tau^{-1}=0.01$ .

#### 5.1.3 Variational Calculation

In addition to the MC simulation, we also conducted the variational calculations of the ground state. We compared the ground state energy of the magnetic states found in the MC simulation: they are, ferromagnetic (FM) order, q = 0 ferrimagnetic (FR) and  $\sqrt{3} \times \sqrt{3}$  FR orders. Further details of the algorithm is given in Sect. 2.4.

#### 5.1.4 Observables

To investigate the magnetic behavior of the model, we calculated several parameters to elucidate the information on the spin states, along with the net magnetization  $m = \sqrt{\langle (\sum_i S_i/N)^2 \rangle}$  and spin structure factor

$$S(\mathbf{k}) = \frac{1}{N_{s}} \sum_{i,j \in \alpha} \langle S_{i} S_{j} \rangle \exp\left(i\mathbf{k} \cdot \mathbf{r}_{ij}\right), \qquad (5.2)$$

where  $\mathbf{r}_{ij}$  is the vector from *i*th to *j*th site, and the sum is taken for the sites *i*, *j* in the same sublattice  $\alpha$ .

Firstly, to see the local spin correlations in the FM and FR states, we used the probability to find a two-up one-down spin configuration in each triangle,

$$P = \sqrt{\langle (\sum_{\nu} \frac{p_{\nu}}{2N_{\rm s}})^2 \rangle},\tag{5.3}$$

5.1 Model and Method 67

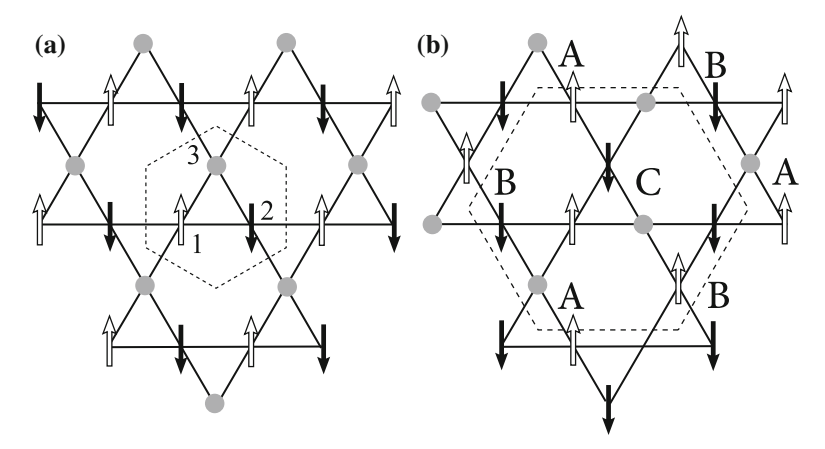


Fig. 5.1 Schematic pictures of the magnetic structures of PD states with  $\mathbf{a} \ \mathbf{q} = \mathbf{0}$  and  $\mathbf{b} \ \sqrt{3} \times \sqrt{3}$  ordering. The *dotted hexagon* in  $\mathbf{a}$  shows the unit cell for the kagome lattice while that in  $\mathbf{b}$  is the magnetic supercell for the  $\sqrt{3} \times \sqrt{3}$  order. The numbers in  $\mathbf{a}$  denote crystallographic sublattice, and A, B, and C in  $\mathbf{b}$  are the magnetic sublattice

where  $p_{\nu} = 1(-1)$  for two-up one-down (one-up two-down) and otherwise  $p_{\nu} = 0$ , and the sum is over all triangles. As we will show later, this parameter acts like an order parameter for the loop-liquid (LL) state, which is a thermally-induced phase with fractional magnetic moment.

In addition to the LL state, we show that this model also exhibit a  $\sqrt{3} \times \sqrt{3}$  partial disorder (PD) state and the Kosterlitz-Thouless (KT) like state similar to that of triangular lattice case discussed in Chap. 3 (Fig. 5.1). In this chapter, we also use the pseudo-spin [3, 15] to study these phases. The pseudo-spin on each unit cell is defined by,

$$\tilde{\mathbf{S}}_{m} = \begin{pmatrix} \frac{2}{\sqrt{6}} - \frac{1}{\sqrt{6}} - \frac{1}{\sqrt{6}} \\ 0 & \frac{1}{\sqrt{2}} - \frac{1}{\sqrt{2}} \\ \frac{1}{\sqrt{3}} & \frac{1}{\sqrt{3}} & \frac{1}{\sqrt{3}} \end{pmatrix} \begin{pmatrix} S_{m}^{1} \\ S_{m}^{2} \\ S_{m}^{3} \end{pmatrix}, \tag{5.4}$$

where  $S_m^{\nu}$  is the Ising spin on the  $\nu$ th site in the mth unit cell (Fig. 5.1a). We calculate the sublattice pseudo-spin moment

$$\mathbf{M}^{\alpha} = \frac{3}{N} \sum_{m \in \alpha} \tilde{\mathbf{S}}_m,\tag{5.5}$$

where  $\alpha = A, B, C$  denotes three sublattices for the pseudo-spins (Fig. 5.1b). To determine the partially disordered state, we also used the azimuth parameter defined by

$$\psi^{\alpha} = (\tilde{M}_{xy}^{\alpha})^3 \cos 6\phi_{\mathbf{M}^{\alpha}},\tag{5.6}$$

where  $\phi_{\mathbf{M}^{\alpha}}$  is the azimuth of  $\mathbf{M}^{\alpha}$  in the xy plane, and  $\tilde{M}_{xy}^{\alpha} = 3(M_{xy}^{\alpha})^2/8$   $[M_{xy}^{\alpha} = \{(M_{x}^{\alpha})^2 + (M_{y}^{\alpha})^2\}^{1/2}]$  (Ref. [15]). The parameter  $\psi^{\alpha}$  takes a negative value and  $\psi^{\alpha} \to -27/64$  for the ideal PD ordering, while it becomes positive and  $\psi^{\alpha} \to 1$  for the ferrimagnetic ordering;  $\psi^{\alpha} = 0$  for both the paramagnetic and the KT-like phases in the thermodynamic limit  $N \to \infty$ .

For both  $\mathbf{q} = \mathbf{0}$  and  $\sqrt{3} \times \sqrt{3}$  PD states shown in Fig. 5.1,  $M_{xy}^{\alpha}$ ,  $|M_{z}^{\alpha}|$ , and  $\psi^{\alpha}$  are independent of  $\alpha$ . To distinguish these two states, we also calculate the net pseudo-spin moment

$$\mathbf{M} = \frac{1}{N} \sum_{m} \tilde{\mathbf{S}}_{m} = \frac{1}{3} \sum_{\alpha} \mathbf{M}^{\alpha}, \tag{5.7}$$

and corresponding  $M_{xy}$ ,  $|M_z|$ , and  $\psi$ . In addition, to detect the phase transitions, we compute the susceptibilities for the pseudo-spin moments by fluctuation formula

$$\chi_O = \frac{N}{T} \left( \langle O^2 \rangle - \langle O \rangle^2 \right),\tag{5.8}$$

where O is a physical quantity renormalized by the number of sites. In the following calculations, we found that all the quantities were independent of  $\alpha$ . Hence, we showed the averaged values over  $\alpha$ ,  $O' = \sum_{\alpha} O^{\alpha}/3$  ( $O^{\alpha} = M_{xy}^{\alpha}$ ,  $|M_{z}^{\alpha}|$ ,  $|\Psi^{\alpha}|$ ).

# 5.2 Loop-Liquid State

# 5.2.1 Phase Diagram

We start by the phase diagram obtained by the MC simulation. Figure 5.2 shows the phase diagram obtained by the MC simulation at J=6 while varying electron density  $n=\sum_{i\sigma}\langle c_{i\sigma}^{\dagger}c_{i\sigma}\rangle/2N$ . As lowering temperature, the system exhibits a phase transition to a state with finite net magnetization. Temperature dependence of m are shown in Fig. 5.3a. In the low density region for  $n \leq 0.28$ , m approaches its saturated value 1 in the low-temperature limit, namely, the system exhibits a fully-polarized FM order. This phase is connected to the FM phase in the the large J region, which is induced by the double-exchange mechanism [1, 17].

While increasing n, the low-temperature value of m decreases from 1 and continuously becomes smaller as n becomes larger, as shown in Figs. 5.3a, b. On the contrary, the local correlation parameter P increases continuously from zero (Fig. 5.3b). A characteristic feature here is that the spin structure factor  $S(\mathbf{k})$  for the same sublattice remains featureless except for the peak at  $\mathbf{k} = \mathbf{0}$ , as shown in Fig. 5.5a. We call this region with the reduced m the partially ferromagnetic (PFM) phase. One point to be noted is that this phase cannot be a ground state of the current model. Hence, at the lowest temperature, the PFM phase is expected to be taken over by another phase.

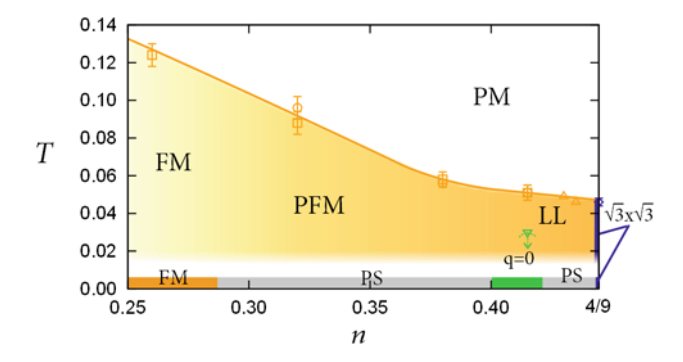
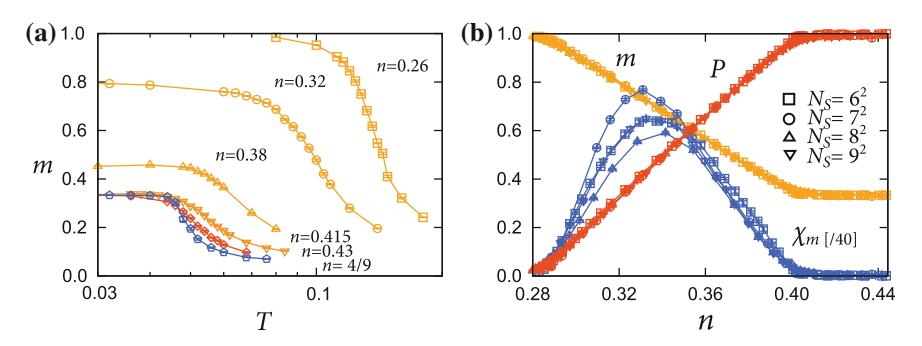


Fig. 5.2 Phase diagram of the model in Eq. (5.1) at J=6. The symbols shows the critical temperatures  $T_c$  for magnetic states: ferromagnetic (FM), partially ferromagnetic (PFM), loop liquid (LL), q=0 ferrimagnetic (q=0), and  $\sqrt{3}\times\sqrt{3}$  ferrimagnetic ( $\sqrt{3}\times\sqrt{3}$ ) states. The upper limit for  $T_c$  for q=0 state q=0. 415 is shown by the downward triangle, which is given by the temperature we reached with  $N_s=8^2$  calculations. The curve connecting the symbols is a guide for the eyes. The strip at the bottom is the ground state phase diagram obtained by the variational calculation. PS is the phase separation between the neighboring two phases



**Fig. 5.3** a MC results for the temperature dependences of m at different n. The data at n=4/9 are calculated for  $N_s=9^2$ , while the others for  $N_s=8^2$ . **b** n dependences of m,  $\chi_m$ , and P at T=0.03 for  $N_s=6^2$ ,  $7^2$ ,  $8^2$ , and  $9^2$ 

In this case, it is likely to be a phase separation between FM and q=0 FR states we found in the variational calculation (see the bottom strip in Fig. 5.2). However, in the MC simulation, we could not determine this instability. Presumably, the phase separation takes place in very low temperature below our calculation.

In the region of  $0.4 \lesssim n < 4/9$ , the low-temperature value of m becomes almost independent of n, and saturates to a fractional value m = 1/3, as shown in Fig. 5.3a. In this region, most of the triangles on the kagome lattice are in two-up one-down spin configurations, namely,  $P \simeq 1$  (Fig. 5.3b). As shown in Fig. 5.5b,  $S(\mathbf{k})$  does not show any sharp peak except for the one at  $\mathbf{k} = \mathbf{0}$ , indicating that this state has no superstructure. Hence, this FR state is a peculiar magnetic state subject to the two-up one-down local constraint, in a similar sense to the two-in two-out state in spin ice [5, 10]. The spin state is composed of the emergent degrees of freedom, self-avoiding

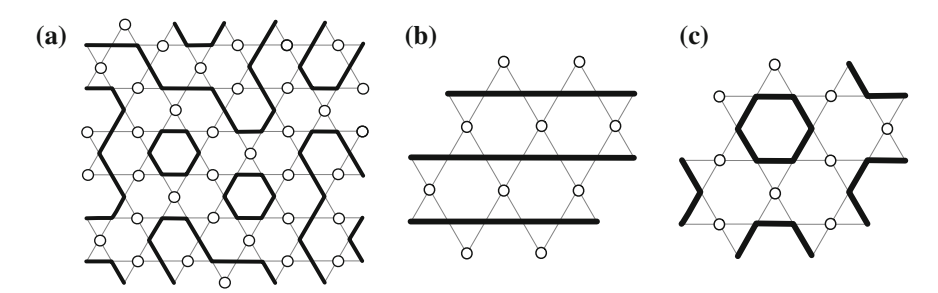


**Fig. 5.4** The schematic pictures of the magnetic states for **a** loop-liquid, **b** q=0, and  $\mathbf{c}\sqrt{3}\times\sqrt{3}$  ferrimagnetic states. The *bold lines* denote the loops connecting up-spin sites and the *dots* show down-spin sites

up-spin loops and isolated down-spins, as schematically shown in Fig. 5.4a (the bold lines in the schematic picture connect up-spin sites while the dots represent down spins). Hence, we call this state the LL state.<sup>1</sup>

An interesting observation here is that the change between the FM, PFM, and LL states is smooth and there is no sign of phase transition. Both m and P changes continuously without showing any singularity, and the magnetic susceptibility  $\chi_m$  shows only a broad hump, as shown in Fig. 5.3b. This indicates that the change from FM to LL is a crossover and not a phase transition. Such behavior is understood from the symmetry point of view. In the LL state, though it possesses a fractional magnetic moment, the system still remains disordered and preserves all the symmetries of the lattice; the situation is unchanged from the FM and PFM states. As a consequence, these phases are smoothly connected by the crossover.

As further decreasing temperature or further increasing n, the LL state exhibits phase transitions with showing a magnetic long-range order (LRO). In our MC simulation, we identify two different transitions; one is the transition to the state with q=0 LRO of the two-up one-down spin configurations (Fig. 5.4b), and the other to the state with  $\sqrt{3} \times \sqrt{3}$  LRO (Fig. 5.4c). The former is observed while decreasing temperature at  $n \sim 0.415$ , and the latter is found by increasing n to a commensurate filling n=4/9.  $S(\mathbf{k})$  for the latter state is shown in Fig. 5.5c. In the corresponding density regions, the two phases are obtained in the variational calculation for the ground state, as shown in Fig. 5.2. These two LRO states are viewed as crystal phases of the emergent loops in the two extreme cases; the former is a periodic array of one-dimensional chains, while the latter the shortest six-site hexagons. Interestingly, the peculiar LL state extends in the density region between these two crystal phases.

<sup>&</sup>lt;sup>1</sup>In general, the algebraic spin correlation may induce a characteristic diffusive structure in the magnetic structure factor, such as the pinch points in the case of spin ice. Indeed, we see a broad hump around  $\mathbf{q} = (\pm 2\pi/3, \mp 2\pi/3)$ , which might be the sign of such structure. However, we need larger systems sizes to precisely determine such a structure.

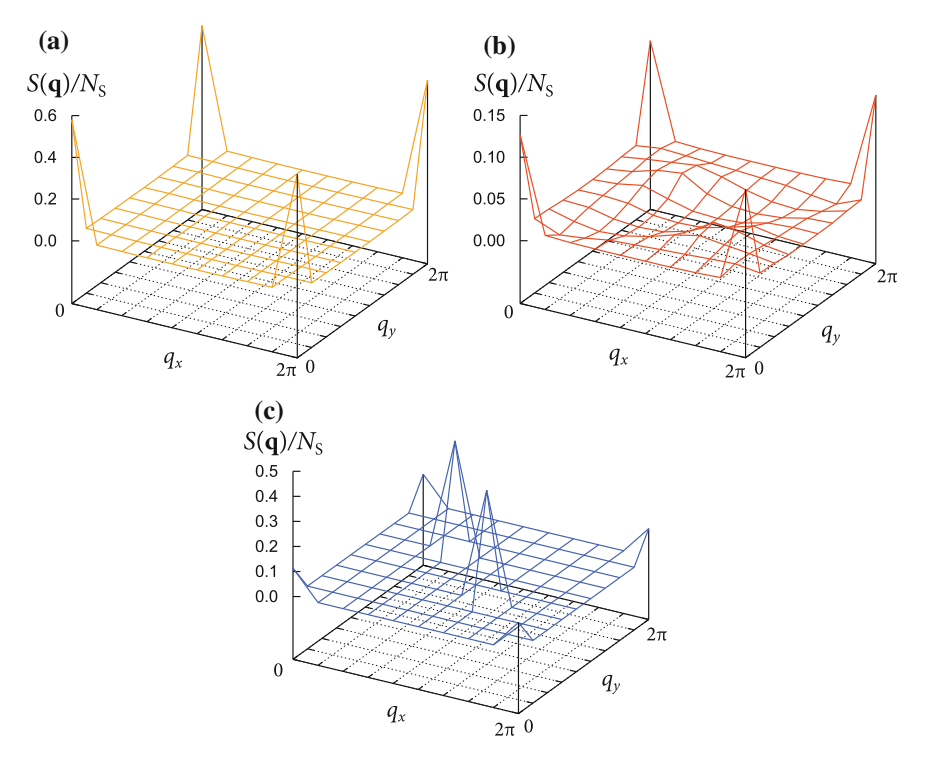


**Fig. 5.5** The MC results of  $S(\mathbf{k})/N_s$  are shown for  $\mathbf{a}$  n=0.325,  $\mathbf{b}$  n=0.42, and  $\mathbf{c}$  n=4/9 at T=0.03 and  $N_s=9^2$ 

# 5.2.2 Loop Liquid and Its Crystalization

Let us closely look at the MC results in the LL region. Figure 5.6 shows the temperature dependence at n=0.415 calculated by MC simulation. Figure 5.6a shows the result of net magnetization m and its susceptibility  $\chi_m$ . m increases with decreasing temperature and shows saturation to 1/3, associated with a divergent peak of  $\chi_m$  at  $T\sim 0.05$ . At the same temperature, P shows saturation to 1 and its susceptibility  $\chi_P$  shows a peak, as shown in Fig. 5.6b. This indicates most of the triangles become two-up one-down below  $T\sim 0.05$ . To determine the order of transition and the transition temperature of this phase transition, we calculated Binder parameter [2] for m and P,  $g_m$  and  $g_P$ , respectively. They are shown in Fig. 5.6d. The two Binder parameters show a monotonic increase with decreasing temperature and a crossing, consistently suggesting the transition to be of second order. The critical temperature for the transition is determined from the crossing of the results for different sizes; it is estimated to be  $T_c = 0.051(4)$ . On the other hand, a rapid increase of  $S(\mathbf{k} = \mathbf{0})/N_s$  to 1 is observed in  $N_s = 4^2$  and  $6^2$ , as shown in Fig. 5.6c. However, the onset temperature decreases for larger  $N_s$ ; they also show strong finite size effects

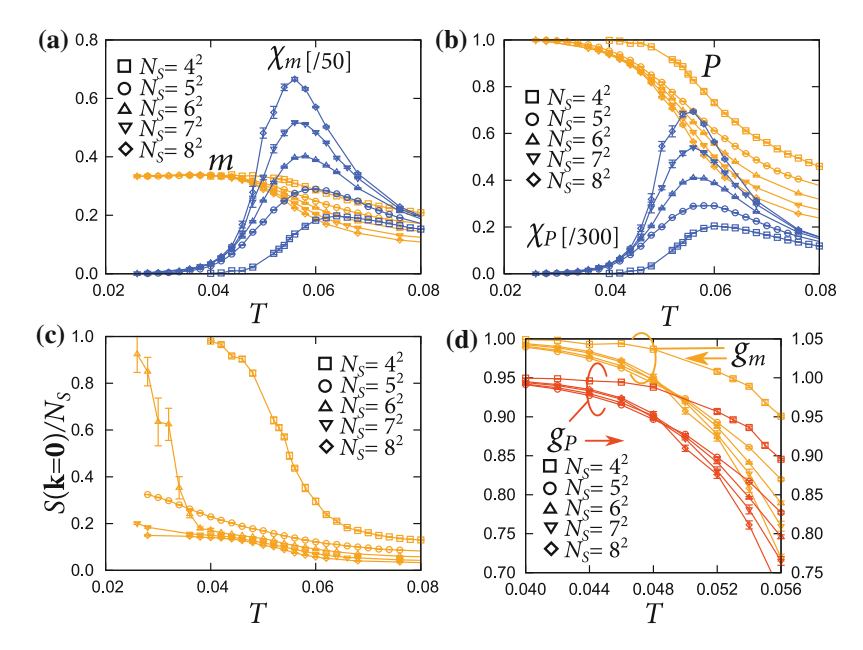


**Fig. 5.6** MC results for **a** m and  $\chi_m$ , **b** P and  $\chi_P$ , **c**  $S(\mathbf{k} = \mathbf{0})/N_s$ , and **d**  $g_m$  and  $g_P$  for  $N_s = 4^2$ ,  $5^2$ ,  $6^2$ ,  $7^2$ , and  $8^2$  and at n = 0.415

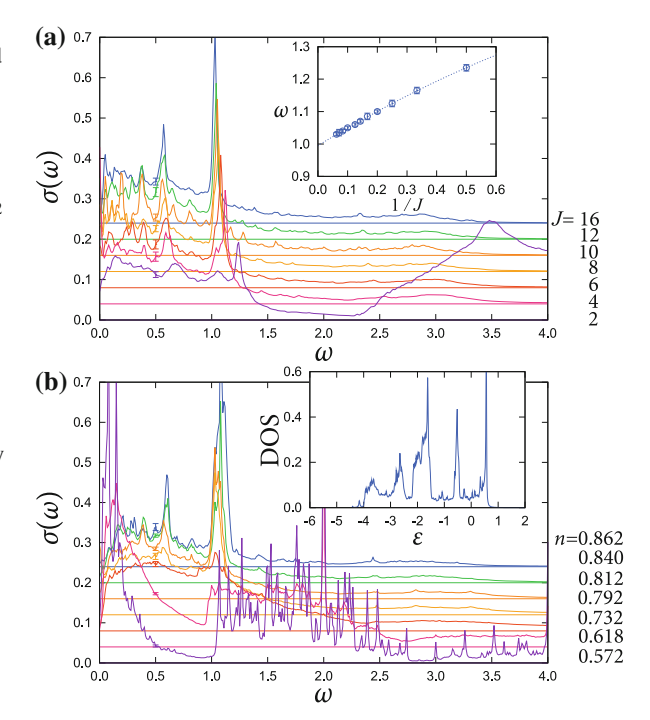
with different behavior for even and odd  $N_{\rm s}$ . This implies a phase transition to the q=0 ordered state takes place at a lower temperature, at least lower than the onset temperature for  $N_{\rm s}=6^2$ , 0.028. This is consistent with the ground state obtained by the variational calculation, as shown in Fig. 5.2a. Although the precise estimate of the critical temperature is difficult within the present calculation, these results indicate that successive phase transitions from PM to LL and LL to q=0 FR state take place at n=0.415. The former corresponds to the formation of loops, and the latter their crystallization.

#### 5.2.3 Resonant Peak in the Electronic State

In the last, we discuss the electronic and transport properties of the itinerant electrons in the LL state. The results of optical conductivity  $\sigma(\omega)$  is shown in Fig. 5.7.

We here study the optical conductivity of LL state using two different approaches. First, to extract the effect of characteristic spin correlations in the LL state, we calculate  $\sigma(\omega)$  by taking simple average over different spin patterns in the ideal LL manifold, i.e., all the triangles satisfy the two-up one-down local constraint. Figure 5.7a is the result of  $\sigma(\omega)$  calculated by taking simple average over 24 different spin configurations, generated randomly. The optical conductivity was calculated at

Fig. 5.7 Optical conductivity  $\sigma(\omega)$  calculated by a simple average over LL configurations at n = 0.422for a  $2^2$  supercell of  $N = 3 \times 12^2$  sites, and **b** MC simulation at J = 6 for a  $4^2$  supercell of  $N = 3 \times 6^2$ sites at T = 0.04. J(n) on the right side of a (b) show Kondo coupling (electron density) for each data. The typical error bars are shown at  $\omega = 0.5$ . The inset in a shows the peak position of  $\sigma(\omega)$  at  $\omega \sim 1$  with the dotted line showing fitting by  $\omega = 0.995 + 0.558$  $J = 0.155/J^2$ . The inset in **b** is DOS at n = 0.431 and T = 0.04



n=0.422 for various J. An interesting feature of the result is the sharp peak at  $\omega=\omega_p\sim 1.0$ –1.2, which shifts to lower  $\omega$  for larger J.

This comes from the transition process between two localized states in the six-site loops. In the limit of  $J \to \infty$ , electrons are confined in the loops or at isolated sites [7]; the contribution to  $\sigma(\omega)$  comes only from the transition process between the electronic states in the same loop. Hence, sharp peaks appear in  $\sigma(\omega)$  corresponding to the discrete energy levels in the finite length loops. In the current kagome case, the most dominant loops are the shortest ones with the length of six sites. In the six-site loops, the energy difference between the unoccupied and occupied levels at this filling (the highest and second highest levels) is 1. Hence, we expect a sharp peak at  $\omega_p = 1$  in the limit of  $J \to \infty$ . For large but finite J, the second order perturbation in terms of the hopping between up and down spin sites shifts the second highest eigenenergy to a lower energy. On the other hand, this perturbation process does not affect the highest eigenenergy state. Hence, it is expected that the peak shifts to a higher  $\omega$  as decreasing J; the asymptotic behavior at  $J \to \infty$  is expected to be  $\omega_p = 1 + \mathcal{O}(1/J)$ . This is confirmed by the fitting shown in the inset of Fig. 5.7a.

Interestingly, the peak persists in the weak J region where the exchange splitting 2J is comparable or smaller than the bandwidth, 6t, where the above perturbative argument is expected to be no longer valid. In a recent study on a metal-insulator transition caused by correlated potentials, a LL-type local correlation induces a metal-insulator transition at a considerably smaller potential than the bandwidth

by confining the electrons in the loops [6]. The persistent existence of resonant peak is likely to be a consequence of this confinement.

Emergence of the characteristic peak is also observed in the thermodynamic average obtained by the MC simulation. Figure 5.7b shows the MC result of  $\sigma(\omega)$  while varying n at T=0.04 and J=6. With increasing n from the FM region, the peak at  $\omega \sim 1$  develops in the LL state for  $n \gtrsim 0.4$ . The inset in Fig. 5.7b shows the density of states (DOS) for itinerant electrons (lower half of two split bands) at n=0.431. The result clearly shows the presence of two sharp peaks below and above the Fermi level set at  $\varepsilon=0$ ; the energy difference is about 1.1, which well corresponds to the peak in  $\sigma(\omega)$  in the main panel of Fig. 5.7b.

#### 5.3 Partial Disorder

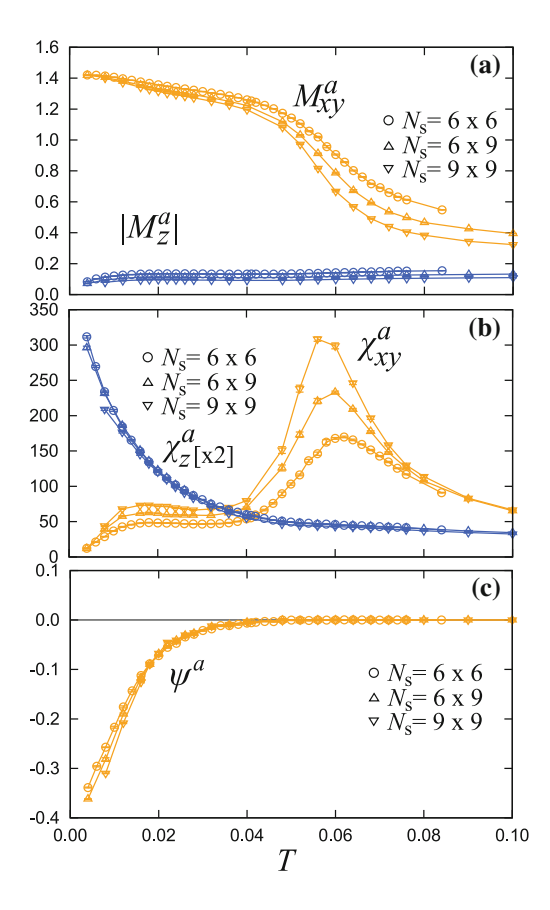
We next focus on the weak J region of the model in Eq. (5.1). We show that, in the weak J region at n = 1/3, the system exhibits the PD and the KT-like state.

Figure 5.8 shows the results of the MC calculation at n=1/3 and J=2. As shown in Fig. 5.8a,  $M_{xy}^{\alpha}$  monotonically increases with decreasing temperature and shows a rapid increase at  $T\sim0.06$ . In addition, it exhibits a small shoulder at  $T\sim0.015$  before approaching the value at the lowest temperature. The two anomalies are more clearly observed in the corresponding susceptibility  $\chi_{xy}^{\alpha}$  plotted in Fig. 5.8b;  $\chi_{xy}^{\alpha}$  shows a divergent peak at  $T\sim0.06$  and a hump structure at  $T\sim0.015$ . The results imply two successive transitions takes place with decreasing temperature. As it will be discussed later, the anomaly at higher temperature is a transition to KT-like state and the lower temperature one is PD. The transition temperature are estimated to be  $T_{\rm KT}=0.057(3)$  by extrapolating the peak temperature of  $\chi_{xy}^{\alpha}$ . On the other hand, the onset of PD state,  $T_c^{\rm PD}$ , is estimated as  $T_c^{\rm PD}=0.030(2)$  from the azimuth parameter  $\psi$ , by temperature at which the size-extrapolated  $\psi$  deviates from zero.

First, we consider the temperature region  $T < T_c^{PD}$ . At the lowest temperature of our calculation,  $M_{xy}^{\alpha}$  approaches  $\sqrt{2}$  while  $|M_z^{\alpha}|$  is essentially zero in the thermodynamic limit, as shown in Fig. 5.8a. In addition,  $\psi^{\alpha}$  shows a sharp decrease in this region, from  $\psi^{\alpha} = 0$  to  $\sim -0.4$ , as shown in Fig. 5.8c. The nonzero  $\psi^{\alpha}$  indicates a spontaneous breaking of six-fold rotational symmetry of  $\mathbf{M}^{\alpha}$ ; specifically, the negative value approaching -27/64 suggests that the system exhibits PD state. Correspondingly, as shown in Fig. 5.8b,  $\chi_z^{\alpha}$  shows a monotonic increase with decreasing temperature, which is ascribed to the presence of paramagnetic spins in the PD state. In contrast to  $M_{xy}^{\alpha}$ , no increase in the net moments,  $M_{xy}$  or  $M_z$ , is seen in the entire range of calculation;  $\psi$  is also zero. We also found that the spin structure factor exhibits a peak corresponding to the  $\sqrt{3} \times \sqrt{3}$  order. Hence, we conclude that the system exhibits the PD state with period  $\sqrt{3} \times \sqrt{3}$  for  $T < T_c^{PD}$ .

5.3 Partial Disorder 75

**Fig. 5.8** MC results for a  $M_{xy}^{\alpha}$  and  $|M_z^{\alpha}|$ , b  $\chi_{xy}^{\alpha}$  and  $\chi_{z}^{\alpha}$ , and c  $\psi^{\alpha}$ . Results shown are the average over all the sublattices  $\alpha = A$ , B, C (See Fig. 5.1b). The data are for J = 2 with system sizes  $N = 6 \times 6$ ,  $6 \times 9$ , and  $9 \times 9$  at n = 1/3



Next, we examine the intermediate temperature region  $T_c^{\text{PD}} < T < T_{\text{KT}}$ . As shown in Fig. 5.8b,  $\chi_{xy}^{\alpha}$  shows a divergent peak at  $T_{\text{KT}}$  corresponding to a rapid rise of  $M_{xy}^{\alpha}$  in Fig. 5.8a, which is a clear indication of a phase transition.  $M_{xy}^{\alpha}$ , however, exhibits a considerable finite-size effect in this temperature region. On the other hand,  $|M_z^{\alpha}|$  and  $\psi^{\alpha}$  shows almost no change. In particular,  $\psi^{\alpha}$  is extrapolated to zero within statistical errors in the limit of  $N \to \infty$ , indicating that the intermediate region shows no rotational symmetry breaking with respect to  $\mathbf{M}^{\alpha}$ . Similar behavior was observed in the KT phase with quasi-long-range order in the Ising antiferromagnets on triangular and kagome lattices [3, 4, 12–14] and in the Kondo lattice model on a triangular lattice (Chap. 3). Hence, we conclude that the intermediate phase for  $T_c^{\text{PD}} < T < T_{\text{KT}}$  is of a KT-like phase.

Consequently, our MC data indicate that the system exhibits two successive phase transitions in the calculated temperature range: one is from a high-temperature paramagnetic phase to an intermediate KT-like phase, and the other is from the KT-like phase to a low-temperature PD state with period  $\sqrt{3} \times \sqrt{3}$ . One point to be addressed here is an anticipated phase transition from the PD state to the true ground state. The

PD state retains residual entropy of  $\sim \frac{1}{3} \log 2$  associated with the 1/3 paramagnetic moments. Hence, the PD state is unlikely to be the ground state of the present model because the degeneracy will be lifted by the long-range Ruderman-Kittel-Kasuya-Yosida (RKKY) interactions induced by the spin-charge coupling (Sect. 1.2.1) [8, 11, 16]. However, in our MC simulation at n=1/3, there is no indication of a further phase transition from the PD state down to  $T \simeq 10^{-3} t$ . This implies that the energy scale of the relevant RKKY interaction is extremely small and that the true ground state is nearly degenerate with other spin configurations in the PD state. A similar feature was also discussed in an Ising spin Kondo lattice model on a triangular lattice in Chap. 3.

Finally, let us compare the present results with those for the model on a triangular lattice discussed in Chap. 3. In the kagome lattice case, the transition temperature to the PD state,  $T_c^{\rm PD}=0.030(2)$ , is an order of magnitude smaller than that in the triangular lattice case,  $T_c^{\rm PD}=0.130(4)$  (see Sect. 3.3.2 for further details). This is presumably because of the stronger frustration in the kagome lattice case. Namely, the antiferromagnetic order develops on the honeycomb network in the case of a PD state on the triangular lattice, whereas it appears on the disconnected hexagons in the kagome lattice case, as shown in Fig. 5.8b; the former can be accommodated by NN interactions, but the latter needs further-neighbor interactions. Hence, the difference of  $T_c^{\rm PD}$  can be understood because the RKKY interaction becomes weaker for further neighbors in general. In the kagome lattice case, instead, the KT-like phase appears over a wide temperature range above the PD phase whereas a direct transition from the paramagnetic to PD phase is observed for the triangular lattice model at 1/3-filling. This might also be ascribed to the difference in frustration; a higher entropy due to the stronger frustration may contribute to the prevalence of the KT-like phase.

# 5.4 Summary

In this chapter, we studied an Ising-spin Kondo lattice model on a kagome lattice focusing on the emergent magnetic states and their electronic properties. In the region with J comparable to the bandwidth, we presented that the loop-liquid state emerges in the finite temperature region, in addition to ferromagnetic, q=0 ferrimagnetic, and  $\sqrt{3} \times \sqrt{3}$  ferrimagnetic states. The loop liquid is a Coulombic ferrimagnetic state, characterized by the emergent up-spin loops originating from the two-up one-down local spin configurations. The phase diagram is understood in terms of the emergent loops as crystallization and cohesion of the dense liquid of the loops. We also showed that the loop-liquid formation is observed in characteristic peaks in the optical conductivity.

On the other hand, in the weak J region at n=1/3, we found two successive transitions: one from a high-temperature paramagnetic phase to an intermediate-temperature Kosterlitz-Thouless-like phase, and the other to a low-temperature  $\sqrt{3} \times \sqrt{3}$  partially-disordered state. The two transitions are clearly elucidated by an unbiased Monte Carlo simulation, using the pseudo-spin moments, the corresponding

5.4 Summary 77

susceptibilities, and the azimuth parameter. A comparison between the present results and those for a triangular lattice implies that the partial disorder is stabilized in a wide class of two-dimensional Kondo lattice models under frustration.

# References

- 1. P.W. Anderson, H. Hasegawa, Phys. Rev. **100**, 675 (1955)
- 2. K. Binder, Z. Phys. B 43, 119 (1981)
- 3. S. Fujiki, K. Shutoh, S. Katsura, J. Phys. Soc. Jpn. **53**, 1371 (1984)
- 4. S. Fujiki, K. Shutoh, S. Inawashiro, Y. Abe, S. Katsura, J. Phys. Soc. Jpn. 55, 3326 (1986)
- M.J. Harris, S.T. Bramwell, D.F. McMorrow, T. Zeiske, K.W. Godfrey, Phys. Rev. Lett. 79, 2554 (1997)
- 6. H. Ishizuka, M. Udagawa, Y. Motome, Phys. Rev. B 83, 125101 (2011)
- 7. L.D.C. Jaubert, S. Piatecki, M. Haque, R. Moessner, Phys. Rev. B 85, 054425 (2012)
- 8. T. Kasuya, Prog. Theor. Phys. 16, 45 (1956)
- 9. Y. Ozeki, K. Kasono, N. Ito, S. Miyashita, Phys. A 321, 271 (2003)
- A.P. Ramirez, A. Hayashi, R.J. Cava, R. Siddharthan, B.S. Shastry, Nature (London) 399, 333 (1999)
- 11. M.A. Ruderman, C. Kittel, Phys. Rev. 96, 99 (1954)
- 12. T. Takagi, M. Mekata, J. Phys. Soc. Jpn. **62**, 3943 (1993)
- 13. T. Takagi, M. Mekata, J. Phys. Soc. Jpn. **64**, 4609 (1995)
- 14. H. Takayama, K. Matsumoto, H. Kawahara, K. Wada, J. Phys. Soc. Jpn. 52, 2888 (1983)
- 15. N. Todoroki, S. Miyashita, J. Phys. Soc. Jpn. 73, 412 (2004)
- 16. K. Yosida, Phys. Rev. 106, 893 (1957)
- 17. C. Zener, Phys. Rev. 82, 403 (1951)

# Chapter 6

# **Anomalous Hall Insulator in Kagome Ice**

Abstract In this chapter, we consider double-exchange model with Ising localized moment on a kagome lattice. We consider Ising anisotropy of the localized moments to be that of (111) kagome plane of pyrochlore spin ice. We find that the local-spin correlation developed in the kagome plane, kagome-ice state, opens a charge gap without magnetic ordering. The insulating phase is a quantum anomalous Hall insulator. By Monte Carlo simulation, we elucidate the anomalous Hall insulating region in the phase diagram with temperature and magnetic field. We also discuss the stability of the charge gap in an anisotropic pyrochlore lattice composed of the kagome layers weakly coupled by the interlayer triangular sites.

#### 6.1 Model and Method

Here, we introduce the model and methods we used in this chapter. In Sect. 6.1.1, we introduce the model in details. Subsequent sections are devoted to the description of method we used; details on the numerical diagonalization and Monte Carlo (MC) simulation are given in Sects. 6.1.2 and 6.1.3, respectively.

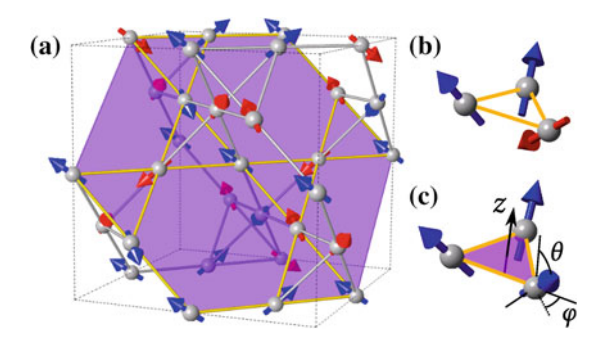
# 6.1.1 Kagome Ice Model

In this chapter, we consider a single-band double-exchange (DE) model [1, 15] with the spin-ice type Ising spins on a kagome lattice, which corresponds to the  $\langle 111 \rangle$  plane of a pyrochlore lattice (see Fig. 6.1a).

$$H = -\sum_{\langle i,j\rangle} (t_{ij}c_i^{\dagger}c_j + \text{H.c.}) - \sum_i h_z \cos \theta_i.$$
 (6.1)

Here,  $c_i$  ( $c_i^{\dagger}$ ) is the annihilation (creation) operator of an itinerant electron at ith site. The spin index of electron is dropped as the spin is aligned parallel to the localized moment  $\mathbf{S}_i$  at each site. The anisotropy axis of the localized

Fig. 6.1 a Schematic picture of spin ice on a pyrochlore lattice. The shaded plane indicates a (111) kagome plane. Schematic pictures of **b** one-in two-out and **c** all-out type spin configuration



moments depend on the sublattice; they are given by  $\mathbf{S}_i = (S_i^x, S_i^y, S_i^z) = S(\sin\theta_i\cos\varphi_i, \sin\theta_i\sin\varphi_i, \cos\theta_i)$ , where  $(\theta_i, \varphi_i) = (\arccos(\frac{1}{3}), \frac{2\pi}{3}n_{\rm S} + \frac{\pi}{2})$ ,  $(\arccos(-\frac{1}{3}), \frac{2\pi}{3}n_{\rm S} - \frac{\pi}{2})$  for the sublattice  $n_{\rm S} = 1, 2, 3$  and S = 1 (see Fig. 6.1c). This anisotropy axes correspond to the line connecting center of the two tetrahedra the site belongs to (Fig. 6.1a).

The sum  $\langle i, j \rangle$  in the first term of Eq. (6.1) is taken over nearest-neighbor (NN) sites on the kagome lattice, and the effective transfer integral  $t_{ij}$  depends on the relative angle of neighboring Ising spins; they are given by

$$t_{ij} = t \left( \cos \frac{\theta_i}{2} \cos \frac{\theta_j}{2} + \sin \frac{\theta_i}{2} \sin \frac{\theta_j}{2} e^{-i(\varphi_i - \varphi_j)} \right), \tag{6.2}$$

where t is the transfer integral between NN sites. In Eq.(6.1), for simplicity, the effect of external magnetic field is taken into account by the Zeeman term only for the localized Ising moments. Hereafter, we set the unit of energy t=1, the length of Bravais lattice vector a=1, and the Boltzmann constant  $k_{\rm B}=1$ . For conductance, the unit is taken as  $e^2/h=1$ , where e is the elementary charge and h is the Planck constant.

In DE models, the spin-charge coupling induces an effective ferromagnetic interaction between the localized spins at general filling as discussed in Sect. 1.2.2 [1, 15]. In this model, the ferromagnetic interaction for NN sites gives rise to macroscopic degeneracy in the ground state. In addition to the effective NN interactions, the spin-charge coupling also gives rise to further-neighbor interactions, which generally lifts the degeneracy in the ground state and select a magnetic order as the ground state. However, as the further-neighbor interactions are usually much weaker than the NN one, a cooperative paramagnetic state with strong local correlations of two-in one-out or one-in two-out is expected to emerge in the intermediate temperature (T) region between a high-T paramagnetic state and the low-T ordered phase. The main focus of this chapter is to study the electronic and transport properties in the cooperative paramagnetic state that evolve in applied magnetic field.

6.1 Model and Method 81

# 6.1.2 Numerical Diagonalization

In the following sections, we study the effect of spin correlation to the electronic states of itinerant electrons by taking a simple average (arithmetic mean) over different configurations of spins. Instead of the magnetic field  $h_z$ , we control the net magnetization along the z direction per triangle,

$$m_z = \frac{1}{N_s} \sum_i \cos \theta_i, \tag{6.3}$$

where  $N_s = N/3$  is the number of the unit cells and N is the number of sites.

The average is taken over different spin configurations with a fixed ratio of different types of triangles. For  $0 \le m_z \le 1/3$ , we consider the manifold in which all the triangles are of two-in one-out or one-in two-out type; their ratio is controlled so as to realize the given value of  $m_z$ . At  $m_z = 1/3$ , all the upward (downward) triangles are in the two-in one-out (one-in two-out) configuration, which is the kagome ice. For  $m_z > 1/3$ , we introduce all-in upward and all-out downward triangles. Eventually, at the saturation to  $m_z = 1$ , the system shows a long-range order of alternating all-in and all-out triangles. For all the cases in  $m_z < 1$ , we generate different spin configurations using a loop update method [7].

The conductivity is calculated by using the Kubo formula. The calculations were done on  $4^2$  superlattices of  $N=3\times18^2$  sites and  $T=10^{-5}$  by averaging over 32 realizations of different spin configurations. Conductivities are calculated with assuming a small inelastic scattering rate  $\tau^{-1}=(3\times18^2\times4^2)^{-1}$ .

#### 6.1.3 Monte Carlo Simulation

In addition to the numerical diagonalization method, we also conducted a MC simulation to investigate magnetic and transport properties in the low temperature region. We used the algorithm described in Sect. 2.2 using the single-spin flip update and global loop update algorithm for the localized spins [11]. The calculations were conducted up to  $N = 3 \times 10^2$  with typically 20,000 MC measurements after 6000 steps of thermalization.

In the Monte Carlo simulation, we calculated difference of two-in one-out and one-in two-out triangles

$$\rho = \sqrt{\langle (\rho^+ - \rho^-)^2 \rangle} \tag{6.4}$$

and the scalar spin chirality

$$\kappa = \frac{1}{2N_{\rm s}} \sum_{(i, i, k)} \langle \mathbf{S}_i \cdot \mathbf{S}_j \times \mathbf{S}_k \rangle \tag{6.5}$$

to identify the kagome-ice state, in addition to  $m_z$  defined in Sect. 6.1.2. Here,  $\rho^+$  is the probability of an upward (downward) triangle to be two-in one-out (one-in two-out) and the  $\rho^-$  is probability for one-in two-out (two-out one-in). In Eq. (6.5), the sum is taken over all the triangles in the kagome lattice. The susceptibilities for  $m_z$  and  $\rho$ ,  $\chi_m$  and  $\chi_\rho$ , were also calculated by

$$\chi_O = \frac{N}{T} \left( \langle O^2 \rangle - \langle O \rangle^2 \right),\tag{6.6}$$

where O is a physical quantity renormalized by the number of sites. Conductivities were calculated by using Kubo formula with taking inelastic scattering factor  $\tau = 0.05$ .

#### **6.2** Exact Diagonalization Study of Electronic States

#### 6.2.1 Density of States

Figure 6.2 shows the electronic density of states (DOS) for different values of  $m_z$ . The solid and open arrows on the spectra indicate the Fermi levels for the electron filling n=1/3 and n=2/3, respectively. Here, electron filling is defined by  $n=\frac{1}{N}\sum_i \langle c_i^{\dagger}c_i \rangle$ .

Figure 6.2a shows the results for  $0 \le m_z \le 1/3$ , where all the triangles are in two-in one-out or one-in two-out configurations. The results indicate that the development of spatial correlations in the kagome ice manifold develops a charge gap at n = 2/3 near  $m_z = 1/3$ , although there is no magnetic long-range order. We also note that a  $\delta$ -function peak appears inside the charge gap. This originates from the localized bound states within the hexagons with all spins in or all spins out. The formation of bound states is a consequence of the quantum phase interference. The details will be discussed in Sect. 6.2.2.

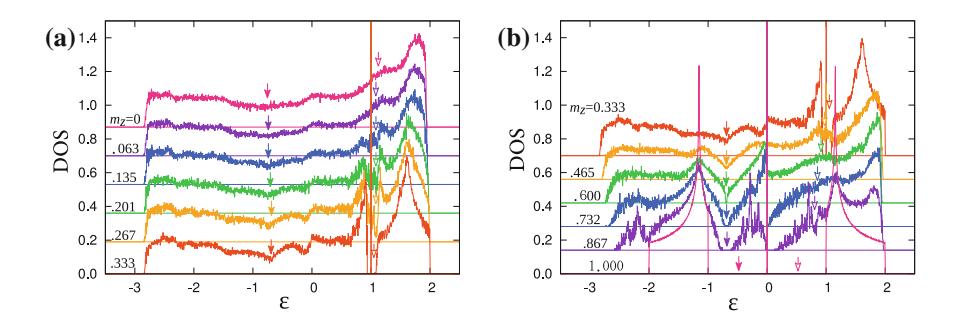


**Fig. 6.2** DOS for different  $m_z$  calculated by the simple average over the kagome ice spin configurations. Solid and open arrows indicate the Fermi levels for n = 1/3 and n = 2/3, respectively. The data for different  $m_z$  are plotted with the offset of 0.14 and 0.19 in **a** and **b**, respectively

Figure 6.2b shows the results for  $1/3 \le m_z \le 1$ , where the all-in upward or all-out downward triangles (magnetic monopoles) are introduced into the kagome ice manifold. At the Fermi level for n=1/3, the introduction of monopoles leads to a dip in the spectra, and opens a full gap for  $m_z \ge 0.7$ . On the other hand, the energy gap at n=2/3 and  $m_z=1/3$  is closed by introducing monopoles. However, for  $m_z \ge 0.7$ , DOS develops a dip again and shows an energy gap at  $m_z \simeq 1$ . In the all-in/all-out ordered state at  $m_z=1$ , DOS has a particle-hole symmetric form with two gaps at n=1/3 and n=2/3 above and below the central flat band [12].

# 6.2.2 In-Gap Localized States

In the results of DOS shown in Fig. 6.2, we found a  $\delta$ -function peak at  $\varepsilon = 1$ , in the energy gap of the kagome ice insulator. We show that this peak comes from the localized electronic state in the six-site loops of the spins pointing inward for the upward triangles (outward for the downward triangles) (see Fig. 6.3). This can be understood by considering a wave function

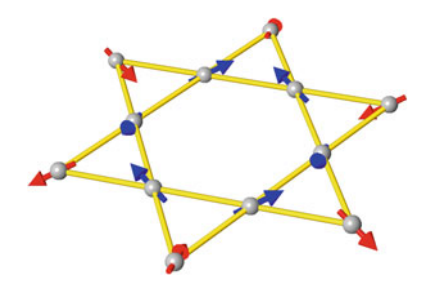
$$|\psi\rangle = \frac{1}{\sqrt{6}} \sum_{n=1}^{6} e^{-i\frac{2\pi}{3}n} c_{i_n}^{\dagger} |0\rangle$$
 (6.7)

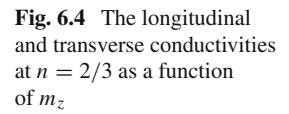
where  $\{i_1, \dots, i_6\}$  is the sites in the hexagon of Fig. 6.3 in clockwise direction. By multiplying the Hamiltonian in Eq. (6.1) to the eigenstate in Eq. (6.7), we can see that Eq. (6.7) is the eigenfunction of Eq. (6.1) with  $\varepsilon = 1$ ; the hopping terms going out of the loop cancel out by the quantum phase interference. Hence, for each six-site loop, there exists one localized electronic state with eigenenergy  $\varepsilon = 1$ , which form the in-gap flat band.

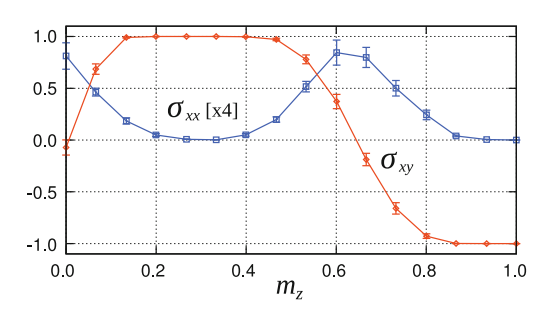
# 6.2.3 Conductivity

To gain further insight into the peculiar changes of DOS in Sect. 6.2.1, we calculated the longitudinal  $(\sigma_{xx})$  and transverse  $(\sigma_{xy})$  conductivities. Figure 6.4 shows the results

**Fig. 6.3** Schematic picture of the six-site loops in the kagome ice state







at n = 2/3. For  $0 \le m_z \le 1/3$ ,  $\sigma_{xx}$  shows monotonic decrease in accordance with the growth of energy gap in DOS. On the other hand,  $\sigma_{xy}$  shows monotonic increase while increasing  $m_z$ , showing a quantized value at  $\sigma_{xy} = 1$  in the gapped state near  $m_z = 1/3$ . In the kagome ice state, we confirmed that all the spin configurations we generated become  $\sigma_{xy} = +1$  within errors of the order of  $10^{-6}$ . Small deviations presumably come from a small T introduced in the calculations.

For  $m_z > 1/3$ ,  $\sigma_{xx}$  increases and shows a hump at  $m_z \sim 2/3$ ; finally it decreases to zero in the all-in/all-out insulator at  $m_z = 1$ . Correspondingly,  $\sigma_{xy}$  decreases from 1 with showing a sign change at  $m_z \sim 2/3$ , and converges to another quantized value  $\sigma_{xy} = -1$  at  $m_z = 1$ .

The non-monotonic change of the Hall conductivity  $\sigma_{xy}$  is explained by the Berry phase mechanism [8, 12, 14]. In a previous study on the kagome DE model with  $\mathbf{q}=0$  all-in all-out magnetic order [12], it was shown that the Hall conductivity depends on the scalar chirality of localized spins in the three-site unit cell,  $\mathbf{S}_i \cdot \mathbf{S}_j \times \mathbf{S}_k$ . A similar mechanism was shown to work through the fluctuations [13] also. Our result of  $\sigma_{xy}$  is understood by considering the scalar chirality; two-in one-out (one-in two-out) upward (downward) triangles bring negative chirality  $-\frac{4}{3\sqrt{3}}$  while magnetic monopoles bring positive chirality  $+\frac{4}{3\sqrt{3}}$  each.

The remarkable point in our results is the quantization of  $\sigma_{xy}$  at +1 in the gapped kagome ice state and its switching to -1 accompanied by the closing and reopening of the energy gap at n=2/3 and associated hump in  $\sigma_{xx}$ . The change in  $\sigma_{xy}$  as well as the hump in  $\sigma_{xx}$  suggests a transition between the kagome ice at  $m_z=1/3$  and all-in/all-out ordered state at  $m_z=1$ . The latter ordered state was shown to be an anomalous Hall insulator (AHI) characterized by the first Chern number C=-1 [12]. On the other hand, the kagome ice at  $m_z=1/3$  is a paramagnetic state with constrained local spin configurations. Hence, the quantization of  $\sigma_{xy}$  as well as the gap opening in DOS is highly nontrivial, suggesting that the cooperative paramagnetic state with kagome-ice correlation is another AHI. The closing and reopening of the energy gap as well as the hump of  $\sigma_{xx}$  is interpreted as a phase transition between topologically different insulators with a transient metallic state in between.

#### **6.3 Monte Carlo Simulation**

The above calculations imply that a similar change between the kagome ice and all-in/all-out ordered state can take place in the model in Eq. (6.1) in applied magnetic field  $h_z$ . To confirm this, in this section, we investigate the thermodynamic behavior of the kagome DE model by a MC simulation, that can take into account the interplay of localized moments and itinerant electrons.

# 6.3.1 Magnetic Properties

Figure 6.5 shows the MC results at T=0.03 and n=2/3 in applied field  $h_z$ . All the results consistently indicate two sharp crossovers while increasing  $h_z$ ; one is from the zero-field state to the kagome ice state by switching on  $h_z$ , and the other to the all-in/all-out ordered state at  $h_z \sim 0.34$ . Figure 6.5a depicts the results for  $m_z$  and its susceptibility  $\chi_z$ . They clearly indicate the presence of 1/3 magnetization plateau for  $0.1 \lesssim h_z \lesssim 0.3$  followed by rapid increase of  $m_z$  for larger  $h_z$  and a peak of  $\chi_z$  at  $h_z = 0.341(3)$ . As shown in Fig. 6.5b, the ratio of two-in one-out and one-in two-out configurations in the system  $\rho$ , defined by Eq. (6.4), stays close to 1 in the

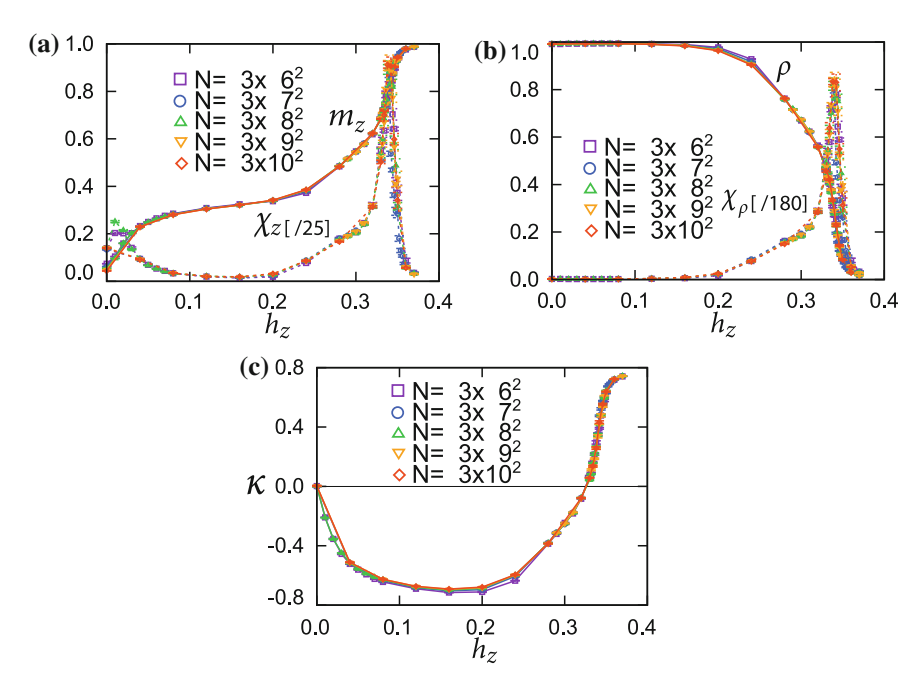


**Fig. 6.5** MC results for **a**  $m_z$  and  $\chi_z$ , **b**  $\rho$  and  $\chi_\rho$ , and **c**  $\kappa$  at n=2/3 and T=0.03. The data were calculated for the system sizes ranging from  $N=3\times6^2$  to  $3\times10^2$ 

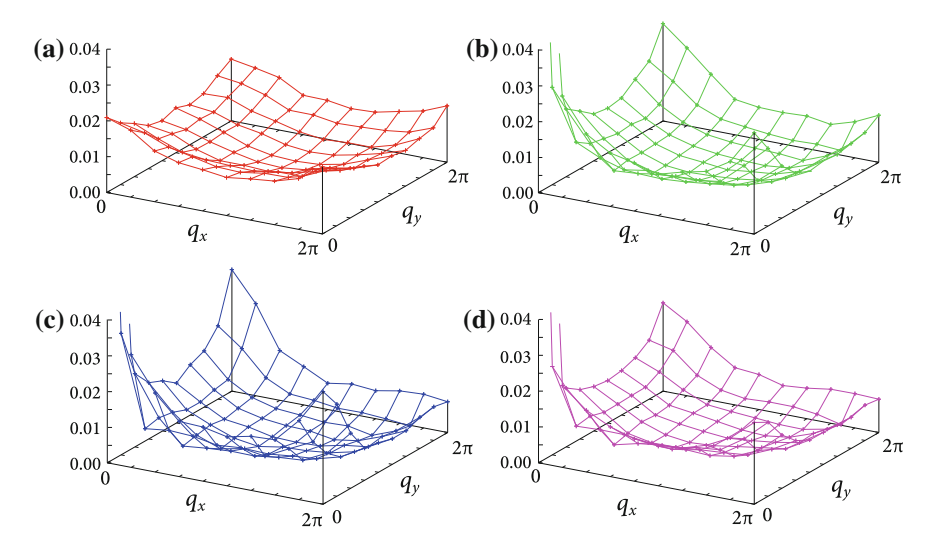


**Fig. 6.6** Spin structure factor for the localized Ising spins calculated by the MC simulation at T = 0.03 and **a**  $h_z = 0.00$ , **b** 0.08, **c** 0.16, and **d** 0.24. The results are for the system size with  $N = 3 \times 10^2$ 

plateau regime, while it decreases for larger  $h_z$ ; the corresponding susceptibility  $\chi_\rho$  shows a sharp peak at  $h_z=0.340(3)$ . Figure 6.5c shows the net scalar chirality  $\kappa$  defined by Eq. (6.5), where the sum is taken over all the triangles and the indices (i,j,k) are in the counterclockwise order in each triangle. It approaches and stays near the minimum value  $-\frac{4}{3\sqrt{3}}$ , followed by rapid increase for a higher field with showing a sign change at  $h_z=0.325(5)$ . These results are signatures of a crossover between the kagome ice state and all-in/all-out ordered state takes place by applying the external magnetic field.

We stress that the 1/3 plateau state in the MC simulation is a cooperative paramagnetic state where kagome-ice type local correlation is well developed but lacks long-range ordering. To confirm this, we calculated the magnetic structure factor by using the MC method. Figure 6.6 shows the results of  $S(\mathbf{q})$  for  $N=3\times 10^2$  at T=0.03 and n=2/3 calculated by MC method. The result at h=0 in Fig. 6.6a shows no magnetic Bragg peaks, which indicates no magnetic long-range ordering. We also note that a broad structure with maxima at  $\mathbf{q}=(0,0)$  is seen in Fig. 6.6a. One possible cause of this structure is the fluctuation toward a long-range magnetic order which is expected at a much lower temperature. Another possibility is that the structure is related to development of local correlation. At the parameter of the calculation, the kagome-liquid type local correlation is well developed, as is seen from Fig. 6.5b. Such development of local correlation sometimes gives rise to a characteristic structure in  $S(\mathbf{q})$ , such as the pinch points in spin ice compounds [4, 5]. However, it is necessary to perform the calculations for larger system sizes to precisely determine such a characteristic structure.

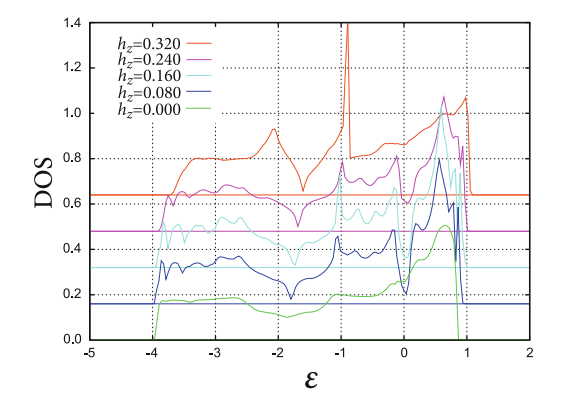
With applying the external magnetic field, a Bragg peak starts to develop at  $\mathbf{q}=\mathbf{0}$  which corresponds to the net magnetic moment. Figure 6.6b–d shows the results of  $S(\mathbf{q})$  under external magnetic field; these results corresponds to the magnetization plateau. The peak at  $\mathbf{q}=\mathbf{0}$  is clearly observed in all the results. However, no other Bragg peaks are observed in the results, indicating that there is no long-range ordering characterized by  $\mathbf{q}\neq\mathbf{0}$ .

# 6.3.2 Electronic and Transport Properties

The development of two magnetic states are also reflected in the electronic and transport properties. Figure 6.7 shows the results of DOS for  $N=3\times 10^2$  calculated by MC method at T=0.03 and n=2/3. The Fermi level for n=2/3 is set at  $\varepsilon=0$ . The result for  $h_z=0$  shows featureless DOS, while an energy gap starts to develop with applying external magnetic field, as is seen in the results for h=0.08 and 0.16. On the other hand, with applying stronger magnetic field, the gap become less obvious for h>0.16. The results for DOS are consistent with the results for  $\sigma_{xx}$  and  $\sigma_{xy}$  shown in Fig. 6.5d, which shows two humps in the result of  $\sigma_{xx}$ . Overall, the results of MC simulation under magnetic field well resemble those of the numerical diagonalization results shown in Fig. 6.2, and hence, the kagome ice insulating state is expected to be realized in the plateau region.

The presence of kagome ice insulator and its crossover to the all-in/all-out state are also seen in the transport properties. Figure 6.8 shows MC results for  $\sigma_{xx}$  and  $\sigma_{xy}$  at n=2/3 and t=0.03. With applying the magnetic field,  $\sigma_{xx}$  decreases rapidly and approaches zero in the magnetic plateau region shown in Fig. 6.5a. However, with further increasing the magnetic field,  $\sigma_{xx}$  shows an increase and a hump. For  $\sigma_{xy}$ , with the application of the magnetic field, it shows rapid increase and approaches 1.0 in the kagome ice plateau region, consistently with the gap formation seen in the MC results for DOS (Fig. 6.7). On the other hand, with further increasing the magnetic

**Fig. 6.7** DOS calculated by MC simulation at T = 0.03 and  $N = 3 \times 10^2$  while varying external magnetic field. The Fermi level at n = 2/3 is set at  $\varepsilon = 0$ . For each data, offset of  $\Delta = 0.16$  is taken for better visibility



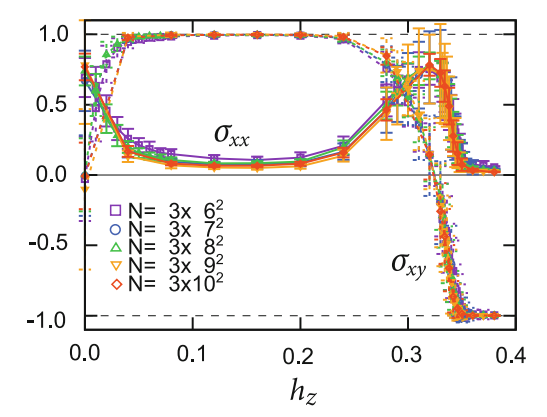


**Fig. 6.8** MC results for  $\sigma_{xx}$  and  $\sigma_{xy}$  with the application of the magnetic field at n=2/3 and T=0.03. The calculations were done for  $N=3\times 6^2-3\times 10^2$  size systems

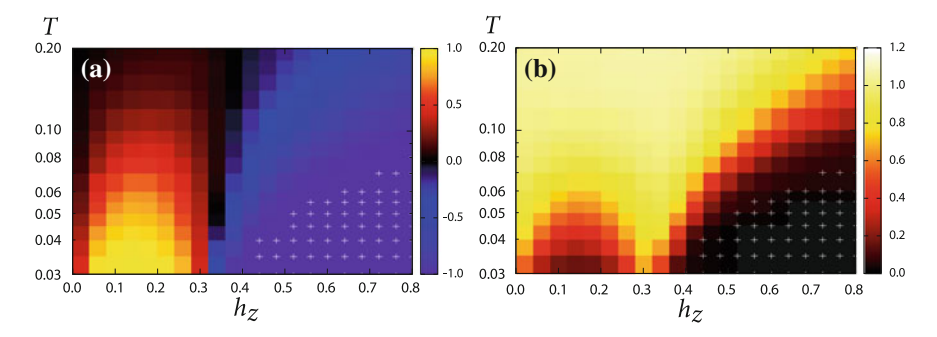


**Fig. 6.9** Contour plots of the MC results for **a**  $\sigma_{xy}$  and **b**  $\sigma_{xx}$  in the  $h_z$ -T plane. The calculations were done for  $N = 3 \times 6^2$  size systems. The white crosses show the parameters at which the MC acceptance rate becomes lower than 1 %

field,  $\sigma_{xy}$  shows a sign change at  $h_z = 0.328(7)$  accompanied by the hump of  $\sigma_{xx}$ . These features resemble the result of exact diagonalization shown in Fig. 6.4.

In the last, in Fig. 6.9, we mapped out the conductances in the  $h_z$ -T plane. The two insulating phases are also clearly observed in the contour plots of  $\sigma_{xy}$  and  $\sigma_{xx}$  in the  $h_z$ -T plane. Figure 6.9a shows the result of  $\sigma_{xy}$ . It clearly indicates two regimes with a finite Hall conductivity  $\sigma_{xy}$  of an opposite sign: a dome-like region centered at  $h_z \sim 0.15$ , and another one for  $h_z \gtrsim 0.34$ . The two regimes are also clearly indicated by strong suppression of  $\sigma_{xx}$ , as shown in Fig. 6.9b. Thus, the phase diagram shows that the model in Eq. (6.1) exhibits two different insulating regimes with different topological characters, as expected in the analysis by using the simple average in Sect. 6.2.

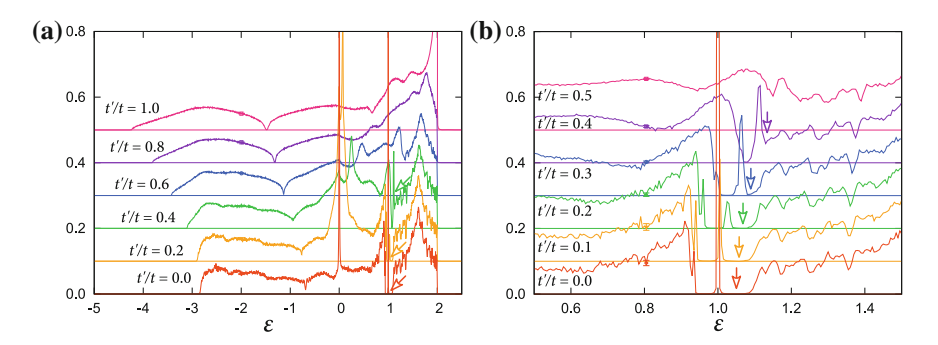
# **6.4** Anisotropic Pyrochlore Lattice

In the last, we discuss the stability of the energy gap when three dimensionality is introduced. Here, we consider an anisotropic pyrochlore lattice model with hopping integral t=1 for the intraplane hoppings in a kagome plane and t' interplane hoppings. The intraplane hoppings are the hoppings in the  $\langle 111 \rangle$  kagome planes [the purple plane in Fig. 6.1a]. On the other hand, the interplane hoppings are those connecting the  $\langle 111 \rangle$  triangular and the  $\langle 111 \rangle$  kagome planes; the model can also be viewed as kagome planes weakly-coupled to the sandwiched triangular planes.

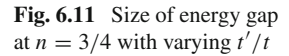
Figure 6.10 shows the result of the electronic DOS calculated by taking simple average over different kagome-ice spin configurations; the moments on the triangular planes are fixed ferromagnetically along the net magnetic moments of kagome planes. Such situation is expected to be realized in pyrochlore material Dy<sub>2</sub>Ti<sub>2</sub>O<sub>7</sub> with external field applied along  $\langle 111 \rangle$  direction [2, 6, 10]. Figure 6.10a shows the overall structure of DOS. In this model, as there is extra electrons from the triangular planes, the energy gap at n=2/3 of the kagome model corresponds to the energy gap at n=3/4 of the t'/t=0 case [The position of the arrow in the lowest DOS in Fig. 6.10a]. By introducing t', the energy gap at n=3/4 becomes smaller and vanishes above t'/t=0.4.

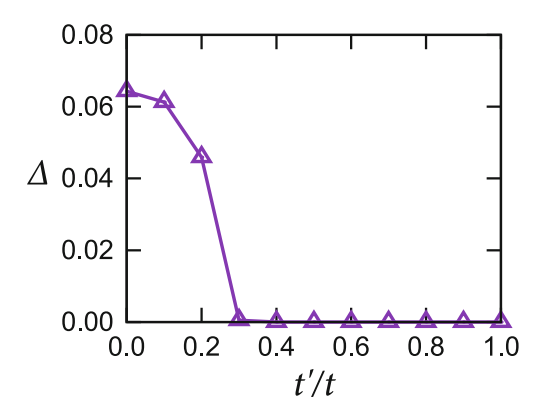
Figure 6.10b shows the enlarged figure of DOS around the energy gap at n = 3/4. In the t'/t = 0 limit, there exist two energy gaps separated by the flat band at  $\varepsilon = 1$ ; the upper one corresponds to the gap at n = 2/3 in the kagome lattice case. When introducing t', the gap becomes smaller and closes around  $t'/t \sim 0.3$ . On the other hand, the lower gap persists to  $t'/t \sim 0.4$ .

The dependence of energy gap with respect to t' is summarized in Fig. 6.11. The energy gap in Fig. 6.11 is estimated from the energy difference between the highest occupied energy level and lowest unoccupied energy level. As indicated in Fig. 6.10, the result shows that the energy gap closes at  $t'/t \sim 0.3$ . The results indicate that, in



**Fig. 6.10** Density of states for the anisotropic pyrochlore lattice with varying t'/t. **a** Overall structure and **b** enlarged figure around the energy gap at n = 3/4. The calculations were done for  $8^3$  superlattice of  $N = 4 \times 6^3$  sites





the presence of interlayer couplings, the kagome ice insulating state persists when the interlayer coupling is weaker or similar to 1/3 of the interlayer couplings.

# 6.5 Discussion and Summary

In this chapter, we presented comprehensive analyses that provide convincing evidence for the existence of kagome ice AHI in the intermediate T classical spinliquid regime. This is a peculiar topological state of matter in the absence of Landau levels, spin-orbit coupling, and magnetic ordering. Upon further decreasing T, it is expected that effective further-neighbor interactions induced by the spin-charge coupling stabilize some magnetic order, whose ordering pattern may become complicated depending on  $h_z$  as well as the electron density. It is left for future study to investigate the full phase diagram including the low-T ordered phases.

On the other hand, an extension of the model to more realistic situation on the three-dimensional pyrochlore lattice was studied in Sect. 6.4. By analyzing the electronic density of states, we showed that kagome ice insulator is stable for  $t'/t \lesssim 0.3$ . For larger t', the quantization of  $\sigma_{xy}$  no longer holds and the behavior of  $\sigma_{xy}$  under magnetic field shows a featureless curve. However, it is expected that the non-monotonic change of  $\sigma_{xy}$  remains in applied magnetic field. It is interesting to note that such non-monotonic behavior of the Hall resistivity was observed in the  $\langle 111 \rangle$  magnetic field in  $Pr_2Ir_2O_7$  [3, 9].

#### References

- 1. P.W. Anderson, H. Hasegawa, Phys. Rev. **100**, 675 (1955)
- 2. H. Aoki, T. Sakakibara, K. Matsuhira, Z. Hiroi, J. Phys. Soc. Jpn. 73, 2851 (2004)
- 3. L. Balicas, S. Nakatsuji, Y. Machida, S. Onoda, Phys. Rev. Lett. 106, 217204 (2011)

References 91

4. T. Fennell, P.P. Deen, A.R. Wildes, K. Schmalzl, D. Prabhakaran, A.T. Boothroyd, R.J. Aldus, D.F. McMorrow, S.T. Bramwell, Science **326**, 415 (2009)

- 5. C.L. Henley, Ann. Rev. Condens. Matter Phys. 1, 179 (2010)
- 6. R. Higashinaka, H. Fukazawa, K. Deguchi, Y. Maeno, J. Phys. Soc. Jpn. 73, 2845 (2004)
- 7. H. Ishizuka, M. Udagawa, Y. Motome, Phys. Rev. B 83, 125101 (2011)
- 8. D. Loss, P.M. Goldbart, Phys. Rev. B 45, 13544 (1992)
- Y. Machida, S. Nakatsuji, Y. Maeno, T. Tayama, T. Sakakibara, S. Onoda, Phys. Rev. Lett. 98, 057203 (2007)
- K. Matsuhira, Z. Hiroi, T. Tayama, S. Takagi, T. Sakakibara, J. Phys.: Condens. Matter 14, L559 (2002)
- 11. R. Melko, M.J.P. Gingras, J. Phys.: Condens. Matter 16, R1227 (2004)
- 12. K. Ohgushi, S. Murakami, N. Nagaosa, Phys. Rev. B 62, 6065(R) (2000)
- 13. S. Onoda, N. Nagaosa, Phys. Rev. Lett. **90**, 196602 (2003)
- J. Ye, Y.B. Kim, A.J. Millis, B.I. Shraiman, P. Majumdar, Z. Tešanovic, Phys. Rev. Lett. 83, 3737 (1999)
- 15. C. Zener, Phys. Rev. 82, 403 (1951)

# Chapter 7 Spin-Charge Coupled Phases on a Pyrochlore Lattice

**Abstract** In this chapter, we study a spin-ice type Kondo lattice model on a pyrochlore lattice. The finite temperature phase diagram of the Kondo lattice model is studied by using an efficient Monte Carlo method using the polynomial expansion technique (Sect. 2.3). This algorithm is an unbiased simulation method with well controlled approximation, that allows us to study spin-charge coupled systems using large system sizes. In this section, we present the results up to 2048 sites. By the large-scale Monte Carlo simulation, we clarify the phase diagram of the model; we find a new 32-sublattice magnetic phase with concomitant charge modulation, along with other phases such as two-in two-out and all-in/all-out orders. We also show that the spin and charge order can be switched by external magnetic field to a different one accompanied by a half magnetization plateau.

#### 7.1 Model and Method

In this section, we briefly review the model and method we used in this chapter. The model is explained in Sect. 7.1.1 and the Monte Carlo (MC) method we used in Sect. 7.1.2. Further details on the model and the method is given in Chap. 2.

# 7.1.1 Spin-Ice Kondo Lattice Model

We here consider a Kondo lattice model with Ising spins on a pyrochlore lattice, whose Hamiltonian is given by

$$H = -t \sum_{\langle i,j \rangle, \sigma} \left( c_{i\sigma}^{\dagger} c_{j\sigma} + \text{H.c.} \right) - J \sum_{i} \mathbf{S}_{i} \cdot \boldsymbol{\sigma}_{i}. \tag{7.1}$$

The first term represents hopping of itinerant electrons, where  $c_{i\sigma}$  ( $c_{i\sigma}^{\dagger}$ ) is the annihilation (creation) operator of an itinerant electron with spin  $\sigma = \uparrow, \downarrow$  at *i*th site, and

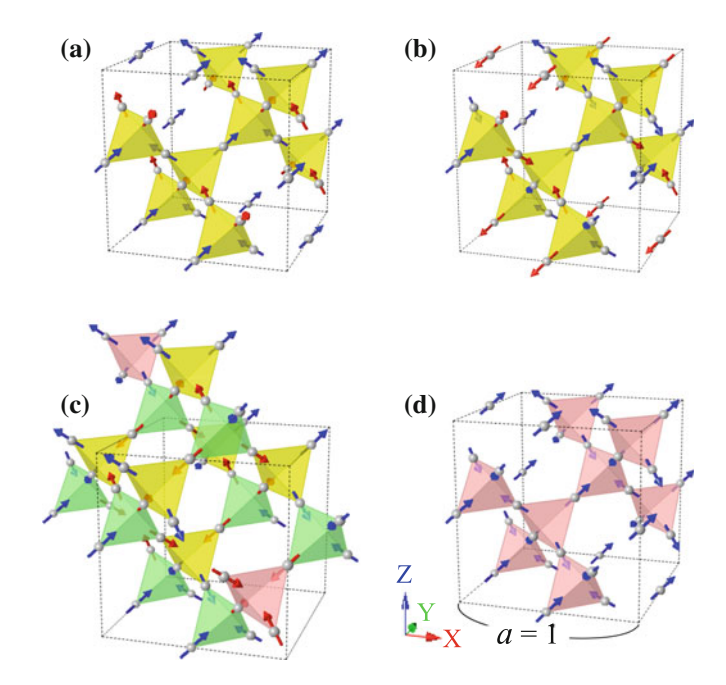


Fig. 7.1 Spin configurations for **a** ice-ferro, **b** ice- $(0, 0, 2\pi)$ , **c** 32-sublattice, and **d** all-in/all-out order

t is the transfer integral for nearest-neighbor (NN) sites. The sum  $\langle i, j \rangle$  is taken over NN sites on the pyrochlore lattice. The second term is the onsite interaction between localized moments and itinerant electrons, where J is the Kondo coupling.  $S_i$  and

$$\sigma_i = \sum_{\alpha,\beta} c_{i\alpha}^{\dagger} \tau_{\alpha\beta} c_{i\beta} \tag{7.2}$$

represent the localized Ising moment and itinerant electron spin at *i*th site, respectively; we take  $|\mathbf{S}_i| = 1$ . Here,  $\tau_{\alpha\beta}$  is the vector of  $\alpha\beta$  components of the Pauli matrices.

In this section, we consider the Ising moments with anisotropy axis along the local  $\langle 111 \rangle$  direction, i.e., along the line connecting the centers of two tetrahedra which the spin belongs to (see Fig. 7.1). Hereafter, we take t=1 as the unit of energy and the Boltzmann constant  $k_{\rm B}=1$ . For the unit of length, we take the lattice constant of cubic unit cell a=1 as shown in Fig. 7.1d.

#### 7.1.2 Monte Carlo Simulation

Thermodynamic properties of the model in Eq. (7.1) are investigated by MC simulation using both the exact diagonalization (ED) and polynomial expansion method

7.1 Model and Method 95

(PEM). In relatively higher density region  $n_e \gtrsim 0.15$ , we concluded that PEM with m=40 polynomials gives good convergence ( $n_e = \sum_{i\sigma} \langle c_{i\sigma}^{\dagger} c_{i\sigma} \rangle / N$ ). On the other hand, the convergence appears to be much worse for  $n_e \lesssim 0.15$ , and hence, we employed ND instead of PEM. Further details of the benchmarks on PEM method are given in Chap. 9.

In this section, the calculations were conducted up to  $N=4\times8^3$  for the MC with PEM and  $N=4\times4^3$  for ED. Typically, we perform more than 3000 MC steps for the calculation of physical quantities. The results are divided into three bins to estimate the statistical error. For system size  $N=4\times8^3$ , one MC step takes about 30 seconds by using 1024 CPU cores in the System B (SGI Altix ICE 8400EX) at ISSP supercomputer center.

#### 7.1.3 Physical Quantities

In the MC simulation, we computed magnetic order parameter defined for  $\alpha$ th sub-lattice,

$$M_{\mathbf{q}} = \left(\frac{S_{\mathbf{q} \text{ max}}^{(\alpha)}}{N_{\mathbf{t}}}\right)^{\frac{1}{2}},\tag{7.3}$$

to determine the development of magnetic orders in low temperature. Here,  $S_{\mathbf{q} \text{ max}}^{(\alpha)}$  is the maximum component of sublattice-dependent spin structure factor,

$$S_{\mathbf{q}}^{(\alpha)} = \frac{1}{N_{t}} \sum_{i,j \in \alpha} \langle \mathbf{S}_{i} \cdot \mathbf{S}_{j} \rangle \exp\left[i\mathbf{q} \cdot (\mathbf{r}_{i} - \mathbf{r}_{j})\right], \tag{7.4}$$

where  $N_t = N/4$  is the number of tetrahedra,  $\mathbf{r}_i$  is the position of ith site, and  $\mathbf{q}$  is the wave number. In addition, we also calculated the probability to find each configuration of all-in or all-out  $(P_{40})$ , three-in one-out or one-in three-out  $(P_{31})$ , and two-in two-out  $(P_{22})$ . The magnetic pattern in each phase are determined from the magnetic order and local correlation parameters.

The spatial modulation in the charge degree of freedom is detected by a similar order parameter defined by

$$n_{\mathbf{q}} = \left[\frac{N_{\mathbf{q} \max}^{(\alpha)}}{N_{\mathbf{t}}}\right]^{1/2},\tag{7.5}$$

where  $N_{\bf q}^{(\alpha)}$  is the charge structure factor for  $\alpha$ th sublattice defined by

$$N_{\mathbf{q}}^{(\alpha)} = \frac{1}{N_{t}} \sum_{i,j \in \alpha} \langle \hat{n}_{i} \hat{n}_{j} \rangle \exp\left[i\mathbf{q} \cdot \left(\mathbf{r}_{i} - \mathbf{r}_{j}\right)\right], \tag{7.6}$$

and  $\hat{n}_i$  is the electron number operator for ith site

$$\hat{n}_i = \sum_{\sigma} c_{i\sigma}^{\dagger} c_{i\sigma}. \tag{7.7}$$

We also calculated the charge modulation  $\Delta n$  defined by the difference of the electron densities between the kagome and triangular planes perpendicular in the [111] direction.

#### 7.2 Phase Diagram

Figure 7.2a shows the phase diagram of the model in Eq. (7.1) at J=2 obtained by the MC simulation. There are four dominant phases at low T in the calculated density region  $0 \le n_e \le 0.3$ . The open symbols show the transition temperatures  $T_c$  for each phase determined from the inflection point or sharp jump of T dependence of the order parameter  $M_{\mathbf{g}}$ .

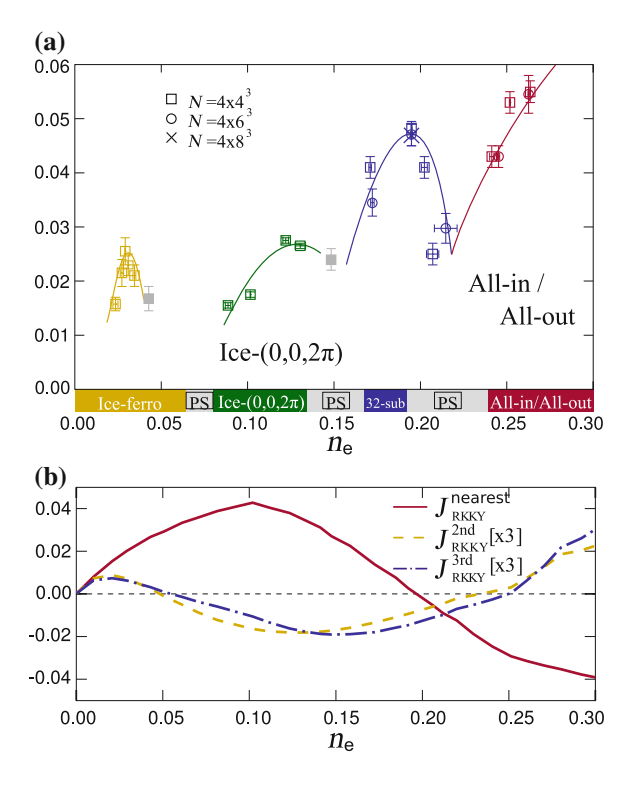
In the low density region  $n_e \lesssim 0.04$ , the  $\mathbf{q} = 0$  two-in two-out order shown in Fig. 7.1a evolves in the low T region below  $T_c \lesssim 0.025$ . We call this phase the ice-ferro phase hereafter. While increasing the electron density, a different ordering develops in the region of  $0.08 \lesssim n_e \lesssim 0.15$ . The ordering structure is of layer type with  $\mathbf{q} = (0, 0, 2\pi)$ , in which every tetrahedron retains two-in two-out icerule configuration, while the net moments of tetrahedra form a collinear layer-type ordering (Fig. 7.1b); we call this the ice- $(0, 0, 2\pi)$  phase. The ordering pattern is the same as that found in a spin ice model including the long-range dipolar interaction [2]. A new phase appears in the higher density region for 0.15  $\lesssim n_e \lesssim$  0.22. The magnetic structure is a 32-sublattice long-range order with  $\mathbf{q} = (\pi, \pi, \pi)$ , in which all third-neighbor spins are aligned in an antiferromagnetic (AFM) manner. Here and hereafter we refer to the third neighbors as the six second-neighbor sites along the straight chains running in the pyrochlore lattice. Note that the AFM third-neighbor interaction is free from frustration, uniquely selecting the 32-sublattice ordering, if other interactions are negligible. For  $n_e \gtrsim 0.22$ , the system exhibits the  $\mathbf{q} = 0$  allin/all-out order (Fig. 7.1d). The closed symbols at  $n_e \sim 0.05$  and 0.15 indicate phase transitions to other complex magnetic orderings, whose magnetic unit cells reach the system size; we need larger system sizes to confirm the orderings.

We also calculated the phase diagram at T=0 by comparing the ground state energy for the four ordered states appearing in the MC simulation. The result is shown in the strip at the bottom axis of Fig. 7.2a. All the four phases appear in the corresponding density regions where the MC results show their instabilities. The phase transitions between different phases are all first order at T=0 accompanied by a jump of the electron density, that is, phase separation (PS).

The trend of the phase diagram is reasonable from the viewpoint of the RKKY interactions [3]. Figure 7.2b shows the nearest-, second-, and third-neighbor components of the RKKY interaction, which are calculated by using the bare magnetic

7.2 Phase Diagram 97

Fig. 7.2 a Phase diagram of the model in Eq. (7.1) at J = 2. The open symbols show  $T_c$  for the four phases, while the closed ones are for other complex orders. The lines are guides for the eyes. The bottom strip shows the ground-state phase diagram obtained by comparing the energy of four phases. PS indicates phase separation. **b** RKKY interactions for the nearest-, second-, and third-neighbor spins calculated by using the second-order perturbation in terms of J for the model (7.1). The latter two are multiplied by factor 3 for clarity



susceptibility for the noninteracting tight-binding model at J=0. In the lowest density region  $n_e \lesssim 0.05$ , all three components are positive [ferromagnetic (FM)], because of the small Fermi surface. This is consistent with the ice-ferro order appearing in this region (Fig. 7.1a). While increasing the electron density above 0.05, the second- and third-neighbor RKKY interactions change their signs to be AFM, while the NN interaction remains dominantly FM. The ice- $(0, 0, 2\pi)$  order is stabilized as a compromise of these interactions (Fig. 7.1b). While further increasing the electron density, the NN RKKY interaction also changes its sign at  $n_e \sim 0.20$ . In the vicinity of this density, the NN interaction becomes relatively weak compared to the further-neighbor ones. The 32-sublattice order emerges in this region. Indeed, the magnetic structure of 32-sublattice order is characterized by AFM ordering of the third-neighbor spins (Fig. 7.1c), while it shows no apparent change in NN spin correlations from high-T paramagnetic state, as discussed below. In the higher density region  $n_e \gtrsim 0.22$ , the NN interaction becomes AFM, and the all-in/all-out order is stabilized. The absence of frustration in the dominant NN AFM interaction makes  $T_c$  much higher than other phases.

It should be stressed that, although the sequence of magnetic orderings is qualitatively understood by the analysis of RKKY interactions, it is difficult to infer a priori the phase diagram in the nonperturbative region of J only by the form of RKKY

interactions. For instance, critical temperatures are difficult to predict. Indeed, our phase diagram is qualitatively different from that for a spin-only RKKY model [1]. The unbiased MC simulation explicitly taking account of itinerant electron degree of freedom is crucial to identify the phase diagram.

# 7.3 Temperature Dependence of Physical Quantities

We next look into the T dependences of the order parameters and short-range spin correlations within each tetrahedron. The local spin correlations are measured by calculating  $P_{40}$ ,  $P_{31}$ , and  $P_{22}$ . Figure 7.3a shows the results in the ice-ferro region. The results show an enhancement of the ice-rule local correlation  $P_{22}$  prior to phase transition at  $T_c \simeq 0.023$ , while  $P_{40}$  and  $P_{31}$  are strongly suppressed.  $P_{22}$  also becomes dominant in the ice- $(0, 0, 2\pi)$  phase region, as shown in Fig. 7.3b. Regarding to the order of transition, a sharp jump is observed for the ice- $(0, 0, 2\pi)$  ordering (Fig. 7.3b), which is an indicative of a first order transition. This is presumably due to the six-fold degeneracy of the ordered ground state, in analogy with the six-state Potts model [4]. In this respect, the transition to the ice-ferro state might also be of first order, while the MC data do not show clear indication of discontinuity in the MC results. This might presumably be of the small system size. Indeed, recent study on an effective spin model using RKKY interaction shows weak first order transition [3]. On the other hand, the results for the all-in/all-out region show contrasting behavior (Fig. 7.3d), in which the all-in/all-out correlation  $P_{40}$  is enhanced prior to the phase transition at  $T_c \simeq 0.051$ .

In sharp contrast, for the 32-sublattice order, the local correlation parameters show weak T dependence, even in the critical region near  $T_c \simeq 0.047$ . This implies that the ordering is not driven by NN spin correlations, as discussed above. Another interesting point here is that the 32-sublattice magnetic order exhibits a concomitant charge disproportionation. In Fig. 7.3c, we plot the charge disproportionation  $n_{\bf q}$ . The result clearly indicates the emergence of concomitant charge disproportionation below  $T_c$ ; the temperature of the inflection point of  $n_{\bf q}$  is in agreement with that of  $M_{\bf q}$ . The wave number for charge structure factor is  ${\bf q}=(0,0,2\pi)$ . The local electron density is higher at the sites belonging to the all-in/all-out tetrahedra compared with the other sites (see Fig. 7.1c). On the other hand, all the other phases in Fig. 7.2 are charge uniform; the 32-sublattice order is the only phase showing a concomitant charge disproportionation.

This could be understood by a simple perturbation argument. A standard secondorder perturbation in terms of J predicts that the underlying magnetic ordering restricts a possible wave number for charge disproportionation to  $\mathbf{q} = \mathbf{q}_{\alpha_1} + \mathbf{q}_{\alpha_2} + \mathbf{G}$ , where  $\mathbf{q}_{\alpha}$  are the magnetic wave numbers and  $\mathbf{G}$  is a reciprocal lattice vector. For the ice-ferro, stripe, and all-in/all-out phases, no charge disproportionation is allowed because  $2\mathbf{q}_{\alpha} = \mathbf{G}$ . For the 32-sublattice order, however, a charge disproportionation with  $\mathbf{q} \neq \mathbf{G}$  is allowed as  $\mathbf{q}_{\alpha}$  is dependent on  $\alpha$ .

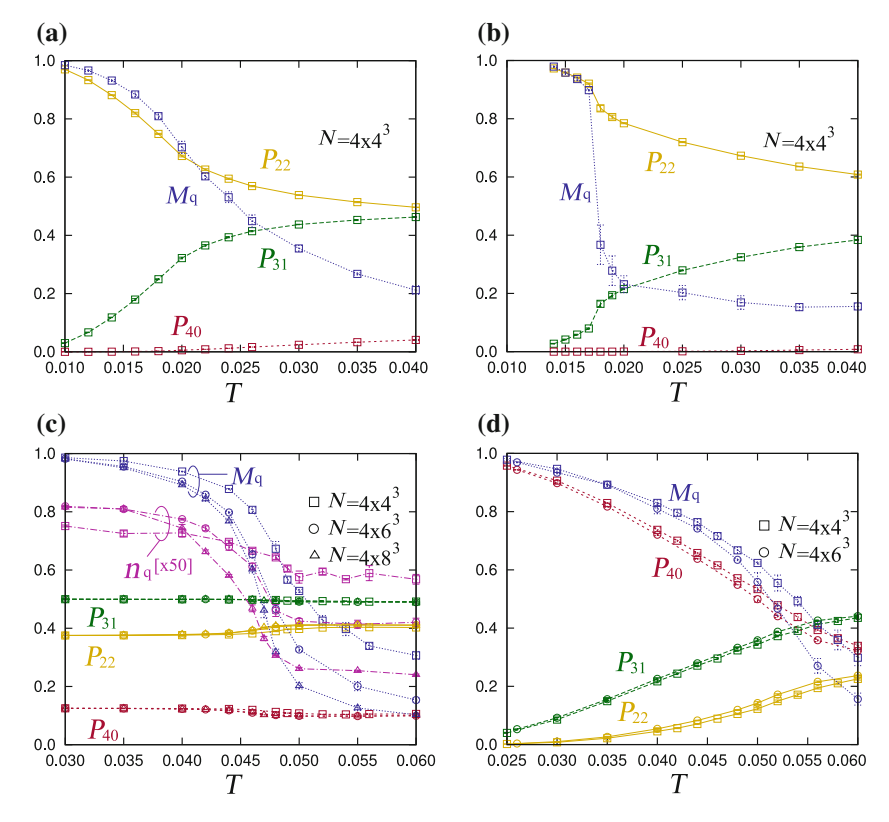
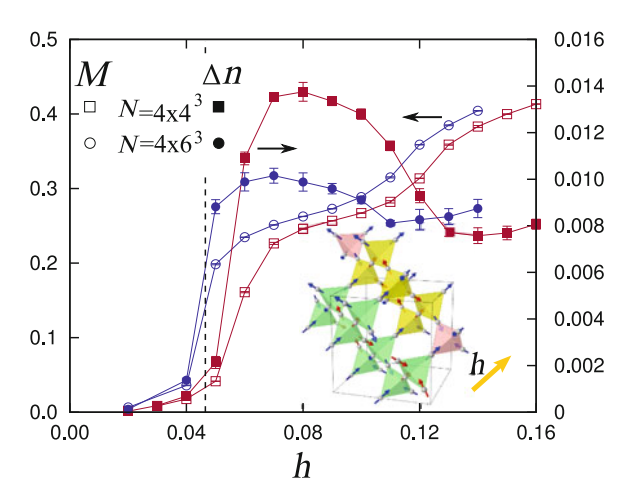


**Fig. 7.3** T dependences of the order parameter  $M_{\bf q}$  and the ratios of tetrahedra with different spin configurations,  $P_{22}$ ,  $P_{31}$ , and  $P_{40}$ , at J=2. The data are calculated at a fixed chemical potential  $\mu$ : **a**  $\mu=-5.9$  [corresponding to  $n_e=0.030(2)$ ], **b**  $\mu=-4.8$  [ $n_e=0.099(3)$ ], **c**  $\mu=-3.4$  [ $n_e=0.195(1)$ ], and (d)  $\mu=-2.4$  [ $n_e=0.264(3)$ ]. The magnetic ordering wave vectors for each phase are (a), **d**  ${\bf q}=0$ , (b)  $(0,0,2\pi)$ , and (c)  $(\pi,\pi,\pi)$ . In (c), the charge disproportionation  $n_{\bf q}$  with  ${\bf q}=(0,0,2\pi)$  is also plotted

# 7.4 Magnetic Field Switching of Charge Disproportionation

In this section, we study the behavior of 32-sublattice order under external magnetic field. In particular, we focus on the charge modulation in this phase, which we show to be switchable by applying an external magnetic field. Figure 7.4 shows the magnetization  $M = |\sum_i \mathbf{S}_i|/N$  and the charge disproportionation under a magnetic field  $\mathbf{h}$  applied along a [111] direction at T = 0.025 ( $\Delta n$ ). For simplicity, we apply a magnetic field only to localized Ising spins. Under a weak magnetic field of up to  $h \sim 0.04$ , the 32-sublattice order at h = 0 remains robust and M remains almost zero. At higher magnetic fields, M increases abruptly, indicating a first-order transition to a different phase, which is characterized by the half-magnetization plateau  $M \simeq 1/4$ 

Fig. 7.4 Magnetization M and charge disproportionation  $\Delta n$  under the external magnetic field h along a [111] direction at  $\mu = -3.4$  and T = 0.025. The vertical dashed line is an estimate of the critical field at T = 0,  $h_c \simeq 0.0465$ , obtained by comparing the ground state energies in a sufficiently large system. The inset shows a schematic picture of the magnetic order in the plateau state at  $M \simeq 1/4$ 



(Due to the non-colinear anisotropy axes, the full saturation is M=1/2 in the present model). This plateau state remains stable up to  $h \sim 0.1$ . The magnetic structure of the plateau phase is obtained by aligning all the spins on triangular layers in the field direction (see the inset of Fig. 7.4). Although there is a finite size effect, the data for  $N=4\times6^3$  show the transition to the plateau state very close to  $h_c$  estimated at T=0 in the thermodynamic limit. For the high-field region above the plateau state, we could not obtain converged results owing to the poor convergence of PEM.

Interestingly,  $\Delta n$  also changes from almost zero to nonzero abruptly at the critical field, namely, the charge disproportionation is simultaneously switched to that along the [111] direction. The switching may be explained as follows. As mentioned above, the charge disproportionation with  $\mathbf{q}=(0,0,2\pi)$  in the zero-field state appears to be dominantly driven by the inhomogeneity of NN spin correlations. In contrast, in the plateau state in applied magnetic field, the NN mean fields have uniform, nonzero magnitude at all the sites. Instead, the mean fields from second-neighbor spins along the chains are different between the triangular and kagome sites, which may lead to the charge disproportionation along the [111] direction in the plateau state.

# 7.5 Discussion and Summary

To summarize, we have numerically investigated the Kondo lattice model with Ising spins with the local [111] easy-axis spin anisotropy on a pyrochlore lattice, which potentially describes metallic pyrochlore oxides. By using the state-of-theart Monte Carlo simulation that can directly simulate the Kondo lattice models, we found the 32-sublattice ordered phase in the phase competing region between the two-in two-out and all-in/all-out phases. This phase exhibits a charge disproportionation concomitant with the magnetic order. The spin and charge pattern can be switched

by an external magnetic field to a different one that shows a half-magnetization plateau. Our result demonstrates that spin-charge coupling on a frustrated lattice induces rich behavior than that in localized spin systems.

#### References

- 1. A. Ikeda, H. Kawamura, J. Phys. Soc. Jpn. 77, 073707 (2008)
- 2. R. Melko, M.J.P. Gingras, J. Phys.: Condens. Matter 16, R1227 (2004)
- 3. H. Ishizuka, M. Udagawa, Y. Motome, JPS Conf. Ser. 3, 014013 (2014)
- 4. F.Y. Wu, Rev. Mod. Phys. **54**, 235 (1982)

# **Chapter 8 Spin-Cluster State in a Pyrochlore Lattice**

Abstract In this chapter, we study magnetic phase diagram and transport phenomena in a double-exchange model on a pyrochlore lattice with spin-ice type localized moments. Magnetic properties at finite temperatures of the model were studied by two different approaches: a classical Monte Carlo simulation of an effective spin model and the Monte Carlo simulation of the double-exchange model. With these two methods, we show that the competition between ferromagnetic double-exchange interaction and antiferromagnetic superexchange interaction leads to an interesting spin-cluster phase. In this phase, four-spin clusters are formed and arranged periodically, which violates spacial inversion without breaking time reversal symmetry. We also show that the spin-cluster phase exhibits spin Hall effect via the fluctuating noncoplanar spin textures.

#### 8.1 Model and Method

In this section, we describe the model and method we used in this chapter. In Sect. 8.1.1, we introduce the spin-ice double-exchange (DE) model. The details of the method we used for the effective spin model, a perturbation theory and a classical Monte Carlo (MC) simulation, are explained in Sects. 8.1.2 and 8.1.3, respectively. Details of the MC simulation for the DE model is given in Sect. 8.1.4. Finally, in Sect. 8.1.5, we describe physical quantities we calculated in this chapter.

# 8.1.1 Spin-Ice Double-Exchange Model

In this section, we consider the strong-coupling limit of the Kondo lattice model we studied in Chap. 7, a DE model [1, 19] on a pyrochlore lattice with Ising localized moments. The Ising moments have anisotropy axis along local [111] axis (see Fig. 8.1a). The Hamiltonian is given by

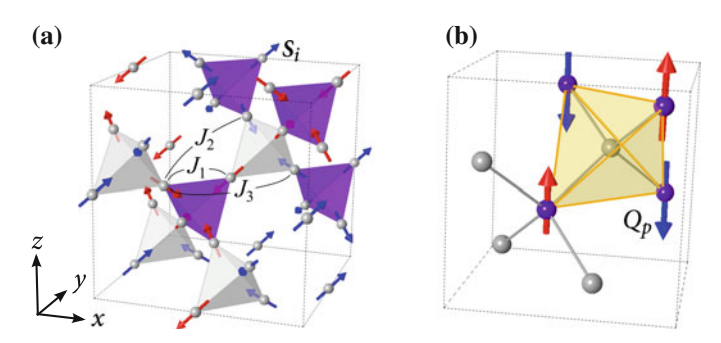


Fig. 8.1 Schematic pictures of  $\bf a$  a pyrochlore lattice and  $\bf b$  diamond lattice composed of the centers of tetrahedra in  $\bf a$ . The definition of interactions in the effective Ising model in Eq. (8.9) are also shown in  $\bf a$ 

$$H = -\sum_{\langle i,j\rangle} (t_{ij}c_i^{\dagger}c_j + \text{H.c.}) + J_{\text{AFM}} \sum_{\langle i,j\rangle} \mathbf{S}_i \cdot \mathbf{S}_j.$$
 (8.1)

Here,  $c_i$  ( $c_i^{\dagger}$ ) is the annihilation (creation) operator of an itinerant electron at ith site. The spin index is dropped as the spin of itinerant electron is aligned parallel to the localized Ising moment  $S_i$  at each site. Instead, the effective transfer integral  $t_{ij}$  depends on the relative angle of neighboring Ising spins, as explained in Sect. 1.2.2. The anisotropy axis of the Ising spin is site-dependent and along the local [111] direction, as shown in Fig. 8.1a. In Eq. (8.1), the sum  $\langle i,j \rangle$  is taken over nearest-neighbor (NN) sites on the pyrochlore lattice. The second term in Eq. (8.1) is the antiferromagnetic (AFM) interaction between the NN Ising moments. This is a minimal model including the [111] anisotropy, spin-charge coupling, and geometrical frustration, which are all present in many pyrochlore oxides [3]. In this section, hereafter, we set the unit of energy t=1, the lattice constant of cubic unit cell a=1, and the Boltzmann constant  $k_B=1$ . The unit of conductance is set as  $e^2/h=1$  (e is the elementary charge of electron).

In the current model, AFM interaction  $J_{\text{AFM}}$  prefers all-in or all-out, while the ferromagnetic (FM) DE interaction favors a two-in two-out configuration of Ising moments in each tetrahedron (see Fig. 1.4 for spin configurations in spin ice). In addition to this competition, the kinetic motion of electrons induces more complicated interactions. Hence, we expect phase competition by controlling  $J_{\text{AFM}}$ . In the following, we particularly focus on the competition between different electronic and magnetic phases in the model in Eq. (8.1) at quarter filling of electrons,  $n = \frac{1}{N} \sum_i \langle c_i^{\dagger} c_i \rangle = 1/4$ , where N is the number of sites.

8.1 Model and Method 105

## 8.1.2 Perturbation Theory

As we studied in Chap. 7, we can study the model in Eq. (8.1) using an MC method. However, as the MC simulation is highly cpu demanding, we first try to capture the overall picture of the phase competition by analyzing an effective spin model with kinetic-driven interactions. To derive the effective spin model, we consider a perturbation expansion for the hopping term from the strong-coupling limit of Isingspin Kondo lattice model. In this method, we map the spin-ice model onto an Ising model on a pyrochlore lattice with Ising spin  $\tilde{S}_i$  on site i, where  $\tilde{S}_i = \pm 1$  is the projected spin parameter to a local [111] vector  $\mathbf{n}_i$ ,  $\mathbf{S}_i = \tilde{S}_i \mathbf{n}_i$ . The details of this method is given in Sect. 2.5. This method is expected to be useful in the cases in which the relative angle of anisotropy axis for NN spins is close to  $\pi/2$ .

# 8.1.3 Monte Carlo Simulation for the Effective Ising Spin Model

We investigate the phase diagram of the effective spin model derived by the perturbation theory in Sect. 8.1.2 using a classical MC simulation. For efficient MC sampling, in addition to the single-spin flip update, we adopt a tetrahedron update, in which four spins in a tetrahedron are flipped at once, by using the heat bath method. The calculations were typically done with  $1.2 \times 10^6$  ( $4.9 \times 10^6$ ) MC steps for  $N = 4 \times 6^3$  and  $4 \times 8^3$  ( $N = 4 \times 10^3$  and  $4 \times 12^3$ ) after the thermalization of  $2.2 \times 10^5$  ( $9.2 \times 10^5$ ) MC steps.

# 8.1.4 Monte Carlo Simulation for the Double-Exchange Model

In addition to the effective spin model, in Sect. 8.3, we directly investigate the DE model in Eq. (8.1) by the polynomial expansion Monte Carlo method (PEMC) [8], the same algorithm we used in Chap. 7. The details of the algorithms are described in Sect. 2.2 and the benchmarks for this algorithm for finite J is given in Chap. 9.

In the calculations presented here, we used 34 polynomials for sufficient convergence. The calculations were done by single-spin flip and tetrahedron updates for typically 2900 MC steps after 700 MC steps of initial relaxation. Both of the updates were done using the standard Metropolis method.

# 8.1.5 Physical Quantities

To identify the ground state magnetic orders in the MC simulation, we calculate the diagonal components of the sublattice-dependent spin structure factor

$$S_{\mathbf{k}}^{(\alpha)} = \frac{1}{N_{t}} \sum_{i,j \in \alpha} \langle \mathbf{S}_{i} \cdot \mathbf{S}_{j} \rangle \exp\left[i\mathbf{k} \cdot (\mathbf{r}_{i} - \mathbf{r}_{j})\right]. \tag{8.2}$$

For simplicity, hereafter in this chapter, we use  $S(\mathbf{k})$  for the diagonal components. We note that the result of  $S_{\mathbf{k}}^{(\alpha)}$  does not depend on  $\alpha$ . In addition to  $S(\mathbf{k})$ , we also calculated the net magnetic moment  $M(\tilde{M})$  and its susceptibility  $\chi(\tilde{\chi})$  for  $S_i(\tilde{S}_i)$ . Also, the local correlations measured by the fraction of two-in two-out,  $\rho_{22}$ , three-in one-out and one-in three-out,  $\rho_{31}$ , and all-in and all-out tetrahedra,  $\rho_{40}$ .

The spin-cluster phase, which is the main finding of this chapter, is detected by  $\lambda$  parameter and its susceptibility  $\chi_{\lambda}$ . Here,  $\lambda$  is defined by

$$\lambda = \frac{1}{2N_{t}} \left( \sum_{p \in P} \sum_{i,j \in p} \tilde{S}_{i} \tilde{S}_{j} - \sum_{q \in Q} \sum_{i,j \in q} \tilde{S}_{i} \tilde{S}_{j} \right), \tag{8.3}$$

where P(Q) is the set of all upward (downward) tetrahedra in the pyrochlore lattice, and the second sum in the first (second) term is taken over all sites in the pth (qth) tetrahedra. This parameter becomes nonzero if the local correlation within each upward and downward tetrahedron becomes inequivalent. Hence, a finite  $\lambda$  implies that spacial-inversion symmetry (SIS) is broken. The specific heat of the model is also calculated by the fluctuation of the internal energy. For the classical spin model, it is given by

$$C = \beta^2 \left( \langle H^2 \rangle - \langle H \rangle^2 \right). \tag{8.4}$$

On the other hand, due to the presence of itinerant electrons, the formula for the DE model is given in the form

$$C = \beta^2 \left( \langle H^2 \rangle - \langle H \rangle^2 + \langle C_e \rangle \right). \tag{8.5}$$

Here,  $\langle C_e \rangle$  is the thermal average of electronic specific heat for a given spin configuration  $\{S_i\}$ ,

$$C_e = \int d\varepsilon \frac{\varepsilon^2 \rho_{\{\mathbf{S}_i\}}(\varepsilon)}{4 \cosh^2[\beta(\varepsilon - \mu)/2]}; \tag{8.6}$$

 $\rho_{\{\mathbf{S}_i\}}(\varepsilon)$  is the one-particle electronic density of states and  $\mu$  is the chemical potential. For the calculation of the spin Hall conductivity,  $\sigma_{\mathrm{H}}^{(\mathrm{s})}$ , we used the Kubo formula

$$\sigma_{\rm H}^{\rm (s)}(\omega) = -\frac{\mathrm{i}}{v_{\rm unit}} \sum_{m,n,\mathbf{k}} \frac{f_{n,\mathbf{k}} - f_{m,\mathbf{k}}}{\varepsilon_{n,\mathbf{k}} - \varepsilon_{m,\mathbf{k}}} \frac{\langle n,\mathbf{k} | j_{z,y}^s | m,\mathbf{k} \rangle \langle m,\mathbf{k} | j_x | n,\mathbf{k} \rangle}{\omega + \varepsilon_{n,\mathbf{k}} - \varepsilon_{m,\mathbf{k}} + \mathrm{i}/\tau}.$$
 (8.7)

<sup>&</sup>lt;sup>1</sup>This parameter is a variant of the bond parameter introduced in Ref. [13].

8.1 Model and Method 107

Here,  $j_{\alpha}^{s}$  is the spin Hall current defined by [16]

$$j_{z,y}^{s} = \frac{1}{2} \left\{ s^{z}, v_{y} \right\}, \tag{8.8}$$

where  $s^z$  is the spin moment along the z direction and  $v_y$  is the verocity for the y direction of the itinerant electrons.  $j_x$  is the charge current operator along the x direction. The  $\varepsilon_{m,\mathbf{k}}$  and  $f_{m,\mathbf{k}}$  is the eigenenergy and corresponding Fermi distribution function for the electronic state in ith band with wave number  $\mathbf{k}$ ,  $|i,\mathbf{k}\rangle$ ,  $\tau$  is the scattering rate, and  $v_{\text{unit}} = 1/\sqrt{2}$  is the volume of the unit cell.

Using these formula,  $\sigma_{\rm H}^{(\rm s)}$  was calculated numerically by taking arithmetic average over 64 different spin configurations randomly generated so that the upward tetrahedra are either all-in or all-out. In the calculation, we assumed  $\tau^{-1}/t=0.01$ , and an electronic field is applied along the [110] direction, and the spin current and magnetic moment are measured along [112] and [111], respectively.

## 8.2 Effective Spin Model

# 8.2.1 $J_1$ - $J_2$ - $J_3$ Ising Model

By using the perturbation theory in Sect. 2.5, we obtain the effective Ising model with long-range and multiple-spin interactions. Among many contributions, for simplicity, we consider only two-spin interactions<sup>2</sup>;

$$H_{\text{eff}} = -J_1 \sum_{\langle i,j \rangle} \tilde{S}_i \tilde{S}_j + J_2 \sum_{\{i,j\}} \tilde{S}_i \tilde{S}_j + J_3 \sum_{[i,j]} \tilde{S}_i \tilde{S}_j.$$
 (8.9)

Here, the estimates of the perturbation for NN, second-neighbor, and third-neighbor couplings gives  $J_1 = -4.19161 \times 10^{-2} + J_{\rm AFM}/3$ ,  $J_2 = 9.65132 \times 10^{-4}$ , and  $J_3 = 9.96332 \times 10^{-4}$ , respectively (see Fig. 8.1a for the definition of interactions). Note that  $J_1$  consists of two contributions: the FM DE interaction and AFM interaction  $J_{\rm AFM}$  (the signs are reversed due to the projection from  $S_i$  to  $\tilde{S}_i$ ).

#### 8.2.2 Monte Carlo Simulation

Figure 8.2 shows the phase diagram obtained by the MC simulation. We identify four dominant regions in addition to the high-T paramagnetic state: (i) the ice state for  $J_1 \leq -0.004$ , (ii) 32-sublattice ordered phase for  $-0.003 \leq J_1 \leq 0$ ,

<sup>&</sup>lt;sup>2</sup>We also evaluated the four-spin interactions, but they are much smaller and subdominant compared to the two-spin interactions. Hence, they are ignored in our calculation.

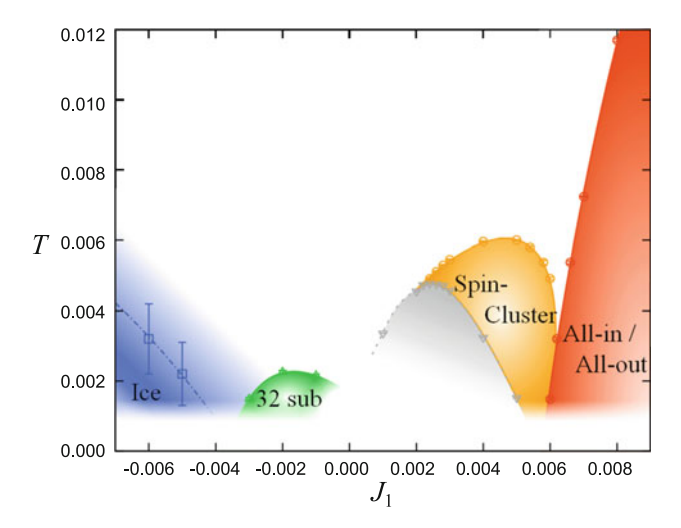


Fig. 8.2 Finite T phase diagram for the effective Ising model in Eq. (8.9). The symbols indicate the critical temperatures (crossovers in the ice region) obtained by MC simulation, and the lines are the guides for eyes

(iii) spin-cluster phase with SIS breaking for  $0.002 \lesssim J_1 \lesssim 0.006$ , and (iv) all-in/all-out ordered phase for  $J_1 \gtrsim 0.006$ . Figure 8.3 shows typical MC data for T dependences of physical quantities used for identifying these four regions.

In the region (i), the FM DE interaction is dominant, which develops the two-in two-out spin configuration in all tetrahedra. This is clearly seen in the local correlations measured by the fraction of two-in two-out,  $\rho_{22}$ , three-in one-out and one-in three-out,  $\rho_{31}$ , and all-in and all-out tetrahedra,  $\rho_{40}$ ; as T decreases,  $\rho_{22}$  grows, while  $\rho_{31}$  and  $\rho_{40}$  are suppressed, as shown in Fig. 8.3a. Correspondingly, the specific heat C shows a hump, similar to that found in the spin ice [4, 12]. This signals a crossover to the ice state, which is plotted in Fig. 8.2.

On the other hand, in the region (iv),  $J_{AFM}$  dominates the FM DE interaction and stabilizes the all-in/all-out order. Figure 8.3e shows a rapid increase of the net magnetic moment for projected spins,  $\tilde{M}$ , and corresponding divergent behavior of its susceptibility  $\tilde{\chi}$ . At the same time, C shows a sharp peak and  $\rho_{40}$  becomes dominant, as shown in Fig. 8.3f. The results indicate the second order transition to the all-in/all-out ordered state; the critical temperature is estimated at  $T_c = 0.01170(4)$  at  $J_1 = 0.008$  from the Binder analysis [2] of  $\tilde{M}$  shown in the inset of Fig. 8.3e.

Between the two regimes, we found interesting phases resulting from competition between the DE interaction and  $J_{AFM}$ . One is the 32-sublattice ordered phase in the region (ii) next to the ice state. Figure 8.3b shows an abrupt increase of the corresponding spin structure factor for the same sublattice,  $S(\mathbf{k})$  at  $\mathbf{k} = (\pi, \pi, \pi)$ , while only small anomalies are seen in  $\rho_{22}$ ,  $\rho_{31}$ , and  $\rho_{40}$ . This is the 32-sublattice order we discussed in Sect. 7.2 (see Fig.7.1c). We note that the phase transition to 32-sublattice order here is apparently of first order while the phase transition in

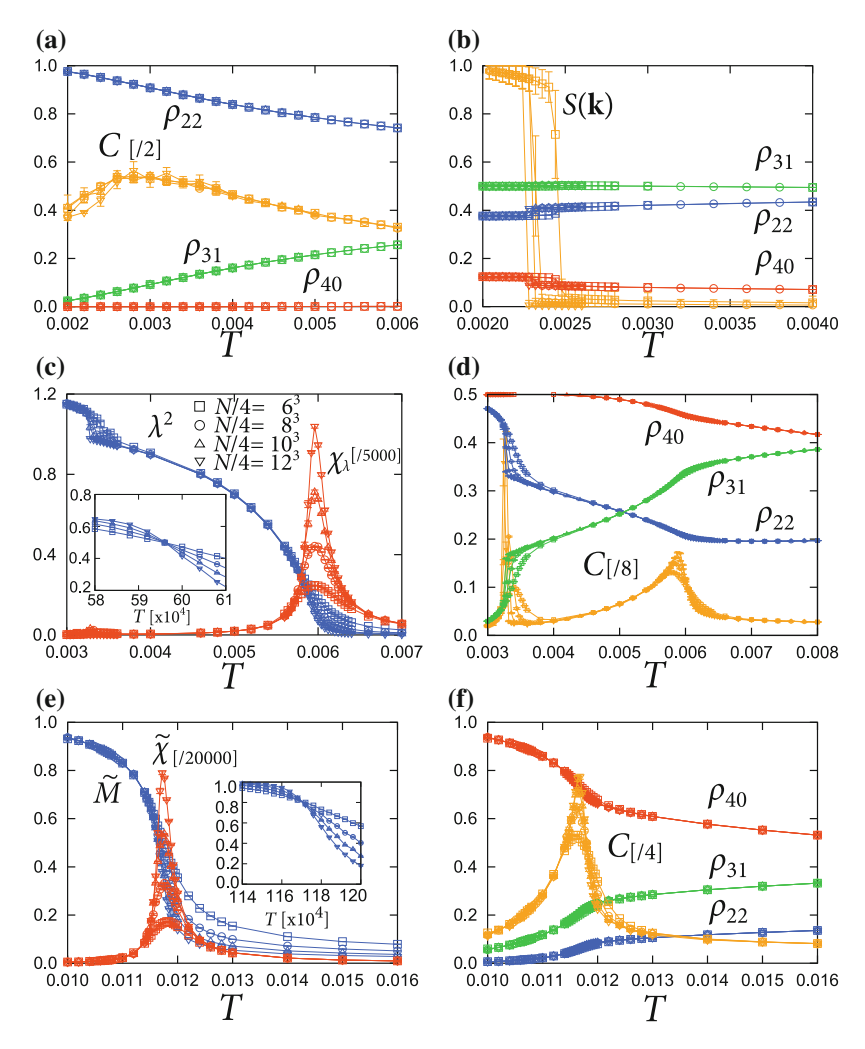


**Fig. 8.3** MC results for the model in Eq. (8.9) at  $\mathbf{a}$   $J_1 = -0.006$ ,  $\mathbf{b}$   $J_1 = -0.002$ ,  $\mathbf{c}$ ,  $\mathbf{d}$   $J_1 = 0.004$ , and  $\mathbf{e}$ ,  $\mathbf{f}$   $J_1 = 0.008$ . See the text for details

Sect. 7.3 appears to be of second order. This is due to the presence of tricritical point, which appears while sweeping the ratio  $J_2/J_3$ . By the MC calculation with sweeping  $J_2/J_3$ , in the region  $J_2/J_3 \ll 1$ , we confirmed that the transition to 32-sublattice order is of second order. On the other hand, the order of transition changes from second order to first order with increasing  $J_2/J_3 \rightarrow 1$ . In the phase diagram in Fig. 8.2, the transition temperature is estimated from the size extrapolation of the abrupt jump of  $S(\mathbf{k})$ .

Another interesting phase is found in the region (iii) on the verge of the all-in/all-out order. Figure 8.3c shows the result for  $\lambda$  parameter and its susceptibility  $\chi_{\lambda}$ . The

result indicates that the upward and downward tetrahedra become inequivalent at low T; one of them has larger population of the all-in/all-out tetrahedra than the other (see Fig. 8.1a). In other words, four-spin clusters are formed and arranged periodically (the translational symmetry is not broken as the primitive unit cell includes a pair of upward and downward tetrahedra). The transition is continuous and the critical temperature is estimated at  $T_c = 0.00596(4)$  at  $J_1 = 0.004$ , from the Binder analysis in the inset. The specific heat plotted in Fig. 8.3d also shows an anomaly at  $T_c$ . Interestingly, the phase below  $T_c$  does not show any magnetic ordering; no singularity is found in  $S(\mathbf{k})$ . Therefore, in this phase, TRS is preserved but SIS is broken due to the differentiation of upward and downward tetrahedra.

# 8.2.3 Emergent Frustration Induced by Further Neighbor Interactions

The spin-cluster phase in region (iii) appears only at finite T, as depicted in Fig. 8.2; the system exhibits another transition at a lower T (see also Fig. 8.3d). This suggests that the spin-cluster phase is a thermally-induced intermediate phase. Such intermediate phase is often found in geometrically frustrated systems, as we discussed some examples in Chaps. 3 and 5. To see the frustration effect more explicitly, let us rewrite the model in Eq. (8.9) into a magnetic charge model,

$$H_{\text{eff}} = J_2 \sum_{\langle p,q \rangle} Q_p Q_q - \frac{\tilde{J}_1}{2} \sum_p Q_p^2 + \text{const.},$$
 (8.10)

defined on a diamond lattice composed of the centers of tetrahedra in the pyrochlore lattice (see Fig. 8.1b). Here,  $\tilde{J}_1 = J_1/2 + J_2$  (we take  $J_2 = J_3$  for simplicity) and  $Q_p = \sum_{i \in p} \tilde{S}_i$  is the magnetic charge at pth site on the diamond lattice, defined by the sum of four projected spins belonging to pth tetrahedron in the pyrochlore lattice. In the MC simulation, below  $T_c$ , either upward or downward tetrahedra are dominated by all-in/all-out configurations. Furthermore, at lower T, the remaining ones become dominantly two-in two-out, as seen for  $T \lesssim 0.00324$  in Fig. 8.3d. Hence, the situation is approximately viewed as the magnetic charge with  $Q_p = \pm 4$  bridged by  $Q_p = 0$  on the diamond lattice, as shown in Fig. 8.1b. This is effectively an Ising model on a face-centered-cubic (FCC) lattice. The system, therefore, hinders severe frustration in the superlattice of tetrahedra, which presumably leads to the emergence of the spin-cluster phase (iii).

<sup>&</sup>lt;sup>3</sup>The indices p and q run both upward and downward tetrahedra; hence, there is a local constraint for neighboring  $Q_p$  and  $Q_q$ , as they share  $\tilde{S}_i$  in between them.

<sup>&</sup>lt;sup>4</sup>The transition at  $T \simeq 0.00324$  might be ascribed to a dimensional reduction similar to that in the FCC Ising model [6].

## 8.3 Monte Carlo Study of the Double-Exchange Model

In Sect. 8.2, by considering the effective Ising model for the DE model in Eq. (8.1), we discussed the emergence of an intermediate spin-cluster phase with broken SIS. In this section, we investigate whether the broken SIS state appears in the original DE model by using PEMC and directly conducting the MC simulation for the itinerant model. We show that, indeed, the intermediate state appears in the DE model at a particular range of  $J_{\text{AFM}}$  and T.

Figures 8.4a, b show the MC results at  $J_{AFM}=0.18$ . The increase of  $\lambda$ , and the peaks of  $\chi_{\lambda}$  and C at  $T\sim0.053$ , along with absence of anomaly in  $S(\mathbf{k})$ , indicate the emergence of a SIS-broken spin-cluster phase, similar to that in Figs. 8.3c, d. On the other hand,  $S(\mathbf{k})$  at  $\mathbf{k}=(0,0,2\pi)$  sharply increases at a lower T associated with a sharp peak in C. The extrapolation with respect to 1/N of these transition temperatures (peaks of  $\chi_{\lambda}$  and C) is presented in Fig. 8.5. The results show that the model in Eq. (8.1) exhibits two successive transitions: one is the transition to the spin-cluster state with SIS breaking at  $T_{C}=0.051(1)$ , and the other is the magnetic transition with TRS breaking at  $T_{N}=0.032(1)$ . The estimate of  $T_{C}$  and  $T_{N}$  are obtained from extrapolation as shown in Fig. 8.5.

The lowest T phase is an AFM planer type magnetic LRO. In the ground state, the tetrahedra that belong to the lattice points in the first  $\langle 100 \rangle$  layer are in all-out configuration. On the other hand, the tetrahedra in the second  $\langle 100 \rangle$  layer are all-in. The spin pattern of the ground state consists of alternating stacking of these two  $\langle 100 \rangle$  layers. While the transition at  $T_N$  is seen clearly in the result of PEMC simulation, such a transition was not captured in the effective Ising model, as shown in Fig. 8.2. The result suggests that the interactions beyond the effective model in Eq. (8.9) lift the degeneracy in the FCC pseudospin model. Indeed, the result of density of states (DOS) for itinerant electrons in this LRO show that this magnetic phase below  $T_N$  is an insulator. This result appears to show that a Slater-like mechanism takes dominant

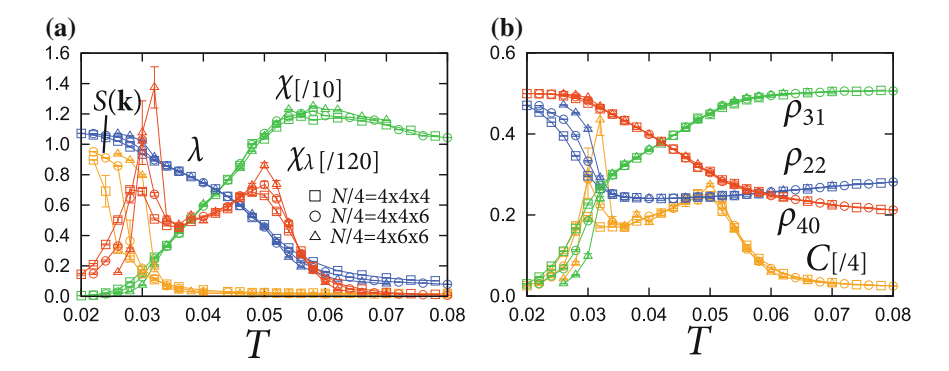
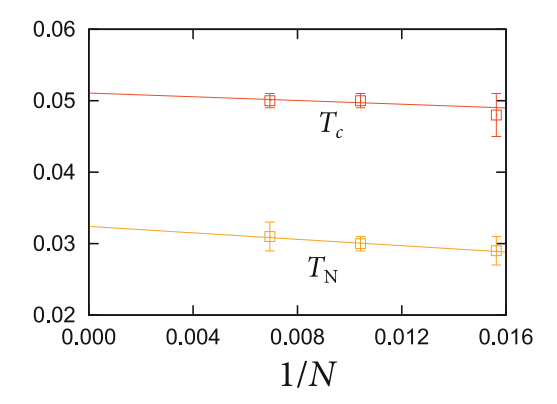


**Fig. 8.4** MC results for the DE model in Eq. (8.1) at n=1/4 and  $J_{AFM}=0.18$ . **a** The results for  $\chi$ ,  $\lambda$ ,  $\chi_{\lambda}$ , and  $S(\mathbf{k}=(0,0,2\pi))$ , and **b**  $\rho_{22}$ ,  $\rho_{31}$ ,  $\rho_{40}$ , and C

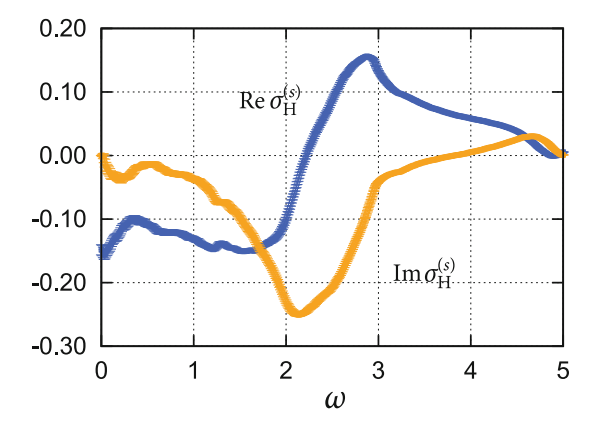
Fig. 8.5 System-size extrapolation of critical temperatures estimated by the two peaks of  $\chi_{\lambda}$  for the DE model in Eq. (8.1) at n = 1/4 and  $J_{AFM} = 0.18$ 



role in selecting the LRO. As our perturbation theory takes the free electron state with renormalized hopping as the non-perturbative Hamiltonian, it is expected that such an effect is neglected in this approximation.

On the other hand, the phase transition to spin-cluster state is well reproduced in the DE model. An interesting feature of this phase is that, though the transition at  $T_c$  is not a magnetic one, the magnetic susceptibility  $\chi$  for the Ising spins,  $\chi$ , shows a steep decrease below  $T_c$ , in addition to a kink anomaly at  $T_N$ , as shown in Fig. 8.4a. This is in sharp contrast to a usual AFM phase transition, which shows a maxima at a temperature at or slightly higher than the magnetic transition temperature. The hump in the magnetic susceptibility is a consequence of the formation of the all-in/all-out spin clusters, which have no magnetic moments for each clusters. In the ideal case of the intermediate state, where all the upward tetrahedra are fluctuating between all-in or all-out, the net magnetic moment of the system are exactly zero as each of the spins belong to a cluster.

Fig. 8.6 Spin Hall conductivity calculated by taking simple average in the SIS-broken spin-cluster manifold



# 8.4 Spin Hall Effect

An interesting point of the intermediate phase is that it exhibits finite spin Hall conductivity. As the evaluation of the spin Hall conductivity using the MC method is numerically tough, we here calculated the spin Hall conductivity by assuming an ideal situation, i.e., by taking simple average over 64 different spin configurations randomly generated so that the upward tetrahedra are either all-in or all-out. Further details on the calculation of spin Hall conductivity  $\sigma_{\rm H}^{(s)}$  is given in Sect. 8.1.5.

Figure 8.6 shows the result of  $\sigma_{\rm H}^{(s)}$  calculated by the Kubo formula Eq. (8.7) with finite frequency  $\omega$ . The results shows that the real part of  $\sigma_{\rm H}^{(s)}(\omega)$  remains finite at  $\omega \to 0$ . This suggests that the intermediate spin-cluster phase show spin Hall effect. The present SHE is one of the consequences of characteristic noncoplanar spin textures [7, 10, 18], which is distinct from the conventional SHE originating from the relativistic SOI.

We note that, it was recently pointed out that, the vertex correction gives significant effects on the spin Hall conductivity; in some cases, the vertex correction completely cancels out the finite  $\sigma_{\rm H}^{(s)}$  obtained by the standard Kubo formula [5]. Also, compared to the charge currents, the definition of  $j_{\alpha}^{s}$  remains somewhat ambiguous. Again, this also has a significant effect on  $\sigma_{\rm H}^{(s)}$ . Hence, our result suggests possible emergence of SHE, but further investigation using more sophisticated calculation techniques is desirable.

# 8.5 Discussion and Summary

To summarize, in this chapter, we studied the phase diagram of the spin-ice double-exchange model using the effective spin model. By using a classical Monte Carlo method, we mapped out the phase diagram of the effective spin model with varying nearest-neighbor interaction, and found a new intermediate phase with broken spatial inversion symmetry. By using the polynomial expansion Monte Carlo method, we also confirmed that the intermediate phase emerges in the original double-exchange model. In addition, we found that the intermediate phase exhibits the spin Hall effect.

The SIS breaking in our model in Eq. (8.1) takes place by formation of four-spin clusters. Cluster formation is a manifestation of competing interactions in frustrated itinerant electron systems [14, 15]. Our SIS-broken phase, however, retains neither charge ordering nor magnetic dipole ordering, suggesting that it is characterized by higher-order electric and magnetic multipoles. Hence, our results indicate that the scattering of electrons by such multipoles can lead to unconventional transport phenomena. Multipole orders, which are often called "hidden orders", have attracted interests not only in localized spin systems but also in conducting systems [9]. SHE may provide a further insight into such hidden multipoles.

As mentioned above, our model is simple but includes some essential features in metallic pyrochlore oxides, which have recently attracted growing interest both experimentally and theoretically [3]. It is intriguing that some pyrochlore compounds indeed exhibit similar SIS breaking accompanied by a breathing-type lattice distortion [11, 17].

#### References

- 1. P.W. Anderson, H. Hasegawa, Phys. Rev. 100, 675 (1955)
- 2. K. Binder, Z. Phys, B 43, 119 (1981)
- 3. J.S. Gardner, M.J.P. Gingras, J.E. Greedan, Rev. Mod. Phys. 82, 53 (2010)
- M.J. Harris, S.T. Bramwell, D.F. McMorrow, T. Zeiske, K.W. Godfrey, Phys. Rev. Lett. 79, 2554 (1997)
- 5. J. Inoue, G.E.W. Bauer, L.W. Molenkamp, Phys. Rev. B 70, 041303(R) (2004)
- 6. J.L. Lebowitz, M.K. Phani, D.F. Styer, J. Stat. Phys. 38, 413 (1985)
- 7. D. Loss, P.M. Goldbart, Phys. Rev. B **45**, 13544 (1992)
- 8. Y. Motome, N. Furukawa, J. Phys. Soc. Jpn. 68, 3853 (1999)
- J.A. Mydosh, P.M. Oppeneer, Rev. Mod. Phys. 83, 1301 (2011)
   K. Ohgushi, S. Murakami, N. Nagaosa, Phys. Rev. B 62, 6065(R) (2000)
- K. Ohgushi, J. Yamaura, M. Ichihara, Y. Kiuchi, T. Tayama, T. Sakakibara, H. Gotou, T. Yagi, Y. Ueda, Phys. Rev. B 83, 125103 (2011)
- A.P. Ramirez, A. Hayashi, R.J. Cava, R. Siddharthan, B.S. Shastry, Nature (London) 399, 333 (1999)
- 13. N. Shannon, K. Penc, Y. Motome, Phys. Rev. B 81, 184409 (2010)
- 14. Y. Shimomura, S. Miyahara, N. Furukawa, J. Phys. Soc. Jpn. **73**, 1623 (2004)
- 15. Y. Shimomura, S. Miyahara, N. Furukawa, J. Phys. Soc. Jpn. 74, 661 (2005)
- J. Sinova, D. Culcer, Q. Niu, N.A. Sinitsyn, T. Jungwirth, A.H. MacDonald, Phys. Rev. Lett. 92, 126603 (2004)
- 17. J. Yamaura, Z. Hiroi, J. Phys. Soc. Jpn. **71**, 92598 (2002)
- J. Ye, Y.B. Kim, A.J. Millis, B.I. Shraiman, P. Majumdar, Z. Tešanovic, Phys. Rev. Lett. 83, 3737 (1999)
- 19. C. Zener, Phys. Rev. 82, 403 (1951)

# Chapter 9 Benchmark of the Polynomial Expansion Monte Carlo Method

**Abstract** In this section, we present the benchmark of the polynomial expansion Monte Carlo method to a Kondo lattice model with classical localized moments on a geometrically frustrated lattice. We apply the method to the model in Eq. (7.1) introduced in Sect. 7.1.1, the spin-ice type Ising-spin Kondo lattice model on a three-dimensional pyrochlore lattice, and examine the convergence in terms of the order of polynomials and the truncation distance. We find that, in a wide range of electron density at a relatively weak Kondo coupling compared to the noninteracting bandwidth, the results by the polynomial expansion method show good convergence to those by the conventional method within reasonable numbers of polynomials. On the other hand, we also show that the real-space truncation is not helpful in reducing the calculation amount for the system sizes that we reached, as the sufficient convergence is obtained when most of the sites are involved within the truncation distance.

#### 9.1 Model and Parameters

In this section, we briefly restate the model and parameters we used for the benchmark.

# 9.1.1 Spin-Ice Kondo Lattice Model

We consider a Kondo lattice model with Ising spins on a pyrochlore lattice (the Hamiltonian studied in Chap. 7). The Hamiltonian is given by

$$H = -t \sum_{\langle i,j \rangle,\sigma} (c_{i\sigma}^{\dagger} c_{j\sigma} + \text{H.c.}) - J \sum_{i} \mathbf{S}_{i} \cdot \boldsymbol{\sigma}_{i}.$$
 (9.1)

The first term represents hopping of itinerant electrons, where  $c_{i\sigma}$  ( $c_{i\sigma}^{\dagger}$ ) is the annihilation (creation) operator of an itinerant electron with spin  $\sigma = \uparrow$ ,  $\downarrow$  at ith site, and t is the transfer integral. The sum  $\langle i,j \rangle$  is taken over nearest-neighbor sites on the

pyrochlore lattice, which consists of a three-dimensional network of corner-sharing tetrahedra. The second term is the onsite interaction between itinerant electron spins.

$$\sigma_i = \sum_{\alpha,\beta} c_{i\alpha}^{\dagger} \tau_{\alpha\beta} c_{i\beta}, \tag{9.2}$$

 $(\tau_{\alpha\beta}$  is the vector of  $\alpha\beta$  components of the Pauli matrices) and localized Ising moments  $\mathbf{S}_i$  ( $|\mathbf{S}_i|=1$ ), and J is the coupling constant. The anisotropy axis of Ising moments is given along the local [111] direction, i.e., along the line connecting the centers of two tetrahedra which the spin belongs to (see Fig. 7.1 in Chap. 7).

As this section is intended to be a presentation of the benchmark for Chap. 7, we particularly focus on the relatively low electron density region of 0 < n < 0.35 at a weak spin-charge coupling (J = 2t). The electron density is defined by

$$n = \frac{1}{2N} \sum_{i\sigma} \langle c_{i\sigma}^{\dagger} c_{i\sigma} \rangle, \tag{9.3}$$

where N is the number of sites. Hereafter, we set the unit of energy t = 1, the lattice constant of the cubic unit cell a = 1, and the Boltzmann constant  $k_B = 1$ .

## 9.1.2 Details of the Calculation and Physical Quantities

The polynomial expansion Monte Carlo method (PEMC) is a controlled approximation in the sense that the results converge to the results by the conventional Monte Carlo method based on the exact diagonalization (EDMC) by increasing the polynomials and truncation length. In the following sections, we present the benchmark results for the convergence by changing the total number of polynomials  $m_{\text{tot}}$  and the truncation distance d. We investigate the convergence using system sizes up to  $N=4\times8^3$ , with electron fillings that corresponds to different ground states studied in Chap. 7 and various temperatures, both above and below transition. For small system size,  $N=4\times4^3$ , we also present comparison of the PEMC results with EDMC. For the results presented in this chapter, we typically performed 3000 MC measurements after 500 MC steps of thermalization.

The convergence of calculation is investigated by the convergence of physical quantities calculated by MC simulation. In this chapter, we measure two types of physical quantities which characterize the long-range ordering and short-range correlations, respectively. These quantities were used in Chap. 7 to clarify the phase diagram of the Kondo lattice model in Eq. (9.1).

9.1 Model and Parameters 117

For the long-range ordering, we calculate the sublattice magnetization

$$M_{\mathbf{q}} = \left[ \frac{4}{N} S^{\alpha \alpha}(\mathbf{q}) \right]^{1/2}, \tag{9.4}$$

where  $S^{\alpha\alpha}(\mathbf{q})$  is the  $\alpha$ th diagonal component of the spin structure factor

$$S^{\alpha\beta}(\mathbf{q}) = \frac{1}{N} \sum_{n,l} \langle \mathbf{S}_n^{\alpha} \cdot \mathbf{S}_l^{\beta} \rangle \exp[i\mathbf{q} \cdot (\mathbf{r}_n^{\alpha} - \mathbf{r}_l^{\beta})]. \tag{9.5}$$

Here,  $\mathbf{S}_n^{\alpha}$  is the classical Ising spin at  $\alpha$ th sublattice site in nth unit cell, and  $\mathbf{r}_n^{\alpha}$  is the position vector of the Ising spin  $\mathbf{S}_n^{\alpha}$ . In the calculations below, we present the results for three magnetic phases: ice-ferro, 32-sublattice, and all-in/all-out order (see Fig. 7.1). The characteristic wave number  $\mathbf{q}$  for these phases are given by  $\mathbf{q}=(0,0,0)$  for the ice-ferro and all-in/all-out orders, and  $\mathbf{q}=(\pi,\pi,\pi)$  for the 32-sublattice order. For these three orders, the diagonal component of the structure factor  $S^{\alpha\alpha}(\mathbf{q})$  does not depend on  $\alpha$ . Hence, we show the results for the sublattice  $\alpha=1$ .

In addition to the sublattice magnetization, we also measure local correlation parameters  $P_{22}$ ,  $P_{31}$ , and  $P_{40}$ . These parameters are defined by the probabilities of a tetrahedron to be in two-out configuration, three-in one-out or one-in three-out configuration, and all-in or all-out configuration, respectively. In Chap. 7, the magnetic ordering pattern is determined by these local correlation parameters in addition to the spin structure factor.

# 9.2 Temperature Dependence

To gain an overview on how PEMC works, we first show T dependence of the sublattice magnetization  $M_{\bf q}$  in the ice-ferro, 32-sublattice, and all-in/all-out ordered regions. In Chap. 7, we argued that four dominant magnetic phases arise in the electron density  $n \lesssim 0.3$ : ice-ferro, ice- $(0,0,2\pi)$ , 32-sublattice, and all-in/all-out. We, however, omit the results for the ice- $(0,0,2\pi)$  phase as PEMC shows extremely slow convergence in terms of the number of polynomials  $m_{\rm tot}$ . The data in this section were calculated for  $N=4\times4^3$  sites with truncation distance d=6. As we show later, the deviation due to the truncation is sufficiently small for d=6.

Figure 9.1a shows T dependence of  $M_{\bf q}$  calculated by PEMC at  $\mu=-5.9$  in comparison with the EDMC result. The electron density is almost T independent at n=0.030(2). In this very low density region, the ice-ferro order develops at low T (see Chap. 7). The PEMC results are shown by the open symbols, while the EDMC results are shown by crosses connected by the solid line. All the results show a rapid increase of  $M_{\bf q}$  as T decreases, signaling the phase transition to the ice-ferro phase.

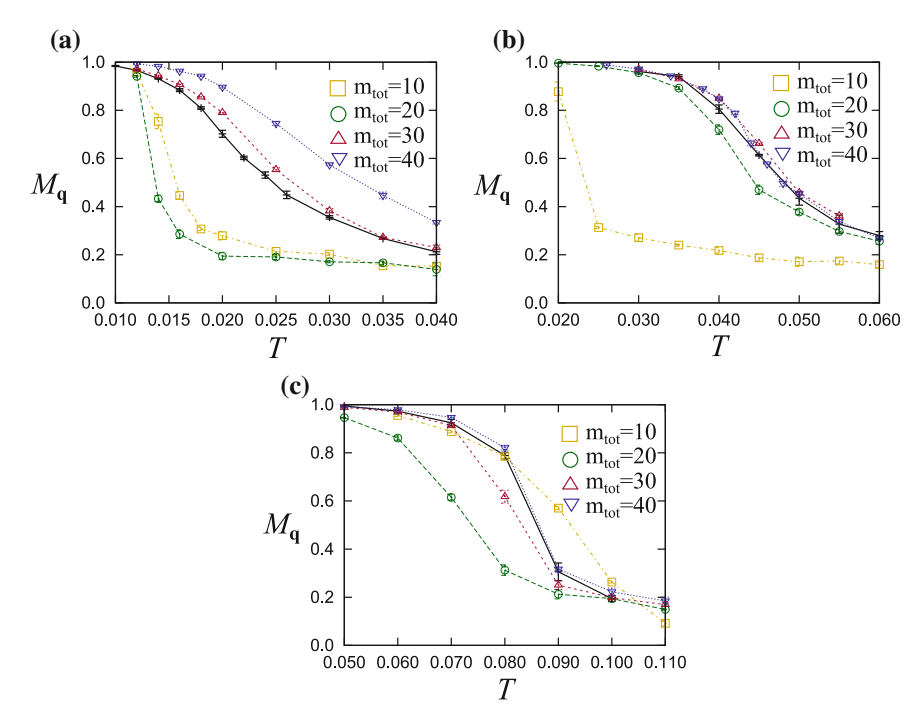


**Fig. 9.1** *T* dependence of  $M_{\bf q}$  calculated by PEMC at  ${\bf a}~\mu=-5.9~[n=0.030(2)]$ ,  ${\bf b}~\mu=-3.7~[n=0.180(5)]$ , and  ${\bf c}~\mu=-1.3~[n=0.348(6)]$ . The wave number  ${\bf q}$  is  ${\bf q}=(0,0,0)$  for ( ${\bf a}$ ) and ( ${\bf c}$ ), and  ${\bf q}=(\pi,\pi,\pi)$  for ( ${\bf b}$ ). Different symbols correspond to the results of MC simulation with different numbers of polynomials. Crosses with *solid lines* show the results by EDMC. The PEMC calculations are done with d=6 for  $4\times4^3$  site systems

However, the PEMC results show slow convergence to the EDMC ones; even the results for  $m_{\text{tot}} = 40$  show considerable deviations.

On the other hand, for higher electron densities, the PEMC results show good convergence to the EDMC results. Figures 9.1b, c show the results at  $\mu = -3.7$  and  $\mu = -1.3$ , respectively. For the result at  $\mu = -3.7$  in Fig. 9.1b, the 32-sublattice order develops at low-T. As shown in Fig. 9.1b, the results for  $m_{\text{tot}} = 10$  and 20 show considerable deviations from the EDMC results. On the other hand, the results for  $m_{\text{tot}} = 30$  and 40 show good agreement except for a slight deviation around the critical point [the critical temperature is estimated as  $T_c = 0.043(2)$  from the inflection point of the T dependence of  $M_{\bf q}$  (see Chap. 7 for further details)].

A similar result was obtained for  $\mu = -1.3$ . At this chemical potential, the all-in/all-out order develops at the low temperature. The result in Fig. 9.1c shows that  $m_{\rm tot} = 30$  and 40 appear to be sufficient for the convergence except for the region close to  $T_c = 0.085(5)$ , whereas the results for smaller  $m_{\rm tot}$  are oscillating in terms of  $m_{\rm tot}$ .

These results indicate that the PEMC results show sufficient convergence for  $m_{\text{tot}} \gtrsim 30$  in the relatively high density region of  $n \gtrsim 0.15$ . The results away from the critical point converge faster than those close to the critical point. These aspects are further discussed in the following sections.

## 9.3 Convergence in the Number of Polynomials

We next investigate the convergence of PEMC with respect to  $m_{\text{tot}}$  in the three density regions shown in Figs. 9.1a–c, respectively, for  $N=4\times4^3$ . We here show the convergence in three different T regions: a low-T ordered region, high-T paramagnetic region, and in the vicinity of the critical temperature. The critical temperatures for  $\mu=-5.7, -3.7, \text{ and } -1.3$  are estimated to be  $T_c=0.023(2), 0.043(2), \text{ and } 0.085(5)$ , respectively, from the inflection point of the T dependence of  $M_0$ .

Figure 9.2 shows the results for  $\mu = -5.7$  (ice-ferro ordered region) at T = 0.012, 0.020, and 0.030, corresponding to the ordered phase, close to critical point, and paramagnetic regions, respectively. Figure 9.2a is the result for  $M_{\bf q}$ , and Figs. 9.2b–d

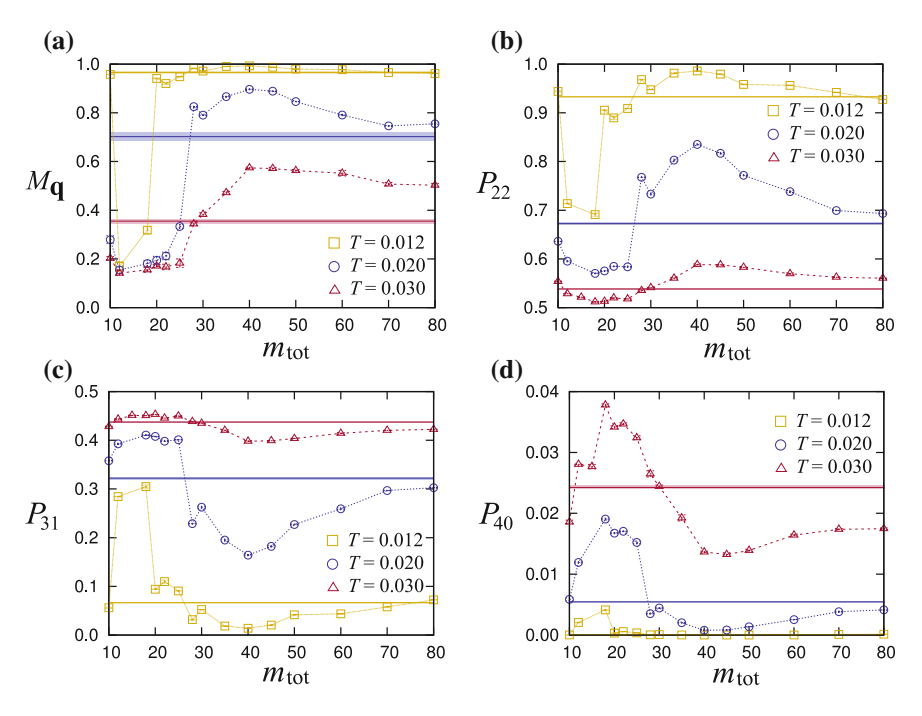
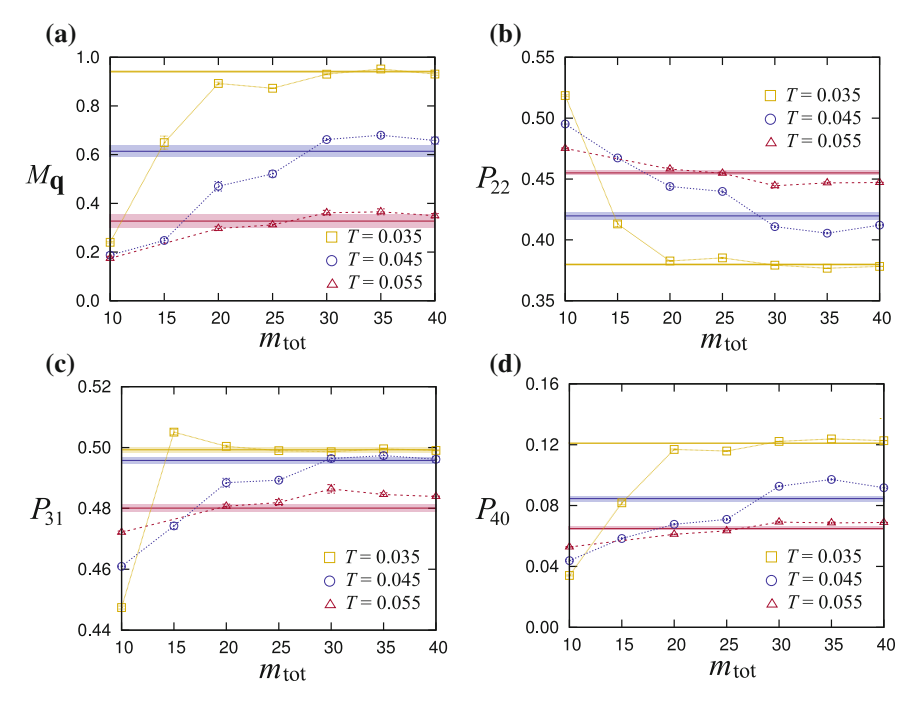


Fig. 9.2 PEMC results for  $m_{\text{tot}}$  dependence of **a**  $M_{\mathbf{q}}$ , **b**  $P_{22}$ , **c**  $P_{31}$ , and **d**  $P_{40}$ . The calculations are done for  $N=4\times4^3$  and  $\mu=-5.7$  with d=6. For comparison, the results and statistical errors by EDMC are shown by *horizontal solid lines* and *shades*, respectively



**Fig. 9.3** PEMC results for  $m_{\text{tot}}$  dependence of **a**  $M_{\mathbf{q}}$ , **b**  $P_{22}$ , **c**  $P_{31}$ , and **d**  $P_{40}$ . The calculations are done for  $N=4\times4^3$  and  $\mu=-3.7$  with d=6. For comparison, the results and statistical errors by EDMC are shown by *horizontal solid lines* and *shades*, respectively

are the results for the local correlation parameters  $P_{22}$ ,  $P_{31}$ , and  $P_{40}$ , respectively. The EDMC results are indicated by horizontal solid lines and the shades show statistical errors. In all T regions, the convergence of PEMC results to the EDMC ones is slow;  $m_{\text{tot}} \gtrsim 80$  appears to be necessary for sufficient convergence.

On the other hand, the PEMC results at  $\mu=-3.7$  show better convergence. The results are shown in Fig. 9.3. Both the sublattice magnetization and the local correlation parameters show reasonable convergence for  $m_{\rm tot}\gtrsim 30$ . The situation is similar for  $\mu=-1.3$  (the all-in/all-out ordered region), as shown in Fig. 9.4; the results show good convergence for  $m_{\rm tot}\gtrsim 35$ . In both cases with  $\mu=-3.7$  and -1.3, the data close to critical temperature appear to show relatively slower convergence compared to the low-T and high-T region, but the remnant deviation is in a reasonable range and not harmful to the estimation of the critical temperature.

The results in Figs. 9.3 and 9.4 indicate that PEMC works efficiently in a wide range of T for the relatively high electron density of  $n \gtrsim 0.15$ . Typically,

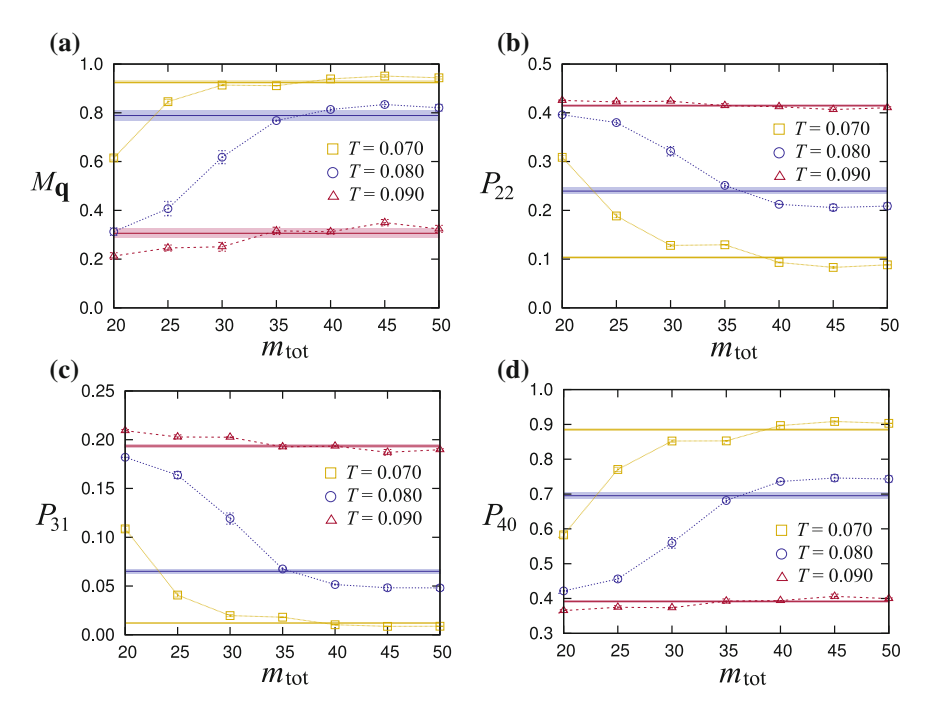


**Fig. 9.4** PEMC results for  $m_{\text{tot}}$  dependence of **a**  $M_{\mathbf{q}}$ , **b**  $P_{22}$ , **c**  $P_{31}$ , and **d**  $P_{40}$ . The calculations are done for  $N=4\times4^3$  and  $\mu=-1.3$  with d=6. For comparison, the results and statistical errors by EDMC are shown by *horizontal solid lines* and *shades*, respectively

 $m_{\rm tot} = 30$ –40 is sufficient for the convergence. On the other hand, in the lower electron density region, quantitatively sufficient convergence requires much larger  $m_{\rm tot}$ . These points are discussed in Sect. 9.6.

# **9.4** Convergence in the Truncation Distance

Next, we investigate the convergence with respect to the real-space truncation distance d. Here, the calculations are done at  $\mu = -3.7$  and -1.3 with  $m_{\text{tot}} = 40$ , for which PEMC results show good convergence to the EDMC ones as discussed in the previous section. The system size considered here is  $N = 4 \times 4^3$ ; the Manhattan distance to the furthest site is d = 8.

Figure 9.5 shows the PEMC results in the 32-sublattice ordered region at  $\mu=-3.7$  for different temperatures,  $T=0.035,\,0.045,\,$  and 0.055, which correspond to the magnetically ordered phase, in the vicinity of critical point, and paramagnetic phase, respectively. In all T regions, the PEMC data converge to the EDMC ones for  $d\gtrsim 6$ , except for the data at T=0.045 in the one close to critical temperature. This shows again that the convergence becomes slower around the critical point.

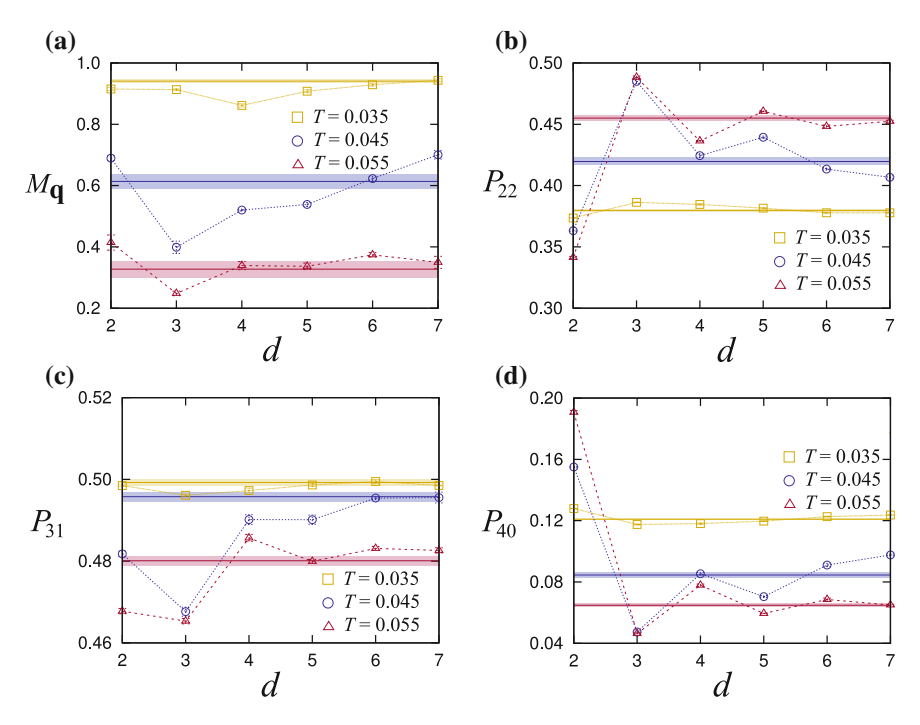


**Fig. 9.5** PEMC results for d dependence of **a**  $M_{\mathbf{q}}$ , **b**  $P_{22}$ , **c**  $P_{31}$ , and **d**  $P_{40}$ . The calculations are done for  $N=4\times4^3$  and  $\mu=-3.7$  with  $m_{\text{tot}}=40$ . For comparison, the results and statistical errors by EDMC are shown by *horizontal solid lines* and *shades*, respectively

The situation is similar in the all-in/all-out region. Figure 9.6 shows the results for  $\mu=-1.3$  at  $T=0.070,\,0.080,\,$  and 0.090. The results for  $M_{\bf q}$  in Fig. 9.6a show good convergence for  $d\gtrsim 5$  for all T shown. For  $P_{22},\,P_{31},\,$  and  $P_{40}$  in Figs. 9.6b–d, the results at T=0.070 and 0.090 also show well converged results for  $d\gtrsim 5$ . On the other hand, the data at T=0.080 show a slight deviation from EDMC data up to  $d\simeq 7$ .

From the above results, it appears that the truncation with  $d \gtrsim 6$  gives sufficient convergence in a wide range of T and n. In this system size  $N=4\times4^3$ , d=6 already covers a large part of the lattice sites, and hence, the truncation is less useful to the reduction of the calculation amount. It is, however, expected from the truncation algorithm that the necessary truncation distance for the same accuracy does not depend so much on the system size. Hence, the truncation may be efficient for larger system sizes. We examine this point in the next section.

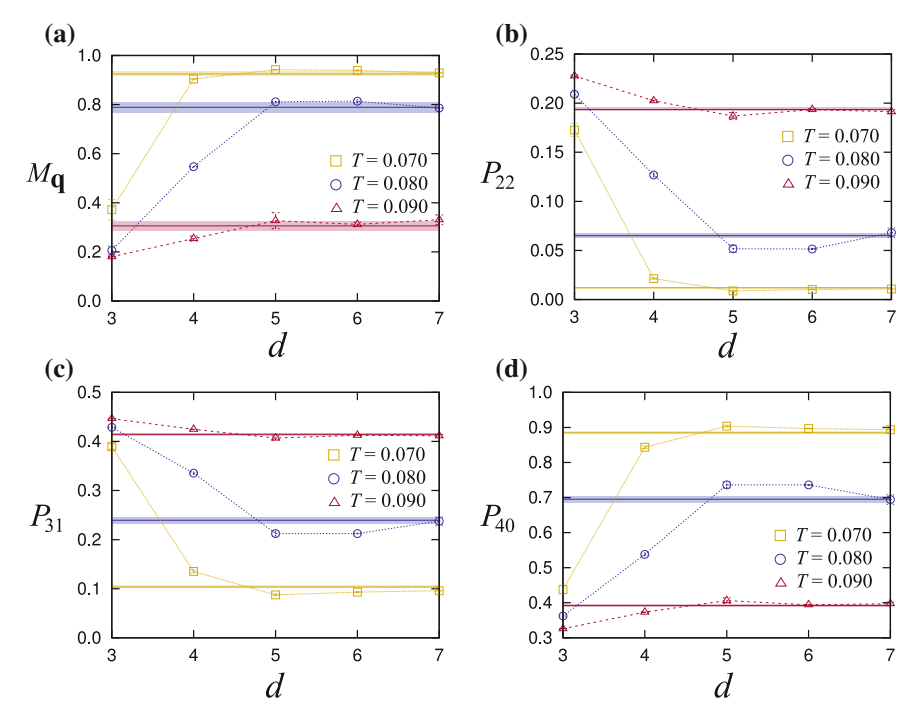


**Fig. 9.6** PEMC results for d dependence of **a**  $M_{\mathbf{q}}$ , **b**  $P_{22}$ , **c**  $P_{31}$ , and **d**  $P_{40}$ . The calculations are done for  $N=4\times4^3$  and  $\mu=-1.3$  with  $m_{\text{tot}}=40$ . For comparison, the results and statistical errors by EDMC are shown by *horizontal solid lines* and *shades*, respectively

# **9.5** Convergence in the Truncation Distance for Larger Systems

To confirm the efficiency of the truncation in larger system sizes, here we conduct the PEMC calculations for  $N=4\times6^3$  and  $4\times8^3$  in the 32-sublattice ordered region. For these system sizes, as EDMC is inapplicable due to the large calculation amount, we perform only PEMC and check the convergence with respect to the truncation distance d. In these sizes, the Manhattan distance to the farthest site is d=12 for  $N=4\times6^3$  and d=16 for  $N=4\times8^3$ .

Figure 9.7 shows the results in the 32-sublattice ordered region at  $\mu = -3.4$  [n = 0.195(1)] for  $N = 4 \times 6^3$ . Here, we take  $m_{\rm tot} = 40$ , as the necessary  $m_{\rm tot}$  for the convergence is expected to be less dependent on the system sizes [2, 3]. As shown in Fig. 9.7a, for  $d \gtrsim 8$ , the results for  $M_{\bf q}$  show reasonable convergence to the results without truncation in all T regions. The results for  $P_{22}$ ,  $P_{31}$ , and  $P_{40}$  also show convergence with  $d \gtrsim 8$ , as shown in Figs. 9.7b–d. Similar behavior is

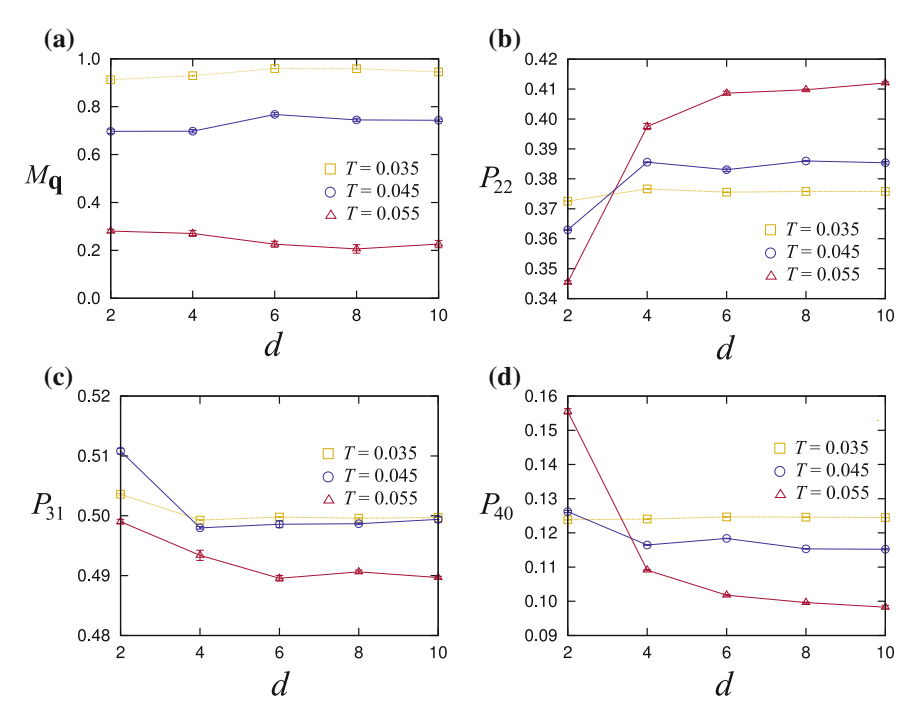


**Fig. 9.7** PEMC results for *d* dependence of **a**  $M_{\bf q}$ , **b**  $P_{22}$ , **c**  $P_{31}$ , and **d**  $P_{40}$ . The calculations are done for  $N=4\times6^3$  and  $\mu=-3.4$  with  $m_{\rm tot}=40$ 

also observed for  $N=4\times8^3$ . Figure 9.8 shows the results for  $N=4\times8^3$  with T=0.035, 0.045, and 0.055. All the results also show good convergence for  $d\gtrsim8$ .

#### 9.6 Discussion

In the previous studies using PEMC, the number of polynomials for well converged calculations was typically  $30 \lesssim m_{\rm tot} \lesssim 40$  [1, 3–6]. Our results presented at  $\mu = -3.7$  and -1.3 in Sects. 9.2 and 9.3 indicate that good convergence is reached for a similar range of  $m_{\rm tot}$ . This shows that PEMC is also an efficient approach even in the presence of severe geometrical frustration. We note that the range of chemical potential  $\mu$  corresponds to a moderate electron density  $n \gtrsim 0.15$ . Considering the fact that most of the previous studies were conducted in the region for  $0.20 \lesssim n \lesssim 0.80$  [1, 3–6], this also supports the applicability of PEMC in the frustrated models in the similar density region.

On the other hand, our results in the lower electron density region show much slower convergence, and even the results for  $m_{\text{tot}} = 80$  show considerable deviations from the EDMC results, as shown in Fig. 9.2. This might be owing to the fact that

9.6 Discussion 125

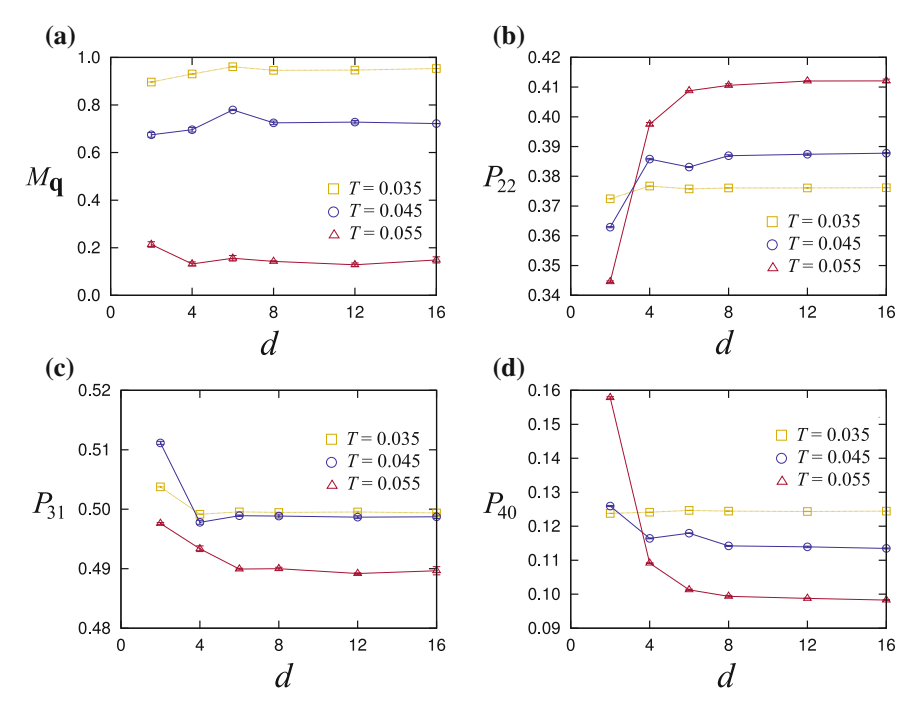


**Fig. 9.8** PEMC results for d dependence of **a**  $M_{\bf q}$ , **b**  $P_{22}$ , **c**  $P_{31}$ , and **d**  $P_{40}$ . The calculations are done for  $N=4\times 8^3$  and  $\mu=-3.4$  with  $m_{\rm tot}=40$ 

the Fermi level is close to the band bottom. In the small electron density region, the precise structure of DOS near the band edge plays a crucial role for the thermodynamics; to reproduce the details of DOS requires larger number of polynomials. Another possible source is the small energy scale in the low density region. Because of the small kinetic energy, the effective interactions between localized spins become small, and hence, the relevant T range including  $T_c$  is much lower than that in the higher density region. This also requires larger number of polynomials for sufficient convergence.

Next, we discuss the convergence with respect to the real-space truncation. The results in Figs. 9.7 and 9.8 show that sufficient convergence is obtained for  $d \gtrsim 8$  for both  $N = 4 \times 6^3$  and  $4 \times 8^3$ . This is consistent with the expectation that the necessary truncation distance is not strongly dependent on the system size. Unfortunately, as d = 8 covers the large part of the system with  $N = 4 \times 6^3$  and  $4 \times 8^3$ , the truncation method is not helpful to reducing the calculation amount for the present system sizes.

# 9.7 Summary

In this section, we have presented the benchmark results on the application of polynomial expansion Monte Carlo method to a geometrically-frustrated spin-charge coupled system, a spin-ice type Kondo lattice model on a pyrochlore lattice. We have investigated the convergence of Monte Carlo results with respect to the number of polynomials  $m_{\text{tot}}$  and the truncation Manhattan distance d. The results indicate that, in the electron density region  $0.15 \le n \le 0.35$ , the polynomial expansion Monte Carlo results with  $m_{\text{tot}} = 40$  show sufficient convergence to those obtained by the conventional Monte Carlo method using the exact diagonalization. The results show that, although the current model has a  $\delta$ -function singularity in the density of states in the noninteracting limit associated with the geometrical frustration, the polynomial expansion Monte Carlo results show good convergence within the number of polynomials comparable to previous studies for unfrustrated models. For the realspace truncation, our results indicate that  $d \gtrsim 8$  gives well converged results for  $N = 4 \times 6^3$  and  $4 \times 8^3$ , while  $d \gtrsim 6$  is enough for  $N = 4 \times 4^3$ . This condition, however, is insufficient for reducing the calculation amount. Hence, we did not use the truncation method in the calculation presented in Chap. 7.

#### References

- G. Alvarez, C. Sen, N. Furukawa, Y. Motome, E. Dagotto, Comput. Phys. Commun. 168, 32 (2005)
- 2. N. Furukawa, Y. Motome, H. Nakata, Comput. Phys. Commun. 142, 410 (2001)
- 3. Y. Motome, N. Furukawa, J. Phys. Soc. Jpn. 68, 3853 (1999)
- 4. C. Sen, G. Alvarez, N. Furukawa, I.A. Sergienko, T.C. Schulthess, A. Moreo, E. Dagotto, Phys. Rev. B 73, 224430 (2006)
- 5. G.P. Zhang, Commun. Comput. Phys. 10, 422 (2011)
- 6. G.P. Zhang, J. Zhang, Q.-L. Zhang, J.-T. Zhou, M.H. Shangguan, Preprint arXiv:1206.6944

# Chapter 10 **Summary**

**Abstract** In this section, we summarize the main results of this thesis, theoretical studies of the Ising spin Kondo lattice models on frustrated lattices: triangular, kagome, and pyrochlore lattices. Using a Monte Carlo simulation, we explored emergence of various nontrivial magnetic states that arise from geometrical frustration and thermal fluctuation. Transport properties in the thermally induced novel states are also discussed.

In this thesis, we studied the thermodynamic behavior of Ising-spin Kondo lattice models on geometrically frustrated lattices: triangular, kagome, and pyrochlore lattices. Throughout the thesis, we extensively discussed the magnetism and electronic/transport properties of the models. The focus of this study is two-fold: (a) to explore novel magnetic phases induced by the spin-charge coupling and thermal fluctuations, and (b) to study how such phases affect the electronic and transport properties of the coupled itinerant electrons.

Physics of spin-charge coupled systems has been one of the major topics in condensed matter physics. Under strong influence of the effective magnetic interactions mediated by the kinetic motion of itinerant electrons, the localized moments in the spin-charge coupled systems show rich behavior. At the same time, the magnetic state of the localized moments is reflected to the itinerant electrons, giving rise to novel transport phenomena. In relation to various systems such as Mn oxides, rare-earth compounds, and spin glass alloys, these phenomena have been studied extensively both in experiment and theory.

On the other hand, recent experiments on the pyrochlore and triangular metallic oxides gave rise to a new question; how does the geometrical frustration affects the magnetic and electronic properties of the spin-charge coupled systems. In localized spin models, it is known that the frustration in interactions gives rise to various exotic behavior far different from the well known magnets. In the spin-charge coupled systems, however, the studies in this direction are still limited and even the magnetic phase diagram of the single-band classical-spin Kondo lattice models remain to be studied. To clarify the fundamental features of the Kondo lattice models on frustrated lattices, and to provide a solid ground for discussing the magnetic and electronic properties of the materials with frustrated lattice structure, we theoretically studied one of the simplest models on frustrated lattices with spin-charge coupling.

128 10 Summary

In Chap. 3, we studied the magnetic phase diagram of an Ising-spin Kondo lattice model on a triangular lattice. By using a Monte Carlo simulation, we showed that a three-sublattice partially disordered state is realized at finite temperature in the phase competing region between stripe, three sublattice ferrimagnetic, and Kosterlitz-Thouless type phases. We also conducted a mean-field type analysis, and discussed the possibility of the partially disordered state to be stabilized by the charge gap formation. This is the first example of the two-dimensional partial disorder, which was shown to be unstable in the previous studies on the two-dimensional Ising models.

In Chap. 4, we discussed the electronic structure of the three-sublattice ferrimagnetic state discovered in Chap. 3. We conducted the band structure analysis and derived the low-energy effective Hamiltonian. The results showed that the band structure is strongly spin dependent, and at electron density n = 2/3, the electronic bands for electrons with the spin anti-parallel to the net magnetic moment (we call this the "down" spin) forms an energy gap. On the other hand, the electronic bands for electrons with the spin parallel to the net magnetic moment form a semi-metallic structure with Dirac nodes at the Fermi level. Hence, in the vicinity of n = 2/3, a half-metallic state with fully spin-polarized Dirac electrons is realized in this model.

In addition, by a variational calculation and a Monte Carlo simulation, we showed that the ferrimagnetic order is stabilized in a wide range of the spin-charge coupling. We also presented that introducing a weak nearest-neighbor Kondo coupling significantly stabilizes the ferrimagnetic state in the vicinity of electron density n = 2/3.

In Chaps. 5 and 6, we considered Kondo lattice models on kagome lattices. In Chap. 5, we investigated the thermodynamic behavior of the collinear Ising-spin Kondo lattice model on a kagome lattice. We investigated the phase diagram in a wide range of electron density by a Monte Carlo simulation at finite temperature and by a variational calculation at zero temperature. In the ground state, we found the ferromagnetic, q=0 ferrimagnetic state, and  $\sqrt{3}\times\sqrt{3}$  ferrimagnetic states by a variational calculation. On the other hand, at finite temperature, we found three thermally-induced states: the loop liquid, Kosterlitz-Thouless, and partially disordered states. Here, the Kosterlitz-Thouless and partially-disordered states are the magnetic states similar to that found in the triangular lattice case.

On the other hand, the loop-liquid state is a peculiar ferrimagnetic state which possesses a fractional magnetic moment but no magnetic superstructure. In this state, all the triangles are in the two-up one-down spin configurations, which results in the emergent degree of freedom, i.e., the loops connecting the up-spin sites and isolated down spins. However, as the two-up one-down local correlation is insufficient to drive the system to form a long-range order, the system remains in a disordered state with 1/3 magnetic moment of the fully saturated case. We also investigated the transport properties of the itinerant electrons in the loop-liquid state, and showed that the formation of the loops manifests in resonant peaks in the optical conductivity.

In Chap. 6, we studied the electronic and transport properties of a kagome-lattice model with noncoplanar Ising spins. Namely, we considered a kagome-ice type Ising-spin Kondo lattice model. We conducted an extensive study on the effect of ice-rule type local correlations on the itinerant electrons, and found that an energy gap develops in the electronic density of states for itinerant electrons. Associated

10 Summary 129

with the energy gap formation, we found that the Hall conductivity is quantized to  $\sigma_{xy} = e^2/h$ . These results indicate that the kagome-ice local correlation gives rise to a quantum anomalous Hall state without a magnetic long-range order, Landau levels, and the relativistic spin-orbit coupling. In addition, we conducted Monte Carlo simulation on the thermodynamic properties, and found that the kagome-ice quantum anomalous Hall insulator is realized in the presence of external magnetic field.

Finally, in Chaps. 7, 8 and 9, we considered a Kondo lattice model on a pyrochlore lattice with spin-ice type localized moments. In Chap. 7, we considered the weak coupling region for the spin-ice Kondo lattice model. The phase diagram of the spin-ice Kondo lattice model with varying the electron density was calculated by using the polynomial expansion Monte Carlo method. We found that a 32-sublattice magnetic order emerges in between the ice-type magnetic orders and all-in/all-out antiferromagnetic order. We presented that the magnetic order is driven by the third-neighbor interactions, and nearest-neighbor interaction is irrelevant in this region. In addition, we showed that the 32-sublattice order accompanies charge disproportionation. We also demonstrated that the charge disproportionation can be switched along with the magnetic order by the external magnetic field.

Chapter 8 is devoted to the strong coupling limit for the spin-ice Kondo lattice model discussed in Chap. 7. By controlling the antiferromagnetic super-exchange interaction between the localized moments, we found that a peculiar intermediate phase appears in the phase competing region between the ice-rule type ferromagnetic and all-in/all-out antiferromagnetic states. In addition, by the analysis on an effective spin model, we found that the intermediate state is driven by the second- and third-neighbor interactions. In the intermediate state, the spatial inversion symmetry of the pyrochlore lattice is broken by the formation of all-in/all-out spin clusters. On the other hand, the time-reversal symmetry is preserved as the clusters are thermally fluctuating between the all-in and all-out states. We also showed that the formation of spin clusters has a substantial effect on transport properties. In particular, we showed that the intermediate state may exhibit a nonzero spin Hall conductivity even in the absence of the spin-orbit coupling.

In Chap. 9, we presented the benchmarks of the polynomial expansion method used in the Monte Carlo simulation in Chaps. 7 and 8. By comparison of the polynomial expansion method to the Monte Carlo simulation using exact diagonalization, we show that a sufficient convergence is achieved within reasonable numbers of polynomials. Application of this method to the pyrochlore model enabled us to conduct simulations on large size systems in three dimensions, as presented in Chaps. 7 and 8.

To summarize, in this thesis, we studied the magnetic and electronic properties of Ising-spin Kondo lattice models on several different frustrated lattices. Throughout the study, we mainly used an unbiased Monte Carlo simulation to obtain reliable, numerically-exact results within the statistical error bars. Our results indicate that the spin-charge coupling and geometrical frustration give rise to peculiar magnetic states; the Slater type mechanism and further-neighbor effective interactions have important contribution to these phenomena. In addition, the spin correlations of peculiar states in the Kondo lattice models are reflected to the itinerant electrons,

130 10 Summary

resulting in interesting transport phenomena. These results imply that the spin-charge coupling brings about qualitatively different nature in the magnetism and transport phenomena from those in the unfrustrated systems.

# **Curriculum Vitae**

#### Hiroaki Ishizuka

Kavli Institute for Theoretical Physics Kohn Hall, University of California Santa Barbara, CA 93106-4030, USA

e-mail: ishizuka@kitp.ucsb.edu

# Appointments

April 2014–present Postdoctoral researcher, University of California,

Santa Barbara

April 2011–March 2014 JSPS research fellow (DC1), The University of Tokyo

#### Education

2013 Ph.D. in Applied Physics, The University of Tokyo
2011 M.E. in Applied Physics, The University of Tokyo
2009 B.E. in Applied Physics, Tohoku University

# Refereed Papers

1. H. Ishizuka, Y. Motome, Exotic magnetic states in an Ising-spin Kondo lattice model on a Kagome lattice. Phys. Rev. B **91**, 085110 (2015)

132 Curriculum Vitae

2. H. Ishizuka, L. Balents, Magnetism in S = 1/2 double perovskites with strong spin-orbit interactions. Phys. Rev. B **90**, 184422 (2014)

- 3. H. Ishizuka, M. Udagawa, Y. Motome, Polynomial expansion Monte Carlo study of frustrated itinerant electron systems: application to a spin-ice type Kondo lattice model on a pyrochlore lattice. Comput. Phys. Commun. **184**, 2684 (2013)
- 4. H. Ishizuka, Y. Motome, Spontaneous spacial inversion symmetry breaking and spin Hall effect in a spin-ice double-exchange model on a pyrochlore lattice. Phys. Rev. B. **88**, 100402(R) (2013)
- 5. H. Ishizuka, Y. Motome, Loop liquid in an Ising-spin Kondo lattice model on a Kagome lattice. Phys. Rev. B **88**, 081105(R) (2013)
- 6. H. Ishizuka, Y. Motome, Thermally-induced phases in an Ising Kondo lattice model on a triangular lattice: partial disorder and Kosterlitz-Thouless state. Phys. Rev. B **87**, 155156 (2013)
- 7. H. Ishizuka, Y. Motome, Quantum anomalous Hall effect in kagome ice. Phys. Rev. B **87**, 081105(R) (2013)
- 8. H. Ishizuka, Y. Motome, Dirac half-metal in a triangular ferrimagnet. Phys. Rev. Lett. **109**, 237207 (2012)
- 9. H. Ishizuka, M. Udagawa, Y. Motome, Magnetic order and charge disproportionation in a spin-ice type Kondo lattice model: large scale Monte Carlo study. J. Phys. Soc. Jpn. **81**, 113706 (2012)
- 10. H. Ishizuka, Y. Motome, Partial disorder in an Ising-spin Kondo lattice model on a triangular lattice. Phys. Rev. Lett. **108**, 257205 (2012)
- 11. M. Udagawa, H. Ishizuka, Y. Motome, Non-Kondo mechanism for resistivity minimum in spin ice conduction systems. Phys. Rev. Lett. **108**, 066406 (2012)
- 12. H. Ishizuka, Y. Motome, N. Furukawa, S. Suzuki, Quantum Monte Carlo study of molecular polarization and antiferroelectric ordering in squaric acid crystals. Phys. Rev. B **84**, 064120 (2011)
- 13. H. Ishizuka, M. Udagawa, Y. Motome, Metal-insulator transition caused by coupling to localized charge-frustrated systems under ice-rule local constraint. Phys. Rev. B **83**, 125101 (2011)
- 14. M. Udagawa, H. Ishizuka, Y. Motome, Quantum melting of charge ice and non-Fermi-liquid behavior: an exact solution for the extended Falicov-Kimball model in the ice-rule limit. Phys. Rev. Lett. **104**, 226405 (2010)

# **Proceedings**

- M. Udagawa, H. Ishizuka, Y. Motome, Invariant energy levels and flat band engineering in Kondo lattice model on geometrically frustrated lattices. JPS Conf. Proc. 3, 014009 (2014)
- 2. H. Ishizuka, Y. Motome, On the stability of quantum Hall Kagome-ice insulator. JPS Conf. Proc. **3**, 014010 (2014)
- 3. H. Ishizuka, M. Udagawa, Y. Motome, Monte Carlo study of an effective Ising model for the spin-ice type Kondo lattice model. JPS Conf. Proc. 3, 014013 (2014)

Curriculum Vitae 133

4. H. Ishizuka, Y. Motome, Thermally-induced magnetic phases in an Ising spin Kondo lattice model on a kagome lattice at 1/3-filling. J. Korean Phys. Soc. **63**, 579 (2013)

- H. Ishizuka, M. Udagawa, Y. Motome, Application of polynomial-expansion Monte Carlo method to a spin-ice Kondo lattice model. J. Phys. Conf. Ser. 400, 032027 (2012)
- 6. H. Ishizuka, Y. Motome, N. Furukawa, S. Suzuki, Quantum Monte Carlo study of the transverse field Ising model on a frustrated checkerboard lattice. J. Phys. Conf. Ser. **320**, 012054 (2011)